Ultra-Wideband CMOS Transceiver Front-End for Bio-Medical Radar Sensing

A Thesis Submitted to the

College of Graduate Studies and Research

in Partial Fulfillment of the Requirements

for the degree of Doctor of Philosophy

in the Department of Electrical and Computer Engineering

University of Saskatchewan

Saskatoon

By

Xubo Wang

Permission to Use

In presenting this thesis in partial fulfilment of the requirements for a Postgraduate degree from the University of Saskatchewan, I agree that the Libraries of this University may make it freely available for inspection. I further agree that permission for copying of this thesis in any manner, in whole or in part, for scholarly purposes may be granted by the professor or professors who supervised my thesis work or, in their absence, by the Head of the Department or the Dean of the College in which my thesis work was done. It is understood that any copying or publication or use of this thesis or parts thereof for financial gain shall not be allowed without my written permission. It is also understood that due recognition shall be given to me and to the University of Saskatchewan in any scholarly use which may be made of any material in my thesis.

Requests for permission to copy or to make other use of material in this thesis in whole or part should be addressed to:

Head of the Department of Electrical and Computer Engineering
Engineering Building
57 Campus Drive
University of Saskatchewan
Saskatoon, Saskatchewan
Canada
S7N 5A9

Abstract

Since the Federal Communication Commission released the unlicensed 3.1-10.6 GHz frequency band for commercial use in early 2002, the ultra wideband (UWB) has developed from an emerging technology into a mainstream research area. The UWB technology, which utilizes wide spectrum, opens a new era of possibility for practical applications in radar sensing, one of which is the human vital sign monitoring.

The aim of this thesis is to study and research the possibility of a new generation human-respiration monitoring sensor using UWB radar technology and to develop a new prototype of UWB radar sensor for system-on-chip solutions in CMOS technology. In this thesis, a low-power Gaussian impulse UWB mono-static radar transceiver architecture is presented. The UWB Gaussian pulse transmitter and receiver are implemented and fabricated using 90nm ST CMOS technology. Since the energy of low order Gaussian pulse is mostly condensed at lower frequency, in order to transmit the pulse in a very efficient way, higher order Gaussian derivative pulses are desired as the baseband signal. This motivates the advancement of the design into UWB high-order pulse transmitter. Both the Gaussian impulse UWB transmitter and Gaussian higher-order impulse UWB transmitter take the low-power and high-speed advantage of digital circuit to generate different waveforms. The measurement results are analyzed and discussed.

This thesis also presents a low-power UWB mono-static radar transceiver architecture exploiting the full benefit of UWB bandwidth in radar sensing applications. The transceiver includes a full UWB band transmitter, an UWB receiver front-end, and an on-chip diplexer. The non-coherent UWB transmitter generates pulse modulated baseband signals at different carrier frequencies within the designated 3-10 GHz band using a digitally controlled pulse generator. The test shows the proposed radar transceiver can detect the human respiration pattern within 50 cm distance.

The applications of this UWB radar sensing solution in commercialized standard CMOS technology include constant breathing pattern monitoring for gated radiation therapy, real-time monitoring of patients, and any other breathing monitoring. The research paves the way to wireless technology integration with health care and bio-sensor network.

Acknowledgements

There are many people I would like to thank for their support, encouragement, and criticism. First and foremost, I would like to thank my supervisors, Professor Anh Dinh, and Professor Daniel Teng, for their support, encouragement, and dedication throughout the years I spent in the VLSI lab. They helped me to establish a direction of research and provided valuable guidance, evaluation, and advice throughout the thesis work.

I would like to thank all the members of the VLSI group for valuable discussions and feedbacks. In particular Professor Li Chen for his Sun micro-system work station with Linux design environment. Thank Professor Robert Johanson for being in my advisory committee, reading my thesis, and giving me a lot of valuable suggestions and feedbacks. Thank Professor Chris Zhang for being in my advisory committee, taking time to read my thesis, and providing valuable feedbacks. Especially, I would like to thank Professor Sebastian Magierowski for taking time to read and review my thesis, and providing a lot of extremely valuable, thoughtful, and insightful feedbacks for the thesis improvement.

I would like to thank Dr. Liangjun Lei and Dr. Qiming Ren at China Unichip Tech., and Director Benvidi Moe at LSI Corporation for the extremely valuable learning experience, tape-out experience, and testing experience they offered during my internship. They provided me the opportunity to know how to approach a better and working design, and to jump start my career in IC industry as a designer as well. All those valuable technical discussions and technical supports they provided have broadened my vision and deepened my knowledge and understanding. Working with them makes my tape-out experience much less painful.

I also would like to thank CMC Microsystems in Canada for the design tools and the chip fabrication services. This project was partially supported by the Natural Sciences and Engineering Research Council of Canada under Strategic Project Grant number STPGP 350545.

I want to deeply thank my parents, Zengzhang Wang and Jianrong Cui for all of their tremendous support and love, without which I could not make this thesis possible. They gave me courage to move on at the moments when I felt desperate, depressed, and hopeless. No matter how hard the life is, I should never give up on my dreams because miracles happen everyday.

To my beloved family

Don't forget that there are places in the world that are not made up of stone, there is something inside that they can not get to, that is hope.

The Shawshank Redemption

Contents

List of Tables

List of Figures

List of Abbreviations

ADC	Analog-to-Digital Converter
AOA	Angle Of Arrival
BPSK	Binary Phase Shift Keying
CMOS	Complementary Metal Oxide Semiconductor
DCO	Digitally Controlled Oscillator
ESD	Electrostatic Discharge
FCC	Federal Communication Commission
FDTD	Finite-Difference Time-Domain
FFT	Fast Fourier Transform
FSPL	Free Space Path Loss
HRV	Heart Rate Variability
IBM	International Business Machines corporation
IEEE	Institute of Electrical and Electronic Engineer
IR	Impulse Radio
KCL	Kirchhoff's Current Law
LNA	Low Noise Amplifier
LO	Local Oscillator
MB-OFDM	Multi-band Orthogonal Frequency Division Multiplexing
MOS	Metal Oxide Semiconductor
NF	Noise Figure
NMOS	N-type Metal Oxide Semiconductor
OOK	On Off Keying
PCB	Printed Circuit Board
PHY	Physical layer
PLL	Phase-Lock-Loop
PMOS	P-type Metal Oxide Semiconductor
PRI	Pulse Repetition Interval
PRF	Pulse Repetition Frequency
RCS	Radar Cross Section
RFIC	Radio Frequency Integrated Circuit
RSS	Received Signal Strength
SI	Signal Integrity
SMA	Sub-Miniature version A
SNR	Signal to Noise Ratio
SoC	System on Chip
ST	ST microelectronics
STI	Shallow Trench Isolation
TDOA	Time Difference of Arrival
TSMC	Taiwan Semiconductor Manufacturing Company
TOA	Time Of Arrival
UWB	Ultra Wideband
VGA	Variable Gain Amplifier
WPAN	Wireless Personal Area Network

Part I

Preface

No path leads from a knowledge of
that which is to that which should be.

Albert Einstein

Chapter 1

Introduction

This chapter provides a brief summary of the status and recent trends in ultra wideband (UWB) technology and UWB radar sensing. There is an increasing demand for mobile health monitoring solutions from an aging society. The release of the UWB frequency band by the Federal Communication Commission (FCC) makes it possible to build a next-generation low-power and low-cost mobile health-monitoring radar sensor for life-sign monitoring. The development of an economical system-on-chip (SoC) solution in UWB band is the focus of this dissertation. Section 1.1 presents an overview of the UWB technology and current UWB research on biomedical radar sensing. Section 1.2 presents the motivation and the objectives of this research. Section 1.3 summarises the research contributions, and Section 1.4 describes the road-map of the dissertation.

1.1 Recent Trends in UWB Technology and UWB Radar Sensing

Since the FCC released the 3.1 to 10.6 GHz frequency band for commercial use in 2002 [1, 2, 3], the UWB has evolved from an emerging technology into a mainstream research topic. The UWB technique differs from current wideband technologies, such as direct sequence orthogonal frequency-division multiplexing (DS-OFDM) and the frequency hopping spread spectrum (FHSS), by using extremely short pulses as signals and signal transmission without carriers. The direct baseband transmission characteristic is the fundamental difference between the UWB technique and the technologies mentioned above.

Over a hundred years ago, the first UWB radio appeared in the form of a spark gap radio that could transmit simple Morse code across the Atlantic ocean [4]. However, due to the

uncontrollable signal frequency spectrum at that time, the spark gap radio was soon replaced by the conventional narrow-band radio technology. A quiet century followed, before recent technology innovation in mobile communication and commercially available complementary metal oxide semiconductor (CMOS) technologies were developed, and the greater demand for bandwidth brought the UWB radio to life.

Over the last decade, UWB technology has shown great potential capability for very high-throughput, short-range applications such as high-speed data transmission, indoor video distribution, low-rate, low-power sensor networks, positioning applications, and radar sensing applications [4, 10]. The fundamental characteristic that differentiates UWB from conventional wireless communications is the absence of carrier signals. The UWB employs extremely narrow Gaussian monocycle pulses and any other shapes of short radio frequency (RF) pulses to represent information. The extremely short pulses in turn generate a very wide band spectrum and offer several advantages: high channel capacity, covertness, ability to work with low signal-to-noise ratios (SNR), low transmit power requirements, better resistance to multipath interference, simple transceiver architecture, and ability of coexistence with recent radio spectrum [4, 5]. In addition, UWB not only can transmit a large amount of data over a short distance with very low power, but also has the ability to pass through objects that are more likely to reflect narrow bandwith signals [9]. These advantages make UWB an alternative solution to the narrow-band technology for sensing applications

In recent years, UWB has drawn significant attention especially for applications in target positioning because of the extremely wide bandwidth and strong potential for high-precision radar applications. An emerging area is biomedical radar sensing and biomedical imaging that takes advantage of the very short wavelength and high resolution of the UWB signal [10].

The use of radar in monitoring human physiologic functions began in the 1970s [6], but development was hindered until the commercially affordable low-power CMOS technology matured in the late 1900s. An UWB radar biomedical application was first proposed in 1998, and a few years later, several U.S. patents describing its medical applications were claimed [6, 7, 8]. One of the most cited researchers was Thomas McEwan at the U.S. Lawrence Livermore National Laboratory [7, 8], who described promising medical applications and emphasized that the *"device is medically harmless, as the average emission level used (about 1 μW) is about three orders of magnitude lower than most international standards for continuous*

human exposure to microwaves" [7, 8].

A recent demand for a biomedical device that can monitor patients vital life indexes such as heart rate variability (HRV) and respiration rate requires a small, wearable, and wireless networkable device that can enable pro-active home monitoring of vital signs [6]. In any aging countries, such a device could reduce the cost of health-care by moving eligible patients from hospital to home-care to release the medical resources. This device could also provide early diagnostics for pathological patients. The networkability enables the device to transmit and share the monitored data with other systems, for example, those in the hospital monitoring center. This requires a communication link from the wearable sensor to a base station. This device should have a bio-radar sensor part and a wireless link all implemented in one device [6]. UWB technology can fulfill these requirements. The physical characteristics of the UWB short pulse make it possible to achieve both high data rate transmission and accurate radar sensing. The wide frequency of the UWB signal allows it to have the better ability to penetrate biological materials such as skin, fat, and other organic tissues, and reflection of the signal from internal organs provides a means to monitor vital signs [9, 10, 11]. The available UWB bandwidth is also attractive to such radar sensing device solutions because of its low complexity, low power consumption, robustness to system specifications, and the most importantly, it is unlicensed.

The UWB system allows imaging of internal organ movements without invasive surgical contact or direct contact through skin [6, 9]. The UWB transceiver is simple and occupies a very small chip area because it does not require a complex frequency recovery system as does the narrow bandwidth transceiver. The power consumption of an UWB system is extremely low because the system only consumes power during the pulse transmitting and receiving period [4, 6]. This is another advantage of UWB for battery-driven device.

Examples of UWB radar systems for biomedical sensing applications can be found in [12, 13, 14, 15] and the PAM 3000, the first UWB commercial product for respiration rate detection, made by Wireless2000 as described in [16]. The system described in [12, 13] uses discrete electronic components on a printed circuit board (PCB); large physical dimensions and high power-consumption make this device awkward for wearability and networkability. The PAM 3000 is designed to be placed underneath the patients mattress for stationary monitoring using high cost, large power-consuming discrete blocks; it is thus not compact

and is not designed as a wearable sensor. The UWB radar sensor proposed in this project is suitable for noninvasive detection of human respiration and other biomedical imaging solution; other attributes are very low product cost, low power consumption for battery-powered devices, high miniaturization capability (it can be worn by a moving person), and environmental friendliness due to its very low electromagnetic energy emission.

Most radars use narrow band frequency signals to detect targets. The frequency bandwidth of conventional radars usually is no more than 10% of its carrier frequency. This signal reflection only provides very simple information about the target coordinates. The information content of the target relies on the frequency band of the signal [17]. In general, radar is similar to the eyes of a person, and the UWB radar with the wide-band signal is similar to an eye with an excellent sight [17]. It not only can tell the location of the targets, but also the characteristics of the targets. Therefore, this frequency diversity is extremely useful in biomedical sensing.

1.2 Motivation and Research Objectives

A general UWB bio-radar system consists of three parts: software layer, baseband signal processing layer, and physical layer (PHY). Software layer provides the interface between bio-radar and users. Baseband signal processing quantizes, filters, and analyzes the received radar signals. This can be done either using hardware or software. Physical layer, which is the last but the most important part of the system, generates and transmits UWB pulses, and receives and detects the target reflections. The performance of the physical layer is the bottleneck that determines the overall success of the entire bio-radar system. This thesis work focuses on the physical layer, which is the transceiver front-end of the UWB bio-radar system.

Many published works have discussed the UWB CMOS transmitter/receiver design for short-range communications, but very few demonstrated the UWB transceiver design in standard CMOS process for biomedical radar sensing for human vital sign monitoring [18, 19, 20, 21, 22, 23, 24]. It is generally agreed that using UWB technology in an integrated CMOS process for biomedical sensing can provides low power, ultra-low cost, and ultra-low area solutions with more acceptable and reliable performance, thanks to the cost advantage, SoC

capability, and continuously improving performance of modern standard CMOS process [10]. However, to the author's best knowledge, no published work has demonstrated the design and implementation of the biomedical radar sensing on a single CMOS integrated UWB transceiver front-end that utilizes the full UWB frequency band to provide frequency diversity. In addition, considering the growing demand for a low-cost mobile health monitoring device, it is desirable to investigate in UWB transceiver SoC.

The basic goals of this research is to study the possibility of UWB CMOS radar sensing using UWB signals (either impulse UWB signals or short carrier-based UWB signals, a formal definition of the UWB signal will be discussed in Chapter 2). More particularly, this research project focuses on the development of a fully radio-frequency integrated circuits (RFIC) front-end using CMOS technology and UWB technology for compact and portable radar sensing devices with low power consumption. Three objectives are initialized:

- To explore different UWB transmitter approaches using digital and analog circuits;
- To propose an integrated radar SoC solution which can achieve the radar sensing for human vital signs monitoring;
- To explore and implement the integrated single chip radar transceiver circuit in CMOS IC.

This project will implement the first low-power, low cost CMOS biomedical radar using UWB signals for human vital sign monitoring with better accuracy and controllability, compared with conventional heart measurement devices built with discrete components. This project will contribute in the development of next generation real-time medical monitoring methods for both home-care and hospital treatment. This project will also make it possible to build and verify an UWB pulse propagation channel model for human heart and human chest tissues in future.

This project can also be carried out further to apply in biomedical imaging using UWB radar. By characterizing the propagation models of different tissues inside a human body, an image inside the human body can be generated under an UWB radar scanning. This scanning, for instance, can be used for 3-Dimensional printing of internal tissues and organs using bio-ink made of biodegradable gel and actual human cells. The UWB radar sensing technology may lead a technology breakthrough in the biomedical sensing and imaging areas.

1.3 Thesis Contributions

This thesis covers different approaches to UWB radar transceiver solution implementation for UWB radar sensing, including digitally generated Gaussian impulse approach and carrier-based UWB approach. The broad themes of this thesis is to explore a most appropriate and feasible solution in terms of power consumption, area, and bandwidth usage, and to explore the possibility of bio-radar sensing using UWB technology. The task can be broken up into the following contributions.

- UWB radar transmitter/receiver using Gaussian impulse and energy collection scheme. This approach proposes an all-digital UWB impulse transmitter generating Gaussian pulses whose spectrum are from 3 to 5 GHz (after a pulse shaping filter), with extremely low pulse energy and low area. The large available bandwidth relaxes the specifications on frequency precision to reduce system complexity. An energy-collection type receiver has been proposed, fabricated, and simulated as well. The transmitter has been demonstrated in a fabricated test chip in ST 90 nm CMOS.

- An all-digital bi-phase higher-order Gaussian pulse UWB transmitter for next generation bio-radar sensing system characterized by a high data rate, low area, low power consumption, and low complexity, and designed to fit UWB band, is proposed for real-time bio-medical sensing. The transmitter is using an all digitally controlled circuit pulse generator to generate the tenth-order derivative of Gaussian pulse with Bi-phase modulation scheme operating in the 6 - 10GHz band. This proposed work is analyzed using TSMC 90 nm CMOS technology. By using the proposed technique, the transmitter can not only generate tenth-order Gaussian pulse, but any poly-cycle pulses through pulse combinations by controlling the delay elements in each edge generator and the number of edge generators used based on different bandwidth and center frequency.

- Proposes an carrier-based mono-static UWB radar transceiver to detect respiration rate. This fully integrated UWB radar transceiver is implemented using the standard 130 nm CMOS process. This UWB radar transceiver integrates an UWB diplexer with a full UWB band carrier-based transmitter and receiver front-end. This radar transceiver uses the entire UWB band to exploit its full benefit of UWB technology in

various applications. The experiment demonstrates that a human breathing rate up to 50 cm away can be successfully detected.

This research on UWB bio-radar transceiver serves as a useful starting point for future researchers to carry out further study in this area. So far, we have very limited knowledge of the accurate human body propagation model at UWB frequency. There is no UWB loss model for human tissues exists which are necessary to open a new research area in 3D human imaging. The UWB radar transceiver solutions will enable the investigation of UWB signal propagation model of the human body. In addition to applications to the biomedical field, the UWB bio-radar sensor can be also applied to other civil applications requiring contactless detection of moving objects.

This dissertation may also be useful in guiding the design of future generation implantable UWB bio-radar transceivers for biomedical radar sensing and imaging applications and contribute to the enhancement of the wellbeing of mankind.

1.4 Thesis Organization

This thesis focuses on the topic of ultra wideband radar transceiver with a particular emphasis on transceiver design and implementation. The remainder of this thesis is organized as follows.

Chapter 2 provides a general overview of the UWB signal fundamentals and UWB radar transceiver techniques in CMOS technology. Choices of UWB radar detection methodologies and different UWB radar transceiver architectures are introduced. The design fundamentals needed in high frequency CMOS design are briefly discussed as well. This chapter also briefly talks about the biomedical radar sensing network and proposes a reliability model of the radar sensing network based on the Markov process described in Appendix A.

Chapter 3 describes and discusses the design of a Gaussian impulse UWB transmitter and Gaussian higher-order impulse UWB transmitter using digital circuit approach. The Gaussian impulse UWB transmitter was designed and fabricated using 90 nm ST CMOS technology. Measurements of the transmitter are presented in this chapter.

Chapter 4 describes and discusses the design approach of a carrier-based UWB radar transmitter. This proposed carrier-based UWB radar transmitter achieves a full UWB band

frequency tuning range. The transmitter was fabricated using 130 nm IBM CMOS technology. The circuit implementation and measurement results are also discussed in this chapter.

Chapter 5 describes and discusses the design approach of a fully-integrated UWB receiver front-end. The designed bandwidth of this UWB radar receiver front-end is 3-10 GHz. The receiver front-end was implemented and fabricated using 130 nm IBM CMOS technology. The measurement results are discussed as well.

Chapter 6 demonstrates the radar experimental results, summarizes the performance of the fabricated UWB radar transceiver, and compares the performance to the similar UWB radar transceiver reported recently.

Finally, Chapter 7 summarizes the thesis and research contributions, and extends the possible research in the future.

Part II

Overview

Chapter 2
Ultra-Wideband Radar Transceiver in CMOS Technology

2.1 UWB Introduction

Ultra-wideband is a generic term describing the radio technology which uses low energy level and a large portion of spectrum for short-range communications. The formal definition of ultra wideband (UWB) is the radio technology with a 10 dB bandwidth exceeding 500 MHz or 20 % of the arithmetic center frequency of the signal, according to the FCC [1].

In conventional communication systems, a transmitter employs a specific carrier frequency to carry information. The signal carrier is a continuous wave (usually a sinusoidal wave) with well-defined energy spectrum in a narrow band, which is very easy to detect. In the UWB case, the transmitter uses very short pulses with a very low duty cycle to represent the information bits. The pulse itself contains the information and is sent directly to the receiver for detection and translation. The very low duty cycle results in a very low average transmission power, and since the spectrum of a signal is inversely related to its pulse width, the short pulses spread their energy across a wide range of frequencies, which in turn results in a very low power spectral density. Figure 2.1 illustrates the differences between conventional communication system and UWB system in a more interpretative way.

2.1.1 Regulations of UWB Technology

In order to protect the conventional communication systems from interference, FCC assigned an unlicensed frequency spectrum mask for UWB applications in the 3.1GHz to 10.6GHz frequency band. There are four masks for indoor UWB applications, outdoor UWB applications,

through-wall UWB imaging applications, and vehicular radar systems respectively [1, 2, 3]. Since this project falls in the category of indoor UWB applications, the first type of emission is considered in the design. Figure 2.2 shows the FCCs emission mask for indoor UWB applications.

For indoor applications, the average output power spectrum density is limited by FCC to -41.3 dBm/MHz between 3.1GHz and 10.6GHz and limited to -53dBm/MHz between 1.99GHz and 3.1GHz, as illustrated in Figure 2.2 [1]. The maximum emissions regulated by FCC are the same as the RF emissions allowed from a home electronic appliance such as a digital alarm clock: *"at or below 75 billionths of a watt"* [25]. This limitation coexists with the FCC Part 15 general emission limits to controlled radio interference [1, 2, 3]. In March 2005, the FCC granted a waiver that allows the use of gated UWB to achieve a high instant power emission. This means UWB systems with a very low duty cycle can transmit at much higher power levels and idle the rest of the time, as long as they still meet the same limits for average power density during the overall period of UWB system operation [26]. The waiver applies only to indoor and hand-held UWB devices. In January 2012, the FCC issues another waiver to FCC Part 15.503(d) that originally requires the UWB system to have a fractional bandwidth equal to or greater than 0.20 or has an UWB bandwidth equal to or greater than 500 MHz at any point in time [26]. This waiver allows UWB radar to perform multiband frequency sweeping for higher image resolution as long as the total operating frequency band exceeds 500 MHz. These two latest FCC waivers open a door for the UWB bio-radar technology to evolve to achieve better detection range, higher accuracy, and higher image resolution.

In this thesis, the targeted UWB signal has a frequency spectrum in 3.1 GHz to 10.6 GHz band. The targeted average transmitting power spectrum density level in this 7.5 GHz frequency band is limited to -41.3 dBm/MHz. It is worthwhile to mention that although the FCC regulated the UWB spectrum, the industrial standardization still remains un-finalized. The FCC masks are the guidelines for forming the regulation templates in other countries including Canada.

One of the big challenges when designing an UWB transmitter is to generate an output UWB pulse that fits the FCC spectral mask. As for bio-radar sensing, low power consumption constraint is another important factor for the transmitter. However, since there is no such a

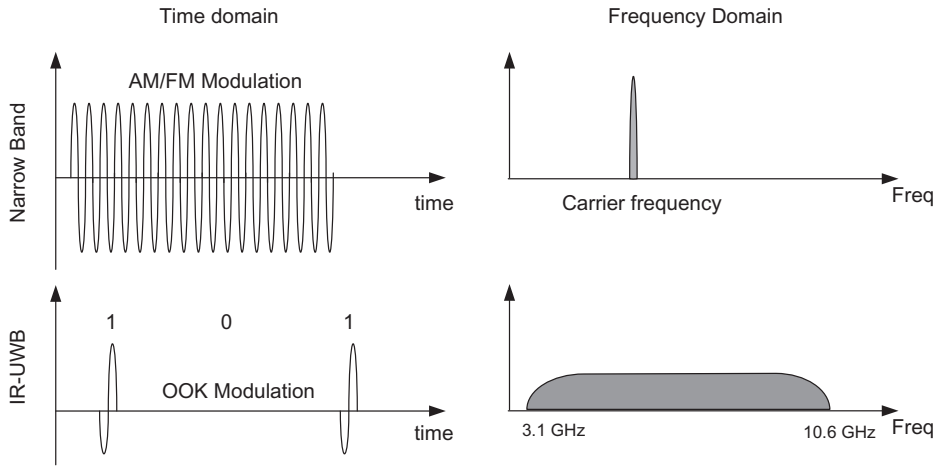

Figure 2.1: Narrowband and UWB signals in the time domain and the frequency domain, reproduced from [5]

regulation describing the shape of the UWB waveform, the transmitted pulse shape choice is left to the designers as long as the pulses meet the FCC spectral limit. The selection of the UWB signal is important as the shape of the signal will affect the signal spectrum. In addition, the emergence of the sub-micron CMOS technology, allowing the fast generation of nanosecond level pulse, makes the UWB signals more welcome.

2.1.2 IEEE Standardization

There are two working groups in the Institute of Electrical and Electronic Engineer (IEEE) associated with this emerging technology:

1. IEEE 802.15.3a group was formed to provide an UWB PHY for applications involving high-speed data transmission. The members of the task group were not able to come to an agreement on the choice of technology proposals between Multi-band Orthogonal Frequency Division Multiplexing (MB-OFDM) and direct sequence UWB, which were supported by two different industry alliances (WiMedia Alliance and UWB Forum). This group was dismissed in January 2006 [27].

2. IEEE 802.15.4a group was formed in August 2007 to try to come up with a PHY providing higher precision ranging and location capability, higher aggregate throughput, longer range, lower power consumption, and lower cost. The selected possible PHY technologies are: UWB Pulse Radio (unlicensed UWB band) and a Chirp Spread Spec-

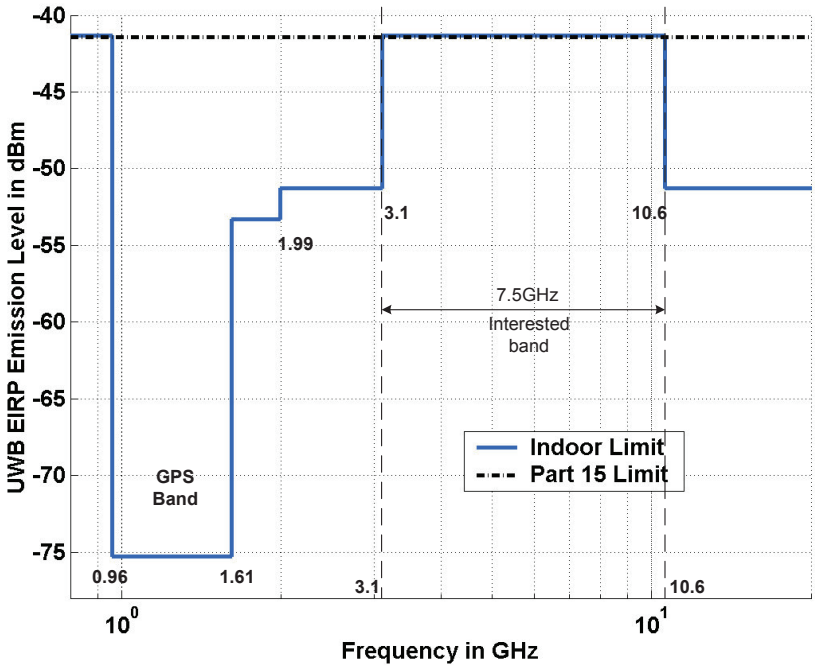

Figure 2.2: FCC indoor UWB spectrum mask, reproduced from [1]

trum (unlicensed 2.4 GHz band) [28, 29]. One of the goals of this group is to focus and develop PHY with low data rate wireless personal area network (WPAN), radar, and sensor networks [28, 29].

2.2 UWB Signals

The terminology Ultra-Wideband is an expression that describes the type of signals that fall in this bandwidth in a very general way. There are two most widely accepted types of UWB signals categorized based on modulation [31]:

1. Impulse Radio UWB (IR-UWB): this UWB signal category is generally used to describe transceiver systems using short impulses with frequency inside 3-10 GHz range. This system, also called carrier-less system, uses pulses as signal carrier to carry messages. IR-UWB signal is often time-modulated before transmission. As seen in [30, 31], the major challenges of impulsed UWB signal is that it is difficult to control the exact impulse shape and its center frequency. On the other hand, the IR-UWB system provides a great potential for ultra low power transceiver design because of the digitally generated low power character.

2. Carrier-based UWB (CB-UWB): this UWB signal category is similar to the conventional radio systems. The carrier signal is a narrow band signal, and this narrow-band signal is modulated by different pulse shapes. This type of UWB system uses frequency conversion and has better spectral control. The major difference between this CB-UWB and the conventional system is that the modulated signal is transmitted as baseband signal with an extremely low duty cycle. The frequency accuracy and controllability, compared to IR-UWB signals, makes the CB-UWB signal meet the FCC spectrum mask better and easier.

2.2.1 UWB Impulse Signal

UWB Impulse signal can be defined as a sudden change of voltage or current signal in an extremely short time. Impulse used here is a generic terminology used for the pulse signal whose energy falls within the wideband spectrum. A few terms that may show ambiguity are well defined and summarized in the following definitions in [31].

- Impulse/pulse: a sudden change of electrical field in time domain whose spectrum is in a UWB band after filtering. It is generally recognized an UWB pulse.
- Burst: *"an emitted signal whose time duration is not related to its bandwidth"* [31].

The IR-UWB is a wideband radio technique that is not based on the modulation or the transmission of a continuous wave. This technique use very low duty-cycle pulses representing one bit or symbol, and it can include all three aforementioned signal definitions: impulse, pulse or burst [31], as long as the signal spectrum is ultra wideband.

2.2.2 Carrier-based UWB Signal

Many approaches are proposed in recent publications to generate the carrier-based UWB pulses. Many uses switched voltage controlled oscillator (VCO) to generate short pulses, as shown in Figure 2.3. Figure 2.3 (a) shows a rectangular-shaped short pulse and Figure 2.3 (b) shows a Gaussian-shaped short pulse in time domain. A rectangular pulse in frequency domain has a sinc function shape, and a Gaussian pulse in frequency domain still has a Gaussian shape. These two types of pulses are all generated by mixing either a rectangular

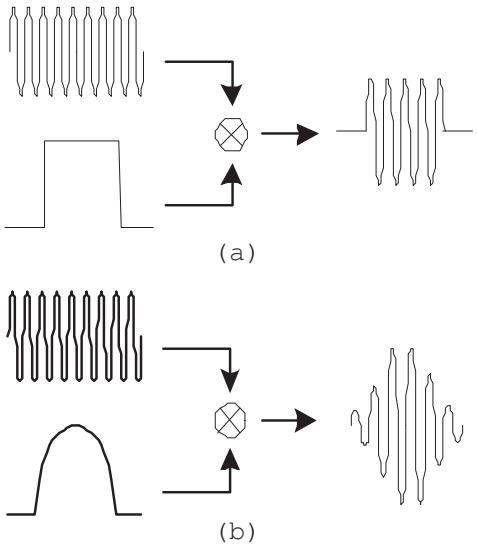

Figure 2.3: Different carrier-based pulse generator schemes.

or a Gaussian pulse with a sinusoidal carrier generated by a VCO. The frequency spectrum of the rectangular and Gaussian waveforms at lower frequencies are shifted upwards. The expressions of these two types of UWB pulses are:

$$v_1 = \frac{1}{2}V_{DD}[1 + \cos(\omega_0 t)] \cdot [u(t) - u(t - t_0)] \tag{2.1}$$

$$v_2 = \frac{1}{2} \cdot \frac{\sqrt{2}}{\alpha} e^{-\frac{2\pi t^2}{\alpha^2}} [1 + \cos(\omega_0 t)] \tag{2.2}$$

where ω_0 is the carrier frequency, u(t) is the unit step function, and t_0 is the pulse width. This pulse generation method can accurately control the pulse in the frequency domain. With a very careful design and gating scheme, this method can consume only a very small amount of power, even with power-hungry VCO and mixer blocks.

2.3 UWB Radar Overview

2.3.1 Detection Scheme

This section discusses different radar detection methodologies: angle of arrival (AOA), received signal strength (RSS), time of arrival (TOA), and time difference of arrival (TDOA)

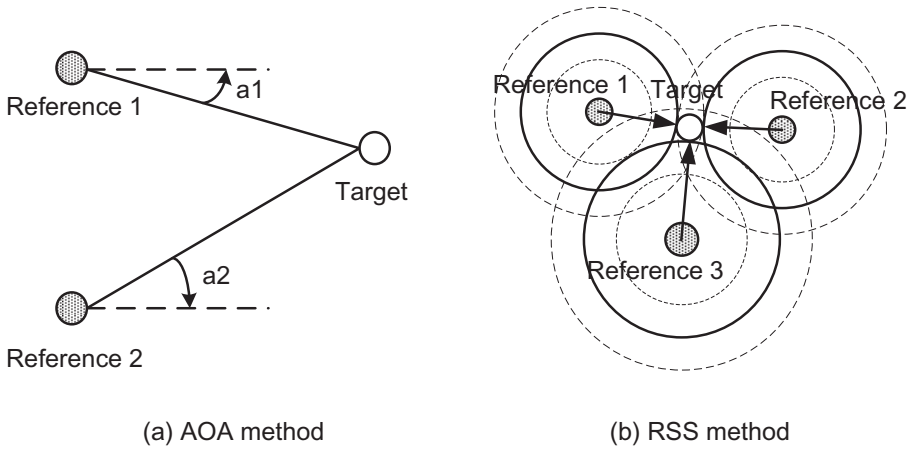

Figure 2.4: Radar detection methodology: (a) AOA method; (b) RSS method [10]

methods.

The AOA method identifies the location of a target in 2-dimension (2D) space by measuring the angles between the reference points and the target $\angle a1$ and $\angle a2$ (seen in Figure 2.4 (a)). This method requires a linear antenna array or a circular antenna array to detect a reflection signal [33]. Usually these types of antenna arrays take a lot of space. AOA method is not the best solution for UWB radar because UWB signal has wide bandwidth, so the diffraction and reflection caused by surrounding objects will have higher probability to result in dispersion in time domain. This effect becomes more obvious in the indoor environment, making angle calculation very difficult. The space and complexity cost of the antenna array make the AOA method even more disadvantageous.

The RSS method calculates the location of a target by measuring and calculating the return signal strength to three different reference points, based on the pre-built channel attenuation model (seen in Figure 2.4 (b)). This method relies heavily on the precision of the channel attenuation parameters, antenna characteristic, channel model, and frequency. In UWB band, the received signal power can be represented by the summation of the received signal power from each multi-path. For conceptual example, at receiver a, the received return signal power from b can be represented as [33]

$$P_r^a = P_{reflect}^b - P_L^{ab}(d_{ab}) - P_L^{ab}(f) \tag{2.3}$$

where $P_L^{ab}(d_{ab})$ is a channel loss function of the distance d_{ab}, and $P_L^{ab}(f)$ is a channel loss function of the frequency f. $P_{reflect}^{b}$ is the returned signal power at point b.

Equation (2.3) [33] shows that this method requires a large number of models for different frequencies and different surrounding environments to obtain an accurate target distance. This method also requires at least three receivers, which may enormously increase the complexity and power of the UWB radar system. However, this RSS method can be applied to a UWB radar sensor network, where a large number of sensors are deployed.

The TOA method locates the distance from radar to a target by measuring the time of the arrival of the reflected signal. Because UWB signal has very short pulse width (nanoseconds) and very high resolution, it is the most suitable for target detection using the TOA technique. In addition, TOA requires much less complexity compared to other methods.

The target detection performance based on a TOA method is sensitive to pulse spectrum and bandwidth. The tendency is that the higher center frequency will generate better resolution [32, 32]. The pulse repetition interval time (PRI) dominates the inter-symbol interference. A high PRI is desirable for accurate resolution and detection because a high PRI will reduce the possibility of pulse collisions and multipath interferences. This also relaxes the design requirement of the transceiver circuits.

2.3.2 UWB Radar Concept

Radar sensing methodology is the foundation of information perception in this world. The simplest example is the human visual and acoustic perception of surroundings based on the scattering of electromagnetic waves (light) from nearby objects such as buildings, plants, automobiles, and even other human faces. Humans can detect detailed geometrical structures and images of the objects because the wavelength of the light is extremely small relative to physical sizes of the most objects in nature [10]. However, light only occupies a small part of the spectrum and has poor penetrating capability. In order to make use of the scattering of electromagnetic waves at other frequencies, different artificial radar are created based on current technology for different applications. This includes UWB radar.

UWB radars are utilizing the electromagnetic waves that occupy a very large band from 3 to 10 GHz. Generally speaking, electromagnetic waves in this frequency can penetrate

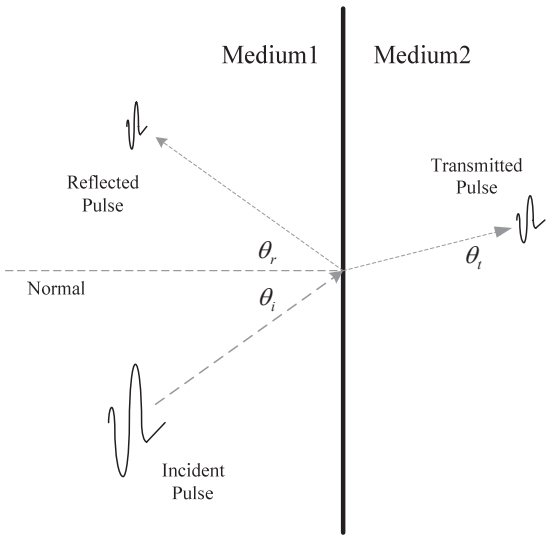

Figure 2.5: UWB pulse reflection and transmission illustration

most non-metallic materials (including human tissues) so that objects remaining under cover may be detected [11, 10]. Because of the large bandwidth, they can detect object with a decimetre, centimetre or even millimetre resolution due to the fact that more information on the object can be provided by a larger bandwidth [10]. Besides this, polar molecules, for example water and human tissues, experiences relaxation effects under particular frequencies. The characteristics of this type of material make the target characterization and identification possible [11].

This fine resolution and high penetrating capability makes the UWB radar beneficial for medical applications [10]. For these reasons, the UWB pulse (usually in order of few hundreds picoseconds to few nanoseconds) with a large bandwidth (nominally 3-10 GHz) makes it possible to build radar with much better spatial resolution compared to other conventional radars [32]. Also, the wide spectrum allows the signal processing unit of the UWB radar to gather detailed information about the surrounding objects and detect, identify, and locate only the most desired target among other objects [6]. The UWB signal with a wide frequency content can pass through a large number of biological materials (most are polar molecules) such as human tissues, fat, blood, and bone [6, 8, 11].

To work as an UWB radar, the UWB transmitter sends an UWB signal toward a target and an UWB receiver detects the reflected signal. This is the basic algorithm applied in the UWB radar sensing. For the biomedical sensor in this project, the target is a human chest.

To further explore how the chest movement can be detected and measured, it is useful to take a close look at what is measured and analyzed in the sensing process.

When the electromagnetic wave with an incident angle θ_i in propagation reaches a boundary of medium with different dielectric properties, a portion of the incident electromagnetic wave is reflected back into the starting medium with a reflection angle θ_r (zero reflection angle if the incident wave path is at the right angle to the boundary surface), while the rest portion of the wave continues propagating through the next medium [9, 32]. The transmission of UWB pulse has the same principal, as shown in Figure 2.5.

The reflection coefficient for the incident wave at a right angle is Γ and the transmission coefficient at a right angle is γ. The reflected and transmitted signals are expressed as

$$E_t \cos\theta_t = \gamma \cdot E_i \cos\theta_i \tag{2.4}$$

$$E_r \cos\theta_r = \Gamma \cdot E_i \cos\theta_i \tag{2.5}$$

where E_i is the incident wave, E_r is the reflected wave, and E_t is the transmitted wave respectively. The reflection coefficient at a right angle can be represented by

$$\Gamma = \frac{\frac{Z_1}{Z_2} - 1}{\frac{Z_1}{Z_2} + 1} \tag{2.6}$$

where $Z_1 = \sqrt{\varepsilon_0/\varepsilon_1}$ and $Z_2 = \sqrt{\varepsilon_0/\varepsilon_2}$ are the characteristic impedances of medium one and medium two, respectively. ε_1 and ε_2 are the relative permittivities of the two mediums. ε_0 is the permittivity of free space. Studies and researches show that there is a noticeable difference in dielectric properties between each layers of human internal tissues [11, 15, 32]. Therefore, when a pulse reaches the interface between the two tissues, partial reflection occurs. The most reflection occurs on the boundary of air and skin.

The primary components of an UWB sensor radar consist of a transmitter and a receiver. These two parts can be either implemented in the same chip or in separate chips. The transmitter sends out a pulse to the thorax and sends a timing signal to a processor. As the

pulse propagates through skin (including epidermis, dermis, and subcutaneous layer), fat, pectorals muscle, cardiac muscle, and heart blood, several reflections occur at each interface. At this moment, it is believed that the energy reflection from the interface between cardiac muscle and heart blood is the highest among these reflections. This is because the dielectric properties between cardiac muscle, which belongs to soft tissue category, and heart blood differ noticeably while the differences of dielectric properties between other similar soft tissues are minor since they are formed by similar types of carbohydrate macromolecules. For the above reason, the receiver only detects the reflected pulse and sends another timing signal to the processor. The time interval t between two timing signals is the pulse round trip time. The distance d is then computed using Equation 2.7,

$$d = t \times v \tag{2.7}$$

where v is the wave travelling velocity. The velocity is material dependent and different propagation velocities are estimated based on tissues relative permittivity. The movements of either the heart muscle or the skin are analyzed based on the computed distance. After repeating sending pulses and receiving pulses, a pattern for measured distances can be plotted and heart beating rate or respiration rate can be obtained.

The radar sensing range can be estimated based on the model of the signal path loss, receiver sensitivity, antenna gain, and maximum transmitting power. The power budget of the signal path is expressed as

$$\mathrm{P}_{received}|_{dBm} = P_{transmitted}|_{dBm} + G_{antenna} - P_{loss}|_{dB} \tag{2.8}$$

Based on the budget link equation, the radar detection range could be derived as

$$Range = \sqrt[4]{\frac{P_{transmitted} \cdot G^2 \cdot \lambda^2 \cdot \sigma}{P_{received} \cdot (4\pi)^3 \cdot L}} \tag{2.9}$$

where L is the loss factor, which consists of the internal attenuation of the radar on the transmitting and receiving paths (this can be measured), $L_{internal-path}$, the free space attenuation $L_{channel}$, and attenuation during propagation inside human body L_{body}. L_{body} accounts for other loss and attenuation in the human body, and these values could be obtained experi-

mentally.

Target Scattering

In UWB radar sensing, the echo signals reflected from targets are obtained directly in time domain for analysis. The received echo wave in time domain is normally the addition of reflected signals from different human body tissue layers. Different return signal time delays can uncover more details about the target shape and different return signal durations are possibly related to the physical dimension of the targets [17, 11]. Most importantly, since the electromagnetic wave propagation inside human tissues greatly depends on the wave frequency, different tissue layers reflect signals at different frequencies.

When radar sensing the human body, one important parameter commonly used to describe the target is the scattering cross section σ as shown in Equation 2.10 [10]

$$\sigma = 4\pi R^2 \frac{E_r^2}{E_{in}^2} \tag{2.10}$$

where R is the distance from the radar antenna to the desired body area, E_r is the reflected signal electric field intensity at the target, and E_{in} is the transmitted signal electric field intensity at the transmitter. This generally simplified target scattering equation reveals the target's capability of reflecting signals. The scattering theory in [10] suggests that the material with an unique dielectric in a target scatters an incident wave independently of others [32, 33]. Thus, in UWB bio-radar design, the transmitter sends radar signals consisting of many Gaussian pulses instead of one pulse to get more target signatures. Therefore, as mentioned in [10], the overall target scattering σ is the sum of each independent scattering σ from different parts in the target. As a result, the received signal reflection is the superposition of each reflected waveforms in time domain [11]. This can be expressed with target scattering parameter of n individual reflections as [10, 34]

$$\sigma_{total} = \sum_{k=1}^{n} \sigma_k \tag{2.11}$$

For bio-medical radar sensing, the frequency diversity is very desirable because different frequency components can provide detailed information about complex targets inside a human

body [17, 10]. More particularly, to improve the detection capability of the UWB radar, the bio-radar employs a transmitting signal on more than one frequency. This is because by sweeping the frequency, the statistical probability of the target visibility will be increased [35]. A better detection results will be achieved if the separation of the center frequency of the transmitting signal are larger.

2.4 UWB Radar Transceiver Architectures

When designing an UWB radar transceiver system, there are two design issues that need to be taken into account: transceiver architecture and circuit implementation. A appropriate transceiver architecture determines the overall system capabilities, and good design and engineering approaches enhance radar system performances [36]. The detection range of UWB radar depends on output signal power level, transmitter and receiver structure design, target scatter area, and baseband signal processing.

2.4.1 Transmitter

In a traditional narrow band transceiver, up-conversion and down-conversion are needed at transmitter and receiver to convert baseband signals to and from high frequency signals. Mixers and phase-lock-loops (PLL) are required to generate local oscillator (LO) frequency. The need of PLLs and up/down mixers greatly increase the overall system complexity and performance criteria of each blocks. In comparison, the UWB transceiver (especially the transmitter) uses the time modulated RF pulses as signals, eliminating the need of complex carrier frequency conversion process.

The UWB transmitter normally consists of only a pulse generator, a modulator, and an output driver. Since the UWB signal is more often analyzed in time domain, the most popular modulation schemes adopted are on-off keying (OOK) and binary phase-shift keying (BPSK) for the sake of transceiver simplicity. Pulse position modulation (PPM) is another modulation scheme for the UWB system. However, the PPM scheme requires time synchronization between transmitter and receiver. This synchronization requires complicated timing circuits, increasing the complexity of the transceiver.

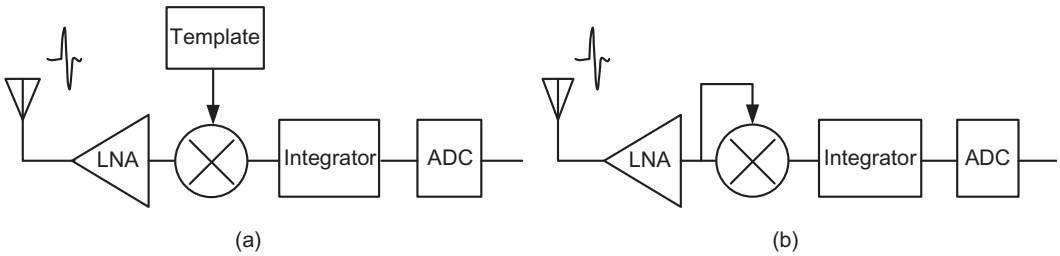

Figure 2.6: (a) Coherent receiver, and (b) non-coherent receiver (b)

2.4.2 Receiver

Coherent, non-coherent, and direct-conversion sampling receivers are three major types of receivers that could be applied for UWB wireless link [24, 36, 19, 20]. The best receiver structure choice mainly depends on the kinds of signal the receiver expects and the applications.

Both coherent and non-coherent structures use cross-correlation to detect the signal. The cross-correlation of two signals is defined based on the autocorrelation using two signals instead of one signal [24, 19, 20, 36, 38, 39]. It provides a measure of the dependencies between two signals. The received signal correlation allows for the stimulation and characterization of a target with arbitrary signals. This increases the flexibility of available radar sensing measurement [10]. The coherent structure, as illustrated in Figure 2.6 (a), is applied when the receiver knows what kind of signals to expect and knows the phase of the expected signals. This requires a timing synchronization mechanism between transmitter and receiver because the data signal may appear to be noise if the signal is out of phase [24, 19, 36]. In a coherent receiver, the received signal correlates with a local template signal through multiplication. The correlated signal is then integrated, followed by a decision making threshold detector.

Compared to coherent detection, the major difference of a non-coherent receiver, as illustrated in Figure 2.6 (b), is that the non-coherent receiver signal correlates with the received signal itself, rather than a local template [24, 19, 20, 36, 38, 39]. This self-multiplication correlation eliminates the need for complex timing synchronization between transmitter and receiver, which makes it a better choice for radar sensing because most of the time the target channel model is unknown and the time of pulse arrival is unpredictable. This non-coherent detection is also referred to as an energy detection receiver. The energy detection based UWB receiver can easily detect and recover the energy/symbol in the multipath channel and multi-target environment [36].

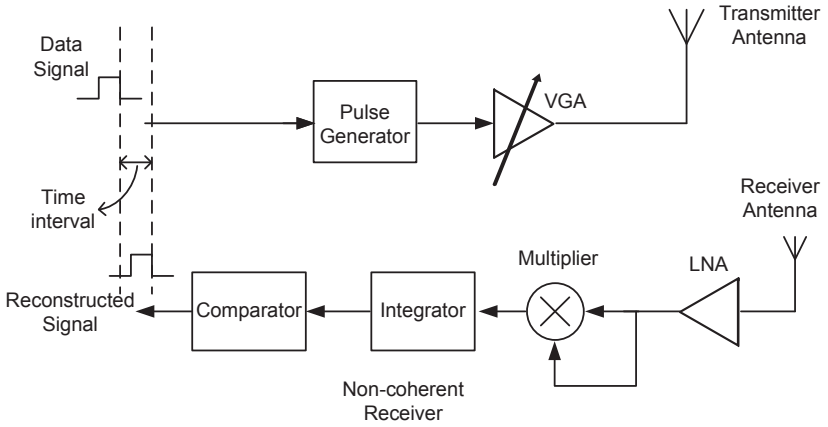

Figure 2.7: Energy Detection UWB transceiver architecture

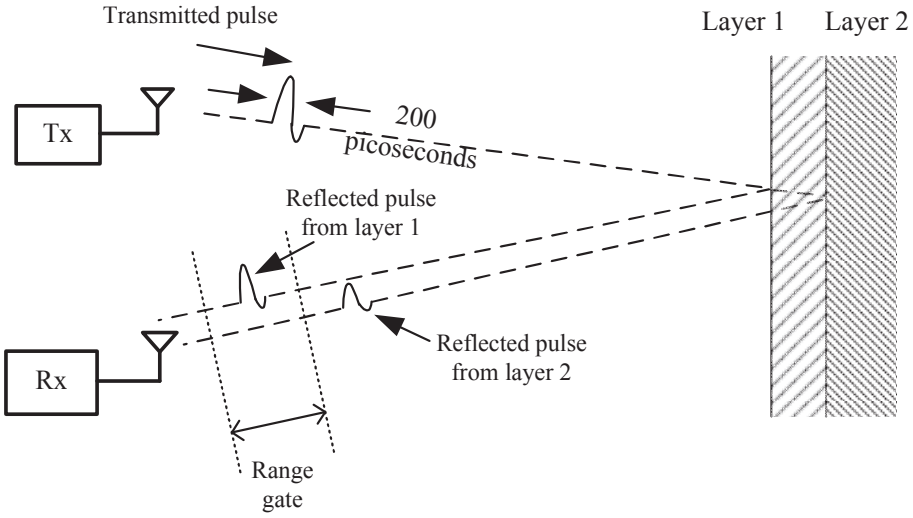

Figure 2.8: UWB radar detection scheme using TOA method

The sampling receiver does not involve energy detection. Instead, it employs a high sampling rate analog-to-digital converter (ADC) to quantize the signal after a RF front-end LNA [19, 40]. For an UWB signal at 3-10 Ghz frequency band, a multigigahertz ADC, which is a power-hungry block, is required to sufficiently quantize the signal for baseband processing and target extraction. At the time of this thesis is written, there is no reported work on the integration of the multigigahertz ADC into UWB receiver front-end.

Although the CMOS has many drawbacks in terms of RF performance and noise, this technology is mature, low-cost, low-power, and highly integrable. Figure 2.7 shows a typical architecture of the UWB energy detection CMOS transceiver for radar sensing and short-range sensor communications [10].

In this architecture, the transmitter sends a pulse train towards the target. The interface between two media produces a partial reflection. Then the receiver detects and samples this particular type of reflected pulse train and the decision circuit makes the final decision [10]. Pulses are diffracted and scattered by different tissue layers and organs in a human body. Channel distortion and power loss easily destructs the reflected pulses and make them undistinguishable. The range-gate is designed to look for the expected reflecting pulse rather than wait and receive every reflected pulse from every location and try to identify the expected return pulse. The receiver samples only the pulses arriving at the receiver during a very narrow time window after pulse transmission, as shown in Figure 2.8. By estimating the distance of the expected target, a delay time is chosen to control the range-gating signal.

Compared to the conventional radar systems, this transceiver architecture greatly reduces the circuitry complexity and power consumption. The transmitter consists of a modulator, a pulse generator, and a variable gain amplifier (VGA) driver. An on-off keying (OOK) modulation scheme is used to modulate the pulse. The VGA and driver are used to amplify output and match output impedance. The receiver consists of a low noise amplifier (LNA), a correlator, an integrator, a clocked voltage comparator, and a delay controller. The input clock train and control signal are modulated to a sequence of clock pulses, which then enters the pulse generator to produce a pulse train. This pulse train is passed onto a driver amplifier and then to an UWB antenna. The reflected pulse is caught by the antenna in the non-coherent receiver and amplified by a LNA. The signal is then squared by a multiplier at the asynchronous receiver. The squared output is in turn fed into an integrator and clocked comparator to boost up the voltage and reconstruct the signals. The range controller uses logic gates to switch on/off the LNA and disable the sampling operation of the comparator for range finding.

2.5 UWB Radar Sensor Network Overview

This section briefly talks about the potential sensor architecture and applications that can be constructed using the proposed UWB radar sensing transceiver in this research work. Understanding how the sensor network is structured will yield useful design insights for design improvement [41]. This section also expands the discussion of a reliable UWB radar

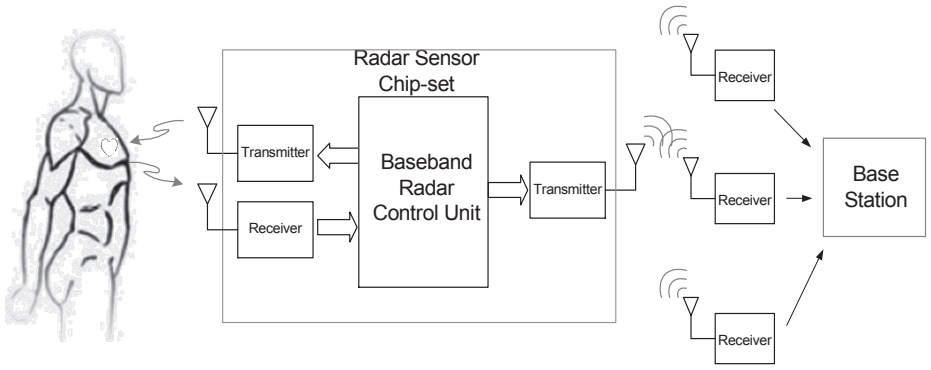

Figure 2.9: UWB biomedical sensor overview

sensor network based on the combination of RSS and TOA method. This section has been published in [41].

2.5.1 Radar Sensor Network Structure

As discussed in the early section, the UWB biomedical radar sensing system works by transmitting electromagnetic energy towards a human body and receiving the reflected signal from tissues and organs inside the body. A biomedical sensor network can be built based on the single sensor employing UWB technology described above and illustrated in Figure 2.9.

The wireless sensor network communication and distribution structure are application and technology dependent [42]. The sensor network proposed in this chapter is used for monitoring of a patient's health conditions. This UWB bio-sensor network can be employed to monitor a chronic condition in real-time, to record a patient's recovery from a surgical operation, or to detect early medical conditions [42, 43]. The performance of the the UWB bio-sensor network depends on how reliably the network can sense and delivery the sensed data from a radar sensor to a sink node. Due to the requirements for real-time monitoring of patient's vital signs, the sensor network must achieve certain reliability and the system must be resistant to individual component failure [42, 43]. In addition, it is difficult to access the sensors for repair or replacement [42]. Therefore, the sensor network should be in normal operation when a part of the whole sensor network breaks down. An example application of the UWB bio-sensor network is shown in Figure 2.10.

A wireless bio-sensor network consists of a large set of spatially distributed and disposable

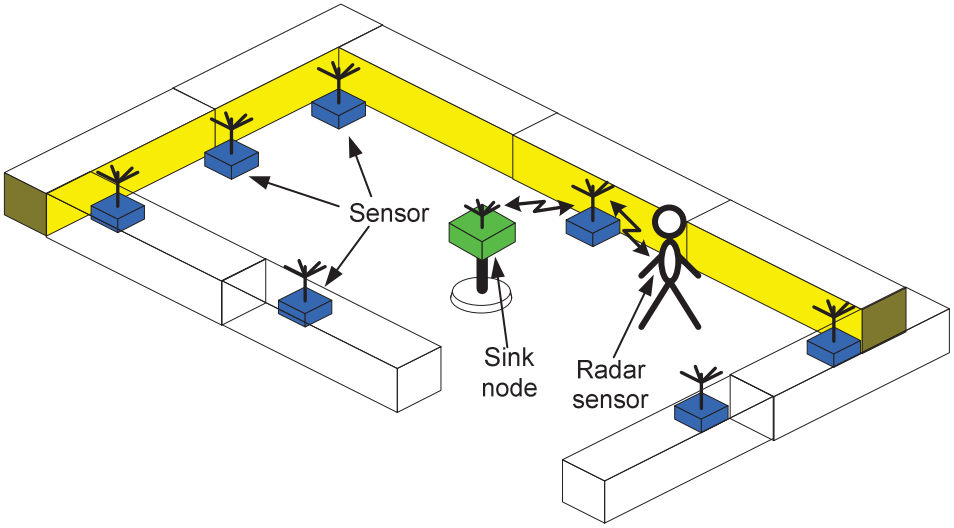

Figure 2.10: An illustration of a biosensor network

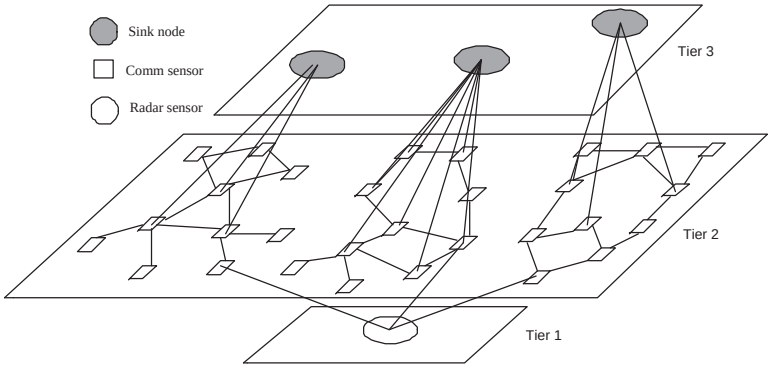

Figure 2.11: Biomedical radar and sensor network architecture.

UWB radar sensors that are able to communicate with each other using short pulses. The optimal use of the energy is a primary concern for this UWB sensor network [44, 45, 46].

The architecture of the proposed sensor network is shown in Figure 2.11. The bio-sensor network is proposed for continuous long-life instantaneous human body health monitoring using a fault-tolerant three-tiered structure. There are three types of sensors: wearable UWB radar sensor (tier 1) that monitors the human body health index, UWB communication sensors (tier 2) that behave as a link between the radar sensor and the sink node, and the sink node (tier 3) that gathers the information sent by the sensor under its monitor and sent information to the base station or other sink nodes.

The UWB bio-sensors communicate with the sink node using UWB signals. The pulsing sensor eliminates the need for complex up-conversion and down-conversion of the baseband

signals, which in turn largely reduce the sensor power consumption. The second tier sensors (communication sensors) consists of N number of identical stationary sensors: all of them can receive and transmit information from and to a sink node and adjacent sensors through multihop communication [42, 43, 44, 45, 46, 47]. To minimize power consumption, each sensor has n transmitting power levels [42]. The sensor is in idle state when it is not being used. When being active, the sensor starts with the lowest power level. If at this level the sensor is not able to establish a communication with any other sensors or sink node, the sensor increase the power to the next level. If it fails to establish a communication, the sensor increases the power further to the maximum power allowable.

In tier one, the wearable bio-radar sensor measures the physiological index of the patient and sends the signals to the closest available sensor node. As the subject moves out of the previous sensor range, the radar sensor establishes a new communication with the next sensor in the sensor network. Along the way of the patient's movement, each available sensor detects the radar sensor signal and reports to the sink node. The patient's position can be tracked as well by using this technique.

A reliability model using a continuous Markov process is developed for the proposed wireless UWB bio-sensor network. The detailed model is presented by the author in [41]. The study show that sensor network reliability is related to sensor output power. The overall system reliability can be increased at the cost of increasing sensor power.

2.6 RF Circuit Design Considerations

UWB transceiver design involves digital circuit blocks and RF analog circuit blocks. The RF analog circuit design requires additional techniques and principles built upon tremendous design experience and knowledge. This section overviews a few most important RFIC design issues that are frequently met throughout the design of UWB radar transceiver.

2.6.1 Impedance Matching and RLC networks

The fundamental design philosophy difference between RF design and digital circuit design is the impedance matching at input and output. This impedance matching becomes particularly important at high frequency, where the wavelength of the signal is compatible with the

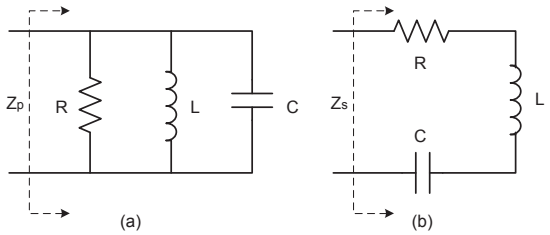

Figure 2.12: RLC networks: (a) parallel connection, (b) series connection

physical size of the signal runners.

The reason for impedance matching in RF design is the objective of maximum power transfer between different circuits, while the objective of the digital circuit is to transfer signal status rather than actual power. In a transceiver system, the transmitter output signal is modulated by a digital signal, and this digital signal is only required to reach an effective threshold to make the modulation function properly. On the receiver side, however, the modulated RF signal is propagated through a link with a lot of attenuation, and the most effective way to transfer and receive the signal before demodulation is power transfer rather than status transfer. To achieve the maximum power transfer between blocks, the source impedance and load impedance must be matched. The impedance matching is often realized by RLC networks.

The RLC network, often referred as LC resonator, is made up of an inductor and a capacitor connected either in series or in parallel form. Figure 2.12 shows both the parallel RLC network and series RLC network. The resistor R usually represents the parasitic resistance introduced by inductor L and capacitor C. Equation 2.13 is the equivalent impedance of the RLC in series, and Equation 2.12 is the equivalent impedance of the RLC in parallel.

$$Z_P(s) = \frac{1}{1/R + sC + 1/sL} \tag{2.12}$$

$$Z_S(s) = R + sL + \frac{1}{sC} \tag{2.13}$$

The resonance frequency for both networks can be expressed by the same ω_0

$$\omega_0 = \frac{1}{\sqrt{LC}} \tag{2.14}$$

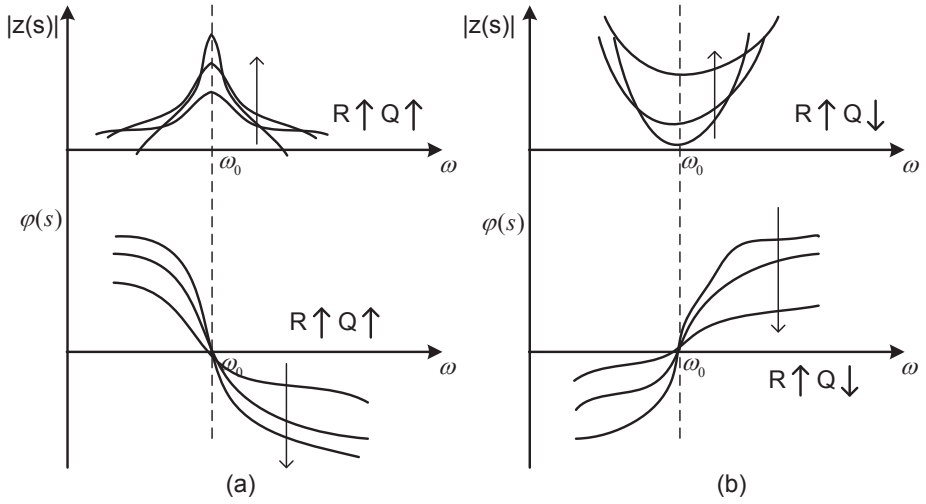

Figure 2.13: RLC network impedance and phase response: (a) parallel connection, (b) series connection

The quality factor Q of the RLC network is defined as the ratio between the energy stored in the circuit and the energy dissipated in the circuit each period. Q is also described as the ratio of resonance frequency and 3 dB bandwidth of the circuit. The equivalent quality factor of the parallel RLC Q_P is given by

$$Q_P = \frac{R}{\omega_0 L} = \omega_0 CR \tag{2.15}$$

The equivalent quality factor of the series RLC Q_S is given by

$$Q_S = \frac{\omega_0 L}{R} = \frac{1}{\omega_0 CR} \tag{2.16}$$

For a parallel RLC network, the magnitude of impedance reaches its peak value R at the resonance frequency ω_0. Its phase response appears to be capacitive when $\omega < \omega_0$ and inductive when $\omega > \omega_0$. For a series RLC network, the magnitude of impedance reaches its minimum value R at the resonance frequency ω_0. Its phase response appears to be capacitive when $\omega > \omega_0$ and inductive when $\omega < \omega_0$. This is illustrated in Figure 2.13. Q_P is increased as R increases in the parallel RLC circuit, and Q_S is decreased as R increases in the series RLC circuit. Q is proportional to the frequency selectivity of the circuit, therefore, high Q is desirable in RFIC design to minimize loss and phase noise.

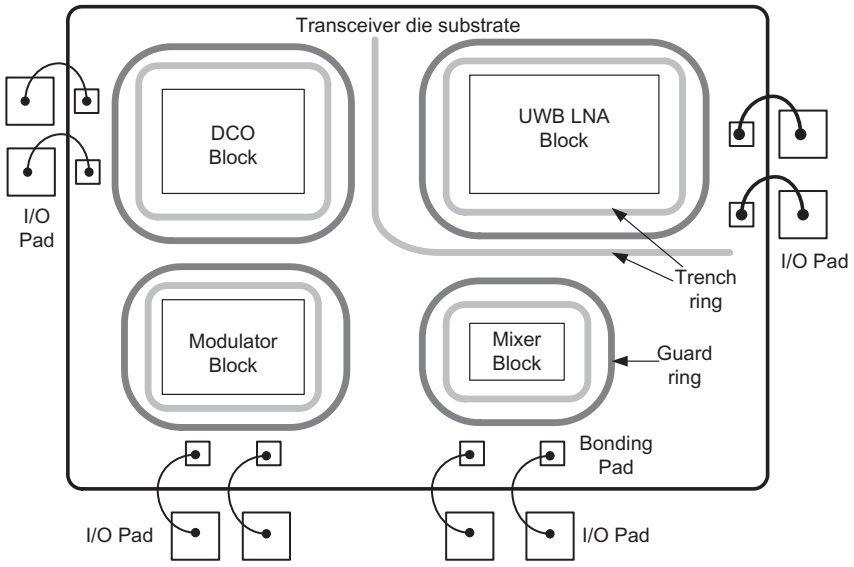

Figure 2.14: Isolation techniques in UWB transceiver die

2.6.2 Isolation Between Circuit Blocks in SoCs

The performance of the overall transceiver SoC mainly relies on the isolation between different circuit blocks on a same substrate. Poor isolation brings cross-talk or interferences between blocks, especially when digital and RF blocks are placed on the same die. A few methods for isolation include guard rings, grounding separations, and power separations.

The main cross-talk between each circuit block is coupled through the substrate on the same transceiver die since the electromagnetic energy is condensed in the substrate owing to a very high dielectric constant compared to other available passes, such as air. One very effective way to reduce this cross-talk is to apply a deep vertical trench between sensitive circuit blocks. The wider and the deeper the trench is, the better isolation will be. In addition to substrate trench, P+ or N well guard ring (substrate ring and guard ring) can further reduce the cross-talk and latch-up problems by collecting either injected electrons or holes. Figure 2.14 illustrates the trench ring and guard ring floor map for a transceiver die. Each block is surrounded by both trench and guard ring to maximize isolation. Studies show that the spacing between guard rings of different blocks starts to have less effect on the isolation when the frequency is above 1 GHz [48].

2.7 Summary

This chapter provides an overview of the UWB signal fundamentals and UWB radar transceiver techniques in CMOS technology. Two UWB signal categories are defined based on UWB signal generation mechanism. Choices of UWB radar detection methodologies such as AOA, RSS, and TOA are introduced. UWB radar transceiver architectures based on energy detection method are proposed and discussed. The design fundamentals such as the RLC circuits characteristics and circuit blocks isolation issues, are briefly introduced. An overview of the UWB radar sensor network model is briefly discussed as well, followed by RF design considerations.

Part III

Designs & Implementations

Chapter 3

Impulse Ultra-Wideband Radar Transmitter

3.1 Introduction

As seen in the last chapter, the time domain short pulses are used for UWB radar sensing. One of the most challenging parts of UWB transmitter design in an UWB system is the generation of an UWB pulse on chip. This leads to two specific tasks: (1) achieve large signal bandwidth and generate pulses at sub-nanosecond time scale; and (2) generate UWB pulses with low power consumption and low circuit complexity.

As aforementioned in Chapter 2, UWB signal generation is generally classified into two types: IR-UWB and CB-UWB. The IR-UWB transmitter is the main exploration in this chapter. The advantages of IR-UWB signal are that the IR-UWB transceiver architecture often is very simple and consumes a little amount of power. The signals do not have any carrier. These pulses can be modulated by polarity, amplitude, time position, or other characteristics. In early development of the IR-UWB transmitter, the UWB pulse was generated using combinations of lumped components, step recovery diodes, and discrete transistors at board level [12, 7, 50, 51, 52]. These methods of pulse generation do not have good scalability and usually have significant ringing effects due to the mismatch of long wiring interconnect on board. The cost is high (when it comes to the point of volume production), power consumption is high, and it lacks re-programmability. Latest advances in CMOS technology provides the potential to achieve UWB pulse generation on silicon chip. The fast logic gates with excellent timing controllability in the standard CMOS process enables the realization of an UWB pulse with good re-programmability.

Currently, there are two types of on-chip IR-UWB pulse generation: one is baseband-generated pulse or mono-cycle pulse, such as Gaussian pulse, Rayleigh pulse, or Hermitian

pulse; another is baseband-based poly-cycle pulse, such as higher-order Gaussian derivative pulse. The signal spectrum is determined by the pulse duration and waveform shapes. The first type of pulse generator generally occupies lower UWB frequency band (3-5 GHz). Most of them neither control pulse width nor pulse amplitude. Additionally, some of these pulse generators need on-chip passive filters which occupy a large die area [53, 54]. The work in [55] uses large on-chip RF choke inductors to approximate Gaussian pulses. The proposed Gaussian pulse transmitter in this chapter tries to solve these problems and improves the power and area performance for radar applications by using only transistors, resistors and capacitors. The proof of concept through chip implementation and measurements is present in this chapter as well.

A few poly-cycle pulse generation techniques are based on a high speed digital-to-analog converter to synthesize poly-cycle waveforms [56, 57]. This approach requires a high sampling rate (20 GS/s) and high speed complex circuits consuming extremely high power. Other multi-cycle techniques include digital switching and carrier pulse-modulation, which are more formally categorized in CB-UWB, and will be discussed in Chapter 4. In the second part of this chapter, a poly-cycle pulse transmitter based on a multiple pulse edge combining technique is proposed. This all-digital poly-cycle pulse generator consumes less power and has great potential for reconfigurability.

This chapter focuses on the design of an IR-UWB Gaussian-shape pulse transmitter and the design of an IR-UWB higher-order Gaussian pulse transmitter. This chapter is organized as follows: Section 3.2 presents the UWB Gaussian impulse characteristics and pulse analysis. Section 3.3 presents the UWB Gaussian impulse transmitter design and implementation. Section 3.4 presents the UWB high-order impulse transmitter design and implementation, and design issues are discussed. Section 3.5 provides measurement results of the fabricated UWB transmitter chip. The chapter summary is drawn in the Section 3.6.

3.2 IR-UWB Pulse Characteristics

Among various UWB systems, the impulse radio UWB family is selected for its simple complexity and easy implementation using standard CMOS for bio-radar sensing and sensor network applications.

Since the only restriction of UWB design is the FCC UWB emission mask and there is no such a regulation describing the shape of the UWB waveform, the transmitted pulse shape choice is left to the designers to decide as long as the pulses meet the FCC spectral limit.

3.2.1 Gaussian Pulse

In the transmitter design, a simple criteria for transmitting a pulse is the absence of DC components within the spectrum mask. Since there is no other specific constraints on the shape of the pulse for transmission as long as the pulses meet the spectral mask, there are a lot of choices for UWB pulses such as Gaussian pulses, Rayleigh, or Hermitian pulses. Among the possible pulse waveforms, the Gaussian pulse and its derivatives are the most commonly used pulse shapes in an UWB system because of their desirable frequency characteristics and their ease to generate and control [59].

A Gaussian pulse has a waveform envelope that is quite similar to the Gaussian function, and can be expressed as

$$V(t) = Ae^{-2\pi(\frac{t}{\alpha})^2} \tag{3.1}$$

where A is the pulse peak amplitude and α is the pulse shape factor controlling the pulse width. Decreasing α decreases the pulse width, which in turn increases the pulse bandwidth in the frequency domain. Equation (3.1) is depicted in Figure 3.1 (a). In the frequency domain, the Fourier transform of the Gaussian pulse *V(t)* can be expressed as

$$V(f) = \int_{-\infty}^{\infty} |V(t)e^{-2\pi jft}|dt = A\alpha e^{\frac{-\pi}{2}(f\alpha)^2} \tag{3.2}$$

Since the Gaussian function is an exponential function, its integral is also in exponential form. The center frequency of the pulse is inversely proportional to the pulse width. For a pulse with a pulse width of t_0, its center frequency is f_0=$1/t_0$.

The normalized Gaussian pulse energy E is calculated from the pulse amplitude V(t), assuming the load resistance is one Ω. The Gaussian pulse energy E can be expressed as

$$E = \int V(t)^2 dt = \int A^2 e^{-4\pi(t/\alpha)^2} dt = \frac{A^2\alpha}{2} \tag{3.3}$$

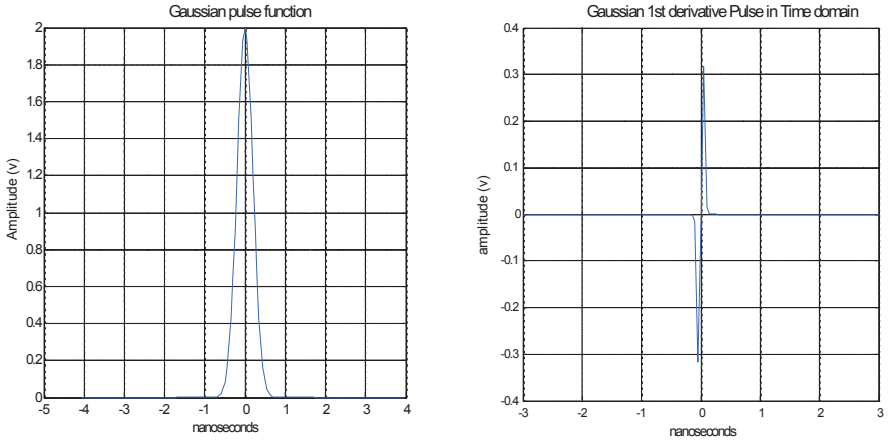

Figure 3.1: Single Gaussian pulse and its first derivative (Matlab source code obtained from [60])

where the unit of V(t) is volts, and E is in joules.

3.2.2 Gaussian Pulse Derivatives

There are three ways to control the energy spectrum of a pulse signal: changing the pulse width, differentiating the pulse, and combining the pulses. The spectrum of the Gaussian pulse can be adjusted by taking derivatives of the pulse.

Taking the derivatives of Gaussian pulse in time domain will shift the center frequency upwards in frequency domain. The n-th order Gaussian derivative has a center frequency

$$f_{center} = \sqrt{n}\frac{1}{\alpha\sqrt{\pi}} \tag{3.4}$$

which is derived from the property of the fourier transform

$$X_n(f) \propto f^n \exp(-\pi f^2 \alpha^2/2) \tag{3.5}$$

As the derivative order increases, the peak frequency goes higher. As an example, Figure 3.2 (a) shows the pulse shapes of the first 15 Gaussian pulse derivatives. Figure 3.2 (b) shows the corresponding energy spectrum.

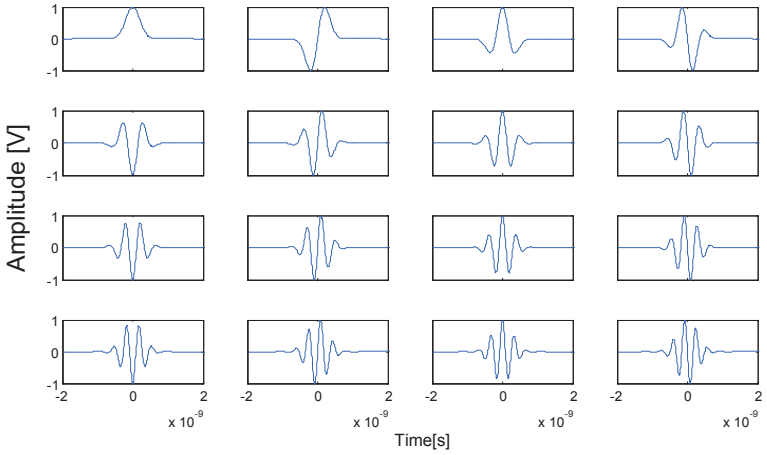

(a) Gaussian pulses and its derivatives in time domain

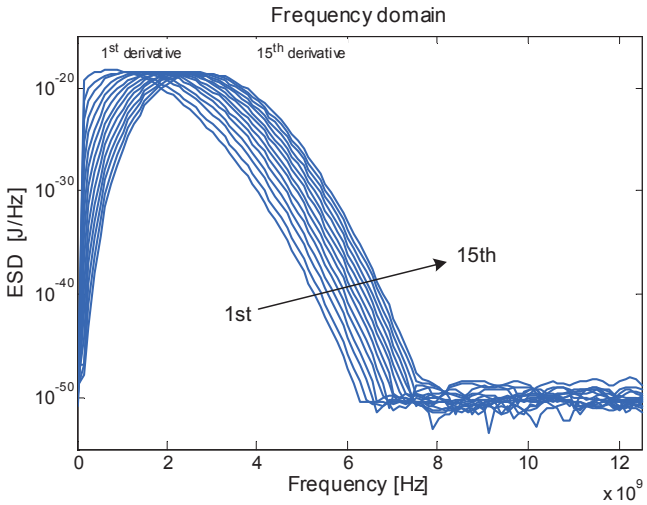

(b) Gaussian pulses and its derivatives in frequency domain

Figure 3.2: Gaussian pulses (a) Gaussian pulse and its derivatives in time domain [60]; (b) Gaussian pulse and its derivatives in frequency domain (Matlab source code obtained from [60])

3.2.3 UWB Pulse Design

The wide bandwidth and excellent distant resolutions of the UWB signal provide an excellent signal reflection response of a complex target. These properties benefit target localization. The impulse radio UWB signal is characterized with either extremely short pulse width in time domain or very complicated wave shape containing multiple frequency components, or both. The ability to distinguish between angle, time, and frequency resolution is unique.

The spectrum shape of a sequence of pulses is mainly determined by the pulse waveform itself. Changing the pulse rate has little influence on the spectrum shape, but affects the

separation of the spectral beams [61]. Thus, the design can be approached by designing single pulse [61]. As seen above, a very interesting property of the impulse UWB signal is that the desired frequency spectrum can be acquired through modifications of the pulse shapes. These modifications include pulse width variation, pulse differentiations, and pulse combinations [58]. Analysis in [60] shows the higher orders (5th or upper) derivative of Gaussian pulse concentrate most of their energy in the upper UWB band (from 5 to 10 GHz) [60]. Thus for the targeted spectrum mask, a higher order Gaussian derivative is required if no pulse-shaping filter is involved.

As for bio-radar sensing, the lossy biological propagation media requires that the special cares must be taken when choosing the energy pulse to minimize the multipath effect and single path wave shape distortion caused by the dispersive channel [62]. The multipath effect is much less problematic in impulse UWB system because of the very low duty-cycle of the transmitted pulse. Because the time interval between each pulse is longer than the pulse width itself, the pulse reflection has a low chance to overlap the transmitting pulse. The single path wave shape distortion is unique in the UWB system [62, 63]. Single path distortion in an UWB system is more frequency-dependent because of the different signal delays at different frequencies as a result of diffraction and media absorption inside human tissues.

If the single path distortion does not exist, the shape of the short impulse waveform remains the same during propagation. The conventional communication theory is often based on the assumption that there is no single path distortion during signal propagation. Thus received pulses are identical of the transmitted pulse [64]. However, in reality, the single path distortion starts to show influence as the signal bandwidth increases. Therefore, it requires careful choice of transmitter pulse and also the template for the correlator of the receiver (for coherent case). To reduce this single path distortion, the spectrum of the desired pulse should be limited to a relative narrow bandwidth inside the usable spectrum mask, while a low-complexity architecture and power consumption of the pulse generator remains.

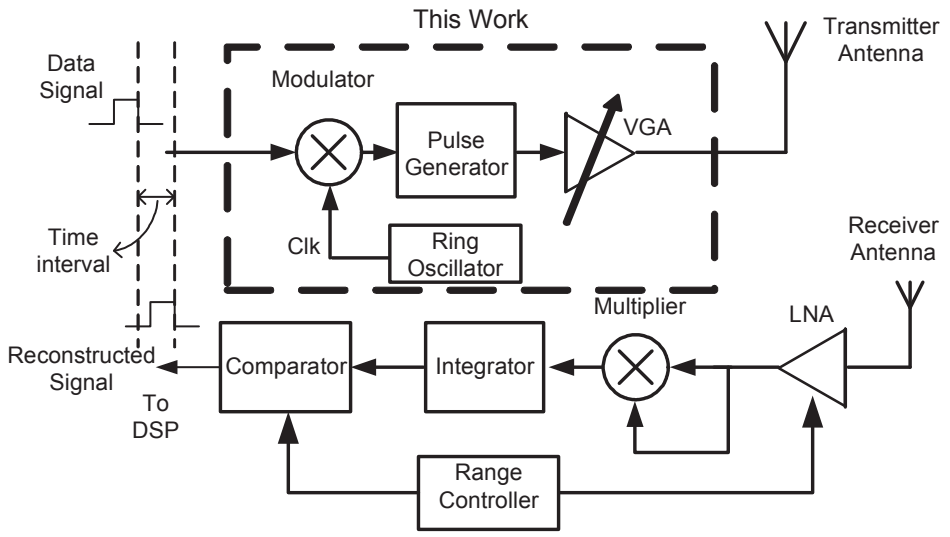

Figure 3.3: Proposed IR-UWB transmitter block diagram in dashed line

3.3 UWB Gaussian Impulse Transmitter Design

3.3.1 Gaussian Pulse Transmitter Architecture

Figure 3.3 shows the block diagram of the transmitter and receiver. This proposed radar architecture employs an On-Off Keying (OOK) modulation scheme with a non-coherent receiver structure [65]. The transmitter includes a modulator, a pulse generator, a variable gain amplifier (VGA) driver, and a ring oscillator.

The proposed impulse-based UWB technique enormously reduces the circuitry complexity and power consumption. An on-off keying (OOK) modulation scheme is used to modulate the pulse. The VGA and driver are used to amplify and adjust the output pulse width, as well as the impedance matching. The incoming data is modulated with a clock train generated by a ring oscillator, yielding a sequence of clock pulses. This modulated clock train then enters the pulse generator to produce a pulse train. This pulse train is passed onto a driver amplifier and then to an UWB antenna. The output pulse amplitude is adjustable through the variable gain amplifier in the driver. The range controller uses logic gates to switch on/off the VGA. The transmitter was fabricated using CMOS 90 nm process and the whole design consumes less than 0.5 mA of static current.

In this proposed architecture, the Gaussian pulse waveform is chosen to relax the com-

plexity of the pulse generator. The transmitter antenna behaves as a differentiator. The received Gaussian pulse at the receiver side has the form of the first derivative of the Gaussian pulse and can be expressed by Equation 3.5. The expected Gaussian pulse shape and its form in free space are shown in Figure 3.1.

The principle behind the non-coherent receiver is an energy detection method. Since there is no need for the synchronization mechanism, the adopted system structure is less expensive, simpler, and consumes less power. The wireless sensor network transceiver with coherent architecture has similar circuit blocks except it has an additional timing circuit and template signal generator. Compared to the non-coherent transmitter, the coherent one provides high performance and high sensitivity, but is more complex and more expensive to implement. Therefore the coherent structure is only selected for the sensor communication transceiver. As a part of the whole transceiver design, this chapter focuses on the non-coherent transmitter design for radar sensing.

The OOK pulse modulation is a special case of Pulse Amplitude Modulation (PAM). This modulation transmits a pulse if the information bit is 1, and transmits nothing if the information bit is 0. The modulated pulse sequence can be represented in time domain by

$$s(t) = \sum_{m=1}^{\infty} b_m \cdot P(t - mT) \tag{3.6}$$

where in this expression, ∞ shows the continuous number of transmitted bits, P(t) is the extremely narrow pulse, b_m stands for the information bit, either 1 or 0. T is the pulse period (pulse duration and the rest in one cycle). This modulation technique is applied in this design due to the low circuit complexity of the modulation and demodulation process. Multiple pulses are used to represent a single bit: this helps to combat noise and attenuation and makes the energy detection at the receiver side easier.

In the human body UWB radar sensing, the echo signals reflected from the targets are obtained directly in time domain for analysis. In the time domain, the received echo wave is normally the sum of reflected signals from different human body tissue layers. Different signal return time delays and return signal durations are associated with the target location, shape, and dimension [33]. Most importantly, since the electromagnetic wave propagation inside

human tissues greatly depends on the wave frequency, different tissue layers reflect signals at different frequencies. Therefore, the proposed Gaussian pulse transmitter with easy pulse timing control algorithm and wide frequency content can benefit the target detections.

Low Power Considerations

Power consumption is an important consideration in UWB radar sensing design for biomedical portable integrated device driven by a battery. In the proposed impulse-based UWB transmitter, the transmitter sends a pulse train towards the target. The interface between the dielectric boundaries causes a partial pulse reflection. Pulses are diffracted and scattered by different tissue layers and organs in human body. Study shows the around trip attenuation from the skin to the heart is approximately 40 dB [6]. This propagation distortion and attenuation easily destructs the reflected pulses and make them undistinguishable. To minimize this problem, and to minimize the device operation time, the gating mechanism using a time-control circuit is applied, ie., it allows the transmitter to send pulses then switch off and enter idle session until next pulse cycle. By using this mechanism, the receiver part (see Section 3.3.4) samples only the pulses arriving at the receiver during a very narrow time window after pulse transmission, as shown in Figure 2.8. Every time the transmitter sends out a pulse, and after this delay time, the receiver is turned on to receive the reflected signals. Then, the entire transceiver goes silent until the next cycle.

3.3.2 The Modulator and Pulse Generator

Figure 3.4 shows two critical components of the transmitter: the OOK modulator and the pulse generator. The clock signal Clk, generated by a ring oscillator, has a period of 1 ns and a pulse width of 500 ps. The clock train is modulated by the input data with OOK modulation by an AND gate. The number of pulses in one bit of data is determined by both the bit length, expected target distance and the clock frequency. Having more pulses to represent a single bit is easier for the energy-detection receiver to detect each single bit correctly. Figure 3.4 (b) illustrates the pulse generator and modulator circuits in the transistor level. All the transistor widthes and lengthes are the minimum size to ensure a very high cut-off frequency and a very small time constant.

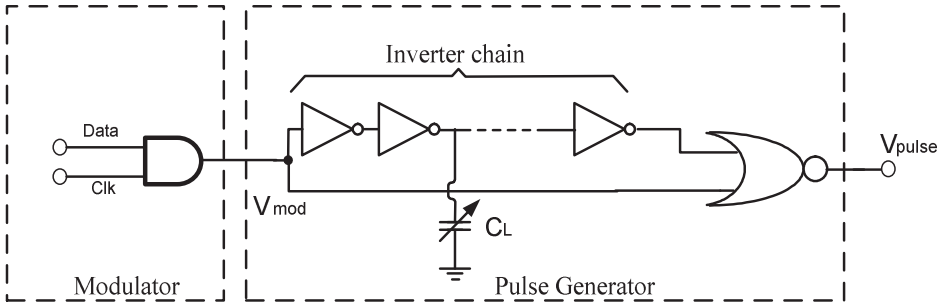

(a) Pulse generator and modulator

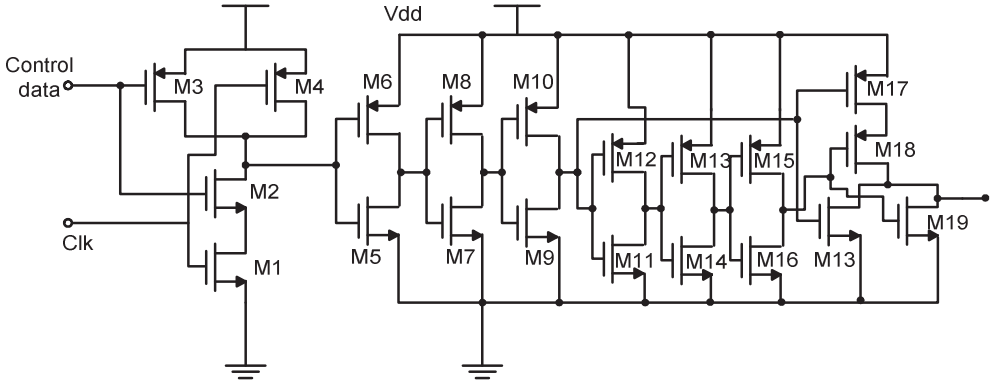

(b) Pulse generator circuit

Figure 3.4: Pulse generator and modulator circuit in transistor level: (a) Pulse generator and modulator; (b) Pulse generator circuit

The signal flow at each block of the proposed transmitter is illustrated in Figure 3.5. The transmitter clock signal is represented by A. And B is the input digital sequence. The modulated clock train passes through an inverter chain to sharpen the rising and falling edge of the the clock signal. The modulated clock train is then split into two signal paths and fed into a NOR gate. Signal in one path is inverted, as shown by C, and another signal is delayed, as shown by D. The NOR gate only outputs high when both inputs are low, and the time when both inputs are digitally-low is the delay time set by the inverter chain in the delay path. The signal E represents the output pulses. The output pulse width is determined by this delay time. The output pulse width can be adjusted by changing the delay of the inverters, which in turn can be adjusted, by varying the load capacitance of the inverters. Figure 3.6 shows the simulated pulses with various pulse widths when changing the load capacitance of the inverters. This load capacitance C is implemented using a CMOS varactor.

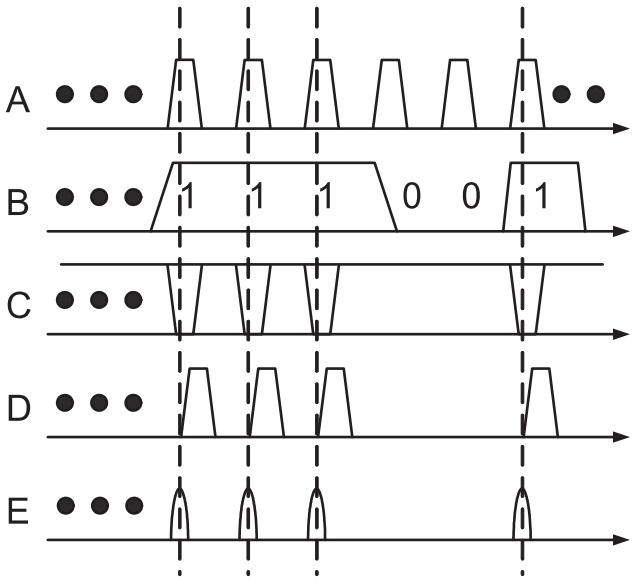

Figure 3.5: Principle diagram of Gaussian pulse transmitter signal flow

3.3.3 The Driver Amplifier with Variable Gain

The driver amplifier is used to amplify and shape the spectrum of the out-going short pulses, to adjust the transmitting pulse amplitude, and to match output impedance. As shown in Figure 3.7, the variable gain driver amplifier consists of three stages. The first stage employs three cascade common-source amplifiers with load resistors. Each amplifier is designed with relatively low gain to achieve a high bandwidth. The second stage consists of two cascade common-source amplifiers with PMOS transistors load. By analyzing the small-signal model of a cascaded common-source amplifier, the voltage gain can be represented as

$$A_V = \frac{-g_m Z_L}{1 + g_m Z_S} \tag{3.7}$$

For a MOS transistor biased in the linear region, a linear resistance is

$$r_{DS} \equiv \frac{v_{DS}}{i_D} = \frac{1}{\mu_n C_{OX} \frac{W}{L}(v_{GS} - V_t)} \tag{3.8}$$

The value of the resistance r_{DS} is controlled by varying the value of V_{con}. The overall gain

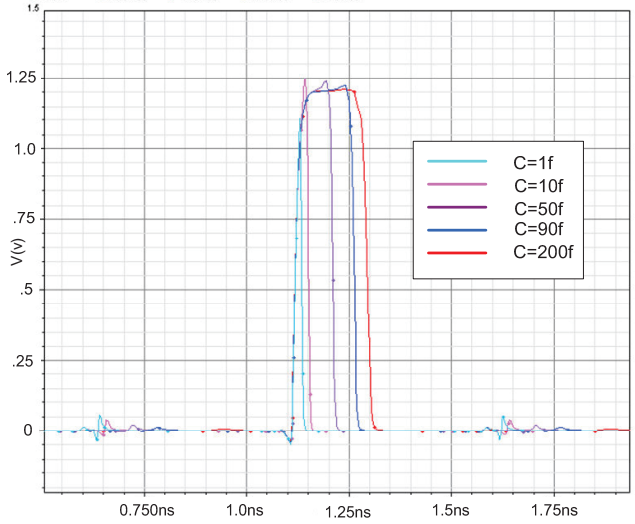

Figure 3.6: Simulation of different pulse widths

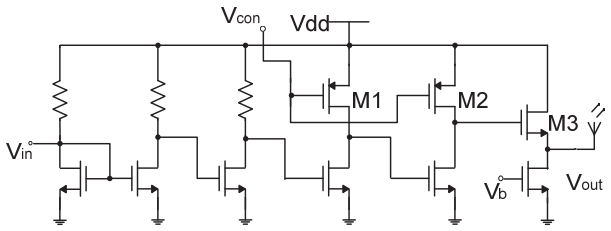

Figure 3.7: Output driver amplifier

of the driver amplifier is therefore

$$A_{driver} = \frac{-g_m Z_L - g_m \left(\mu_n C_{OX} \frac{W}{L}(v_{GS} - V_t)\right)^{-1}}{1 + g_m Z_S} \tag{3.9}$$

The two PMOS transistors M1 and M2 are tuned in the triode region and the equivalent resistances are controlled by the control voltage V_{con}, which equals to V_{GS} of the two PMOS M1 and M2. Simulation shows that the change of V_{con} from 0 V to 0.15 V corresponds to output pulse level from 30mV to 560 mV. The last stage is an output driver for 50 Ω antenna impedance matching purpose.

3.3.4 Energy Detection Based Receiver

For the sake of consistency with the transmitter design, this subsection briefly discusses the energy detection receiver, which is integrated on the same chip as well, as shown in Figure 3.3.

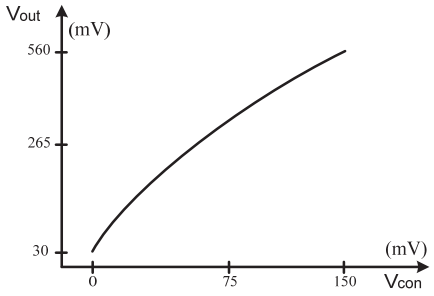

Figure 3.8: Output pulse amplitude vs. different control voltage

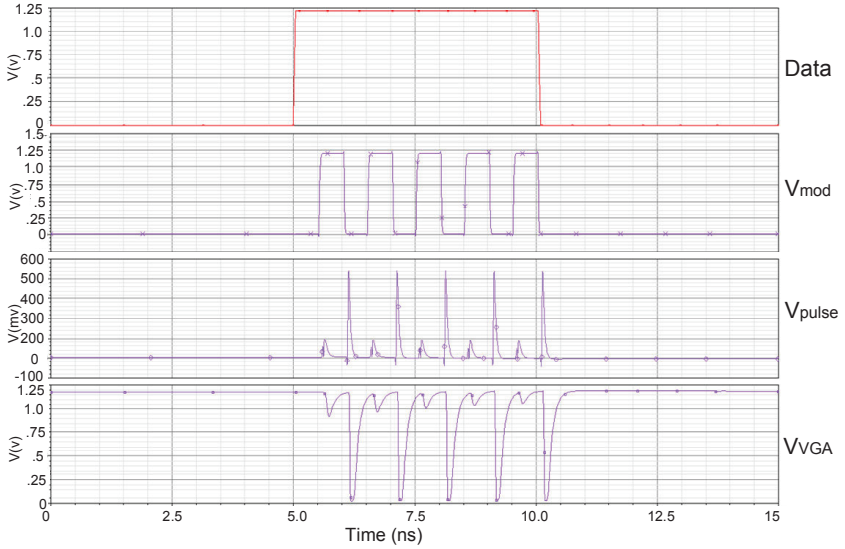

Figure 3.9: Simulated IR-UWB transmitter signal flow

This receiver includes a wideband LNA, a multiplier, an integrator, and a comparator.

The first block in the receiver is a LNA, which consists of two common-source, common-gate cascade amplifiers. The cascade configuration with inductive peaking improves the reverse isolation and frequency response. The sizes of the transistors are chosen to maximize the gain while maintaining low power consumption. A PMOS transistor switches the LNA on and off for gated idle operation.

A Gilbert cell is used to implement the multiplication function. For the non-coherent receiver, the correlator applies the received signals themselves as a signal template. An analog RC circuit is used as an integrator to collect the charges in a pulse train representing a symbol. The RC time constant is determined by the bandwidth of the data signals. By integrating the pulse train voltages, the voltage level of the received signal is more distinguishable from the noise. The integration time according to the single bit length can be

adjusted through a voltage controlled capacitor or a resistor R. The differential signal output from the multiplier cell is converted to a single-ended signal through a differential pair (a on-chip balun/transformer is another option).

A positive-feedback regenerative sense amplifier (latch), as shown in Figure 3.10, is employed as a clocked comparator because of its high sensitivity and low circuit complexity [69]. The NAND SR latch makes the output of the comparator changes only on the rising edge of the clock signal. The power consumption is depending on the switching frequency and the parasitic capacitance. Transistors M3, M4, M8 and M9 form a current flow through the amplifier to sense and amplify the voltage difference between the input voltage and the reference voltage [69]. The transistor sizes are chosen to be the minimum size to achieve maximum bandwidth, to reduce the hysteresis, and to reduce the power. The range gating signal is combined with the comparator clock by an inverter and an AND gate to control the sampling time of the comparator. The comparator samples the waveform only during the time window when the range gating signal is on. At other times, the receiver is turned off and the comparator is not functioning.

3.3.5 Transmitter Simulation with Energy Detection Receiver

The impulse UWB transceiver was designed and post-layout simulated using Cadence analog design environment. A 1.2 V DC was supplied to both the transmitter and the receiver. The clock signal was set to 1 GHz. The transmitted pulse width was 0.4 ns. A single data bit was set to 20 ns for radar sensing post-layout simulation, allowing 20 pulses in one bit, and 10 ns, allowing 10 pulses in one bit, for communications. The antennas were modeled as a capacitive-dominant RLC circuit and the antenna resistance R was 50 Ω [70]. Figure 3.11 shows the transceiver simulation setup. Two lossy transmission lines with different lengthes were used to represent the target movement during a certain time interval.

Figure 3.12 shows the post-layout simulation results for radar sensing. To reduce the simulation time, a target with much faster moving rate than the actual human skin was assumed here. T1 is the first time interval between output and reflected signals at the time when the target is close to the transceiver. T2 is longer than T1, indicating that the target moved further away from the transceiver. Different channel lengths in the simulations were

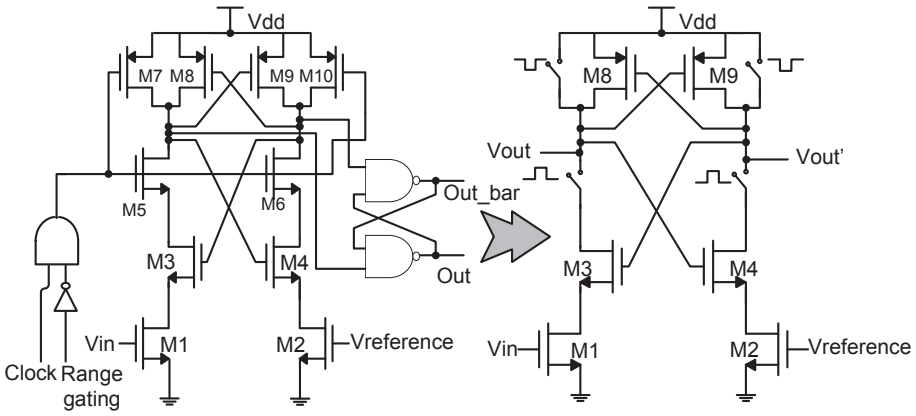

Figure 3.10: Clocked comparator

used to represent different target positions. The total power consumption of the transceiver in this case is 5.32 mW.

To simulate the transceiver for communications, the clock signal was set to 1 GHz. A transmitter input data pattern of "01000100110001011100" was used at the data rate of 100 Mbps. The signals at each transceiver internal node are illustrated in Fig. 14. V1 represents the modulated clock signal. V2 is the waveform before the driver amplifier, followed by V3 which is the signal at output of the impedance buffer. The amplitude of the signal at the output of the buffer amplifier is 300 mV. After the lossy channel, the pulse amplitude V4 is about 75 mV at the receiver front-end and the pulse V5 is amplified to 400 mV by the LNA. V6 is the output of the multiplier and V7 is the output after integration. The waveform amplitude before the comparator is 430 mV, which yields a significant signal-to-noise ratio. The final successfully-reconstructed data is represented by V8.

Three transceivers with minor modifications are integrated in one 1mm×1mm chip for testing purpose. To determine the overall sensitivity of the transceiver design due to process variations and mismatch, a Monte Carlo simulation at the input node of the comparator was run, and the result is shown in Figure 3.14. The simulation result shows a reasonable discrepancy that does not affect the comparator output. The total average power consumption of the transceiver is 21 mW. The Gaussian impulse transmitter is implemented using ST 90 nm technology, the chip layout is shown in Figure 3.15. The transceiver core layout is 0.3 mm^2.

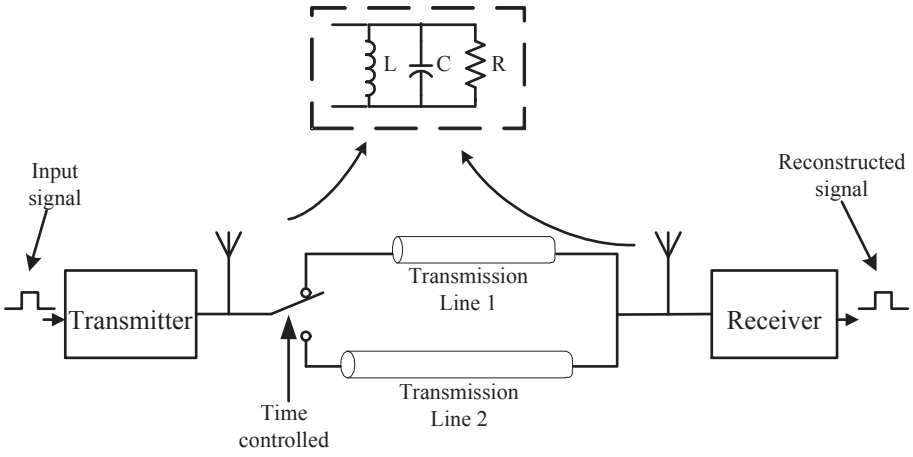

Figure 3.11: Transceiver simulation setup

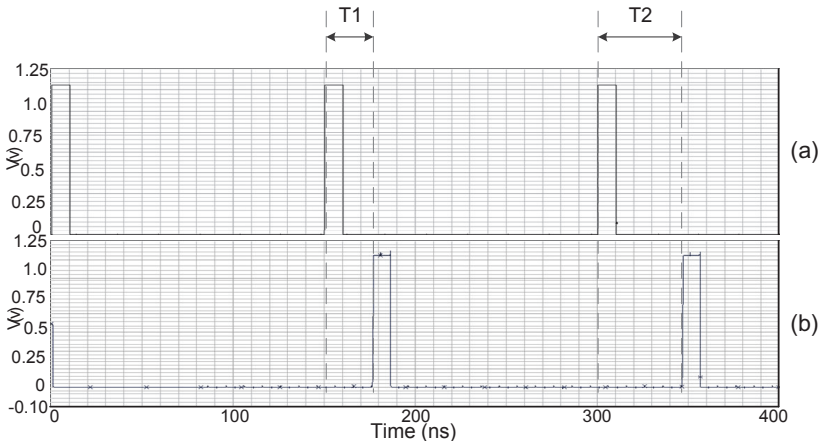

Figure 3.12: Simulated radar sensing waveforms: (a) input signals; (b) reconstructed signals from reflected pulses

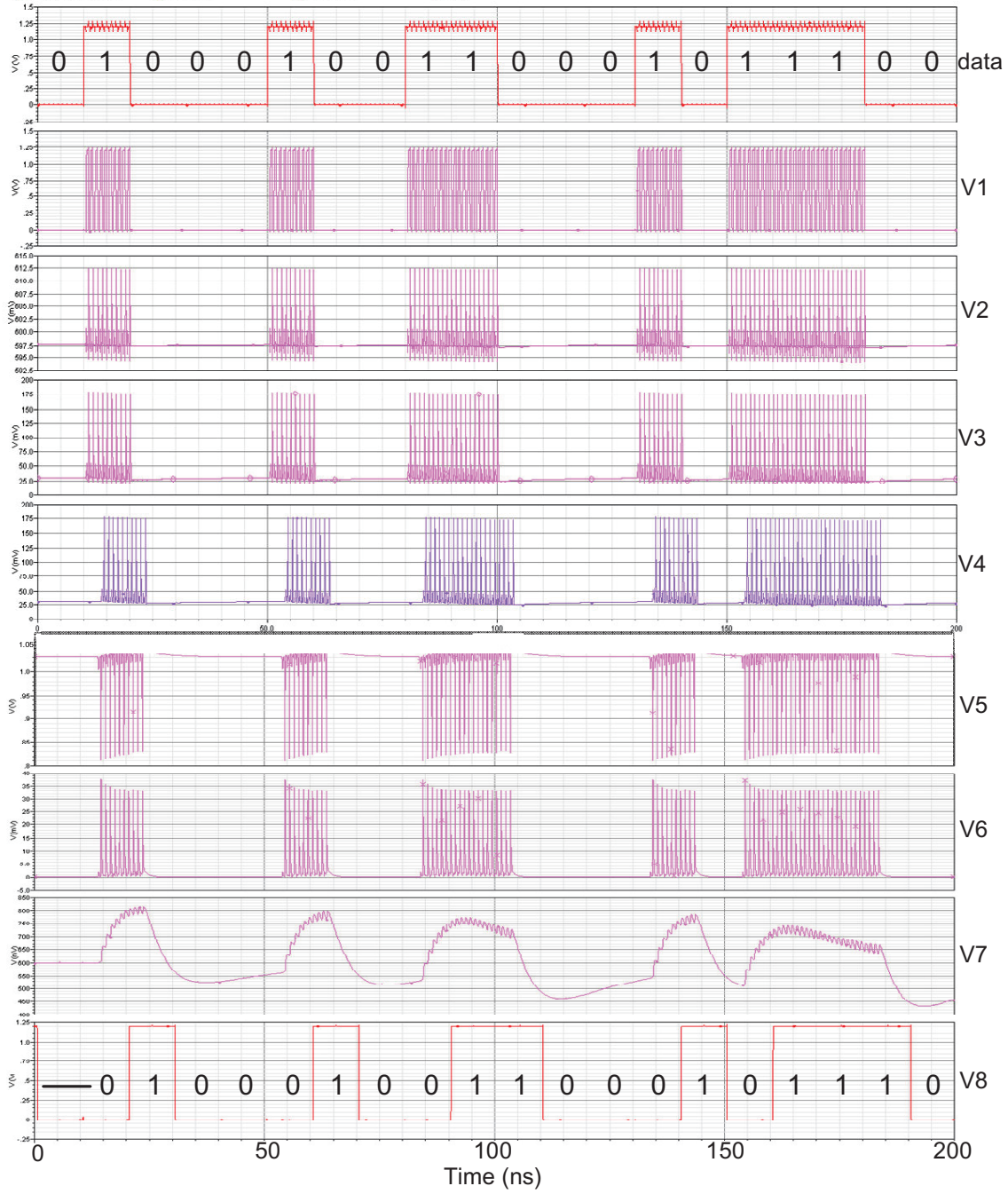

Figure 3.13: Simulated pulse signal transient waveforms at each circuit stage of the proposed IR-UWB Gaussian pulse transmitter and energy-detection receiver

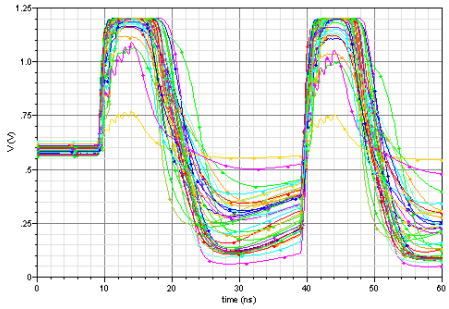

Figure 3.14: Monte Carlo simulation at the input of the comparator

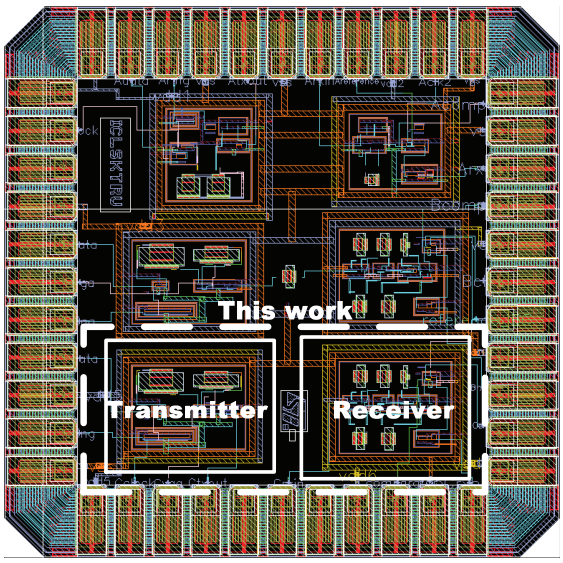

Figure 3.15: IR-UWB transceiver die layout

3.4 Higher Order Derivative IR-UWB Gaussian Poly-Cycle Transmitter

While the UWB Gaussian pulse transmitter earns its name for extremely simple complexity and low power, its disadvantages are also considered. Since the output UWB pulse has a broad bandwidth, a small variation of the pulse shape can critically affect the signal spectrum, and it can even violate spectral regulations. Thus, to exploit different upper frequency bands in UWB band allocation, and to have more degrees of freedom for spectra control, a reconfigurable poly-cycle pulse generator is highly desirable. In this section, an IR-UWB transmitter with OOK/BPSK modulation using higher order Gaussian poly-cycle pulse with digital circuit implementation is proposed. This transmitter outputs tenth-order Gaussian derivative BPSK-modulated pulses.

3.4.1 UWB High-Order Pulse Design

As seen in previous sections, the energy of a Gaussian pulse is mostly condensed at a lower frequency starting from DC. Most of the pulses generated are the Gaussian pulse or lower order Gaussian derivatives [18, 21, 22, 23, 66, 75, 76, 77], which can not completely and efficiently fulfill the FCC spectrum mask requirement. In order to transmit the pulse in a more efficient way, a higher order Gaussian derivative pulse is desired as the baseband signal. This motivates the development of the UWB high-order poly-cycle pulse transmitter.

While taking all the factors, such as spectrum mask, complexity, power consumption, and distortions, into consideration, the higher order Gaussian derivative pulse, such as a tenth-order derivative pulse, is suitable for the proposed transmitter. In terms of physical implementation, the higher order Gaussian derivatives have the very similar effect as the modulation of a higher sinusoidal carrier frequency by an equivalent Gaussian envelop both in time domain and in frequency domain except the former has less complexity and needs less power and no start-up time [82]. In the proposed transmitter, an all digital tenth-order derivative of Gaussian pulse is generated. The expression of a normalized tenth-order

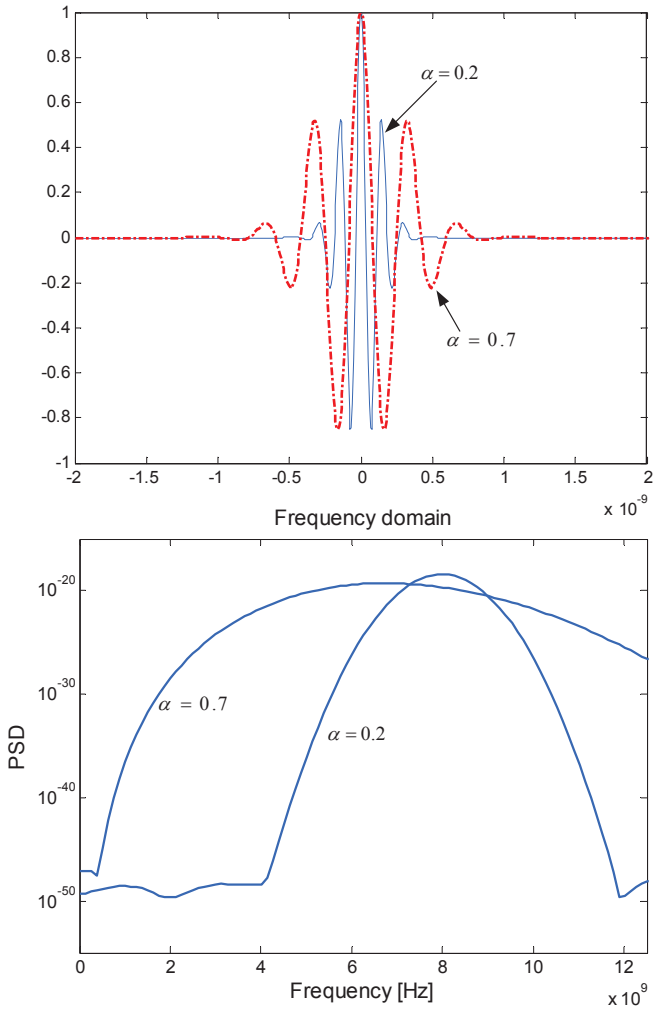

Figure 3.16: Tenth derivative of Gaussian pulse: (a) normalized pulses with different shape factors; (b) normalized pulses in frequency domain with different shape factors

Gaussian derivative can be derived from Equation (3.1) as

$$V_{pulse} = -1024\pi^5 t \cdot \exp\left(\frac{-2\pi t^2}{\alpha^2}\right) \cdot \left(\frac{945}{\alpha^{10}} - \frac{5040\pi t^2}{\alpha^{12}} + \frac{6048\pi^2 t^4}{\alpha^{14}} - \frac{2304\pi^3 t^6}{\alpha^{16}} + \frac{256\pi^4 t^8}{\alpha^{18}} \right) \quad (3.10)$$

Here α is the shape factor. Figure 3.16 shows the waveforms and spectra of two tenth-order Gaussian derivative pules with different α. As seen from the Figure 3.16 (b), a lower α pulse has a higher center frequency with a narrower bandwidth. Reducing the pulse width can achieve a spectrum inside the 6-8 GHz UWB band. When expanding the equation 3.10 into a polynomial form, it can be seen that it is represented by combinations of different Gaussian functions.

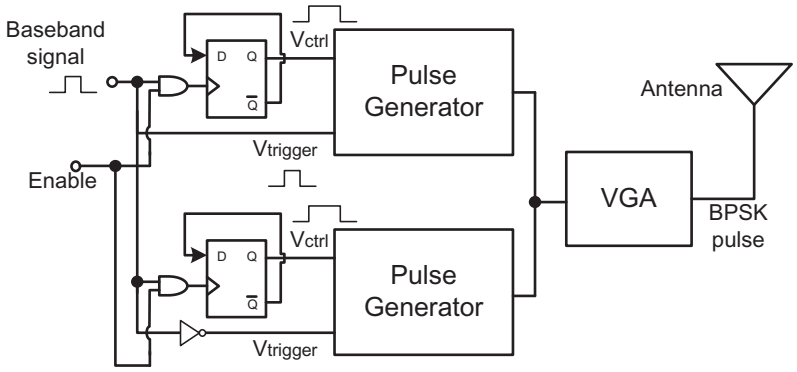

Figure 3.17: Proposed transmitter architecture

3.4.2 Higher Order Derivative Gaussian Impulse Generator Design

The proposed UWB high-order Gaussian pulse transmitter with pulse tuning capability is shown in Figure 3.17. The proposed transmitter consists of two Gaussian derivative pulse generators, a variable gain driver amplifier, and peripheral circuitry [83]. The input of the transmitter is the baseband signal. A D-type flip-flop as a frequency divider is used to expand the control signal for pulse generators. The baseband signal is also used to trigger the generation of a pulse. The baseband signals are BPSK modulated such that one pulse generator outputs positive Gaussian derivative pulses when the baseband signal is logic high, and the pulse generator outputs negative Gaussian derivative pulses when the baseband signal is logic low.

As seen from the transmitter block diagram, the proposed transmitter is not using any clock signals. This greatly reduces the power consumption of the circuit at the tradeoff of lower pulse repetition frequency (PRF), which is not the ultimate concern for the bio-radar sensing applications. The average transmitter output power emission in the UWB band is limited to -41.3 dBm/MHz. But due to the FCC wavier as mentioned in Chapter 2, gated UWB systems can also transmit at higher power levels and then sit quietly if the average emission power density during the time period still satisfies the power limitation. The enable signal in the transmitter controls the gating timing. This gated signal can then achieve the same average transmit power as a continuous signal while occupying only a fraction of the channel time available for transmissions in the UWB system.

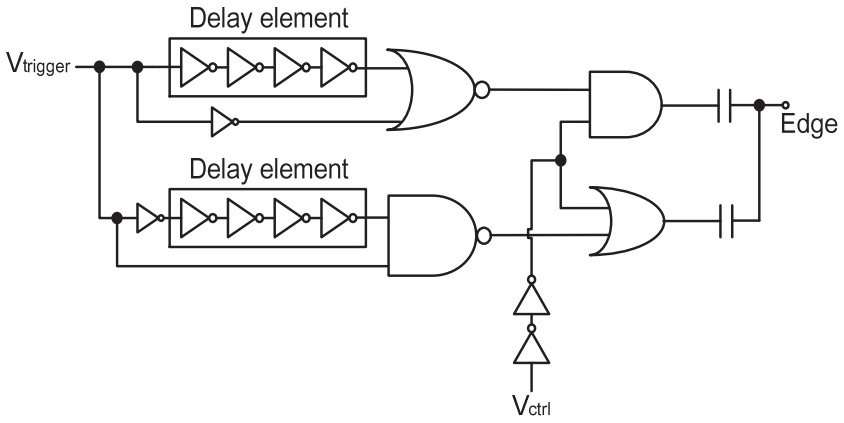

Figure 3.18: Edge generator circuit with edge tuning capability

3.4.3 Pulse Generator

The core component of the pulse generator is the edge generator, as shown in Figure 3.18. The edge generator generates the basic element which is the Gaussian pulse. Each rising edge of the $V_{trigger}$ trigger positively-peaked pulses through a NOR gate and negatively-peaked pulse through a NAND gate. The pulse width and pulse amplitude are controlled through the delay elements, as shown in Figure 3.19.

Figure 3.19 (a) shows a widely-used current starved inverter delay circuit. The delay of the inverter chain is controlled by the biasing voltage, which generates different turn-on resistance R_p and R_n. The propagation delay time t_p for a single inverter is approximately

$$t_p = 0.35(\tau_n + \tau_p) \tag{3.11}$$

where τ_n is the time constant of the NMOS transistors, and

$$\tau_n = R_n C_n \tag{3.12}$$

τ_p is the time constant of the PMOS transitors, and

$$\tau_p = R_p C_p \tag{3.13}$$

Since the turn-on resistance R is inversely proportional to the transistor g_m at triode region,

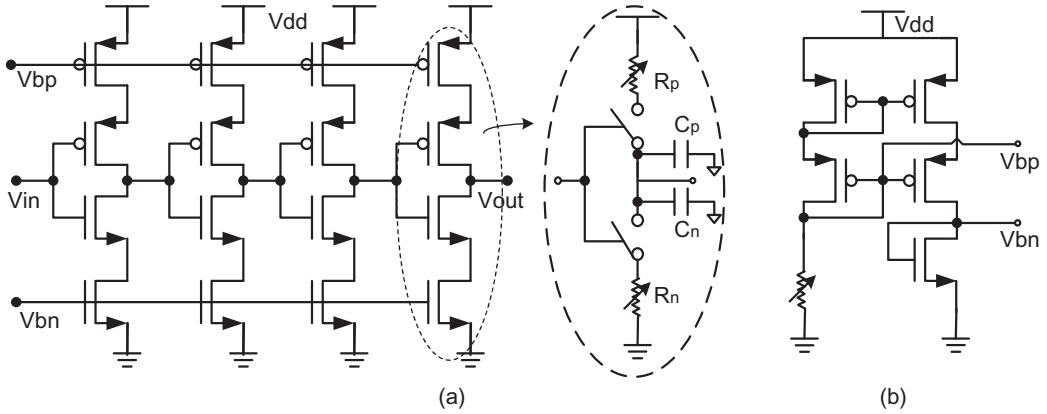

Figure 3.19: Delay element circuit: (a) Delay inverter train; (b) Cascode current mirror biasing circuit for the delay element

increasing the biasing current reduces R_p and R_n, thus reduces the delay time, and vice versa. The biasing current is controlled by a cascode current mirror shown in Figure 3.19 (b). The pulse width is adjusted by changing the bias current in the current mirror. The pulse generation logic is that when one NOR input is slower than the other NOR input, the time difference between these input produces a positive normally distributed voltage pulse (usually represented by Gaussian distribution), and when the inverted NAND input is slower than the other NAND input, the time difference of these two input produces a negative normally distributed voltage pulse. The polarity of the edge generator output is controlled by V_{ctrl}. The V_{ctrl} selects either the positive pulse to pass to output or the negative pulse to output through the AND and OR logic gates (AND and OR gates can be replaced by controlled transmission gates). Figure 3.20 illustrates the pulse generation principal and the waveforms at different points inside the pulse generator.

The Gaussian derivative pulse generator, as shown in Figure 3.21, consists of an array of edge generators connected in parallel. Each edge generator produces a single pulse with different amplitude and same pulse width T_{delay}. The delay in each edge generator is adjusted based on the shape factor of the tenth derivative of the Gaussian pulse. The control signal is inverted at the 2nd, 4th, 6th, and 8th edge generators to produce pulses with negative polarity at these locations. The trigger signal $V_{trigger}$ is delayed one pulse width T_{delay} at the input of the 2nd edge generator, delayed two pulse widthes $2T_{delay}$ at the 3rd edge generator, $3T_{delay}$ at the 4th edge generator, $4T_{delay}$ at the 5th edge generator, $5T_{delay}$ at the 6th edge generator, $6T_{delay}$ at the 7th edge generator, $7T_{delay}$ at the 8th edge generator, and $8T_{delay}$ at

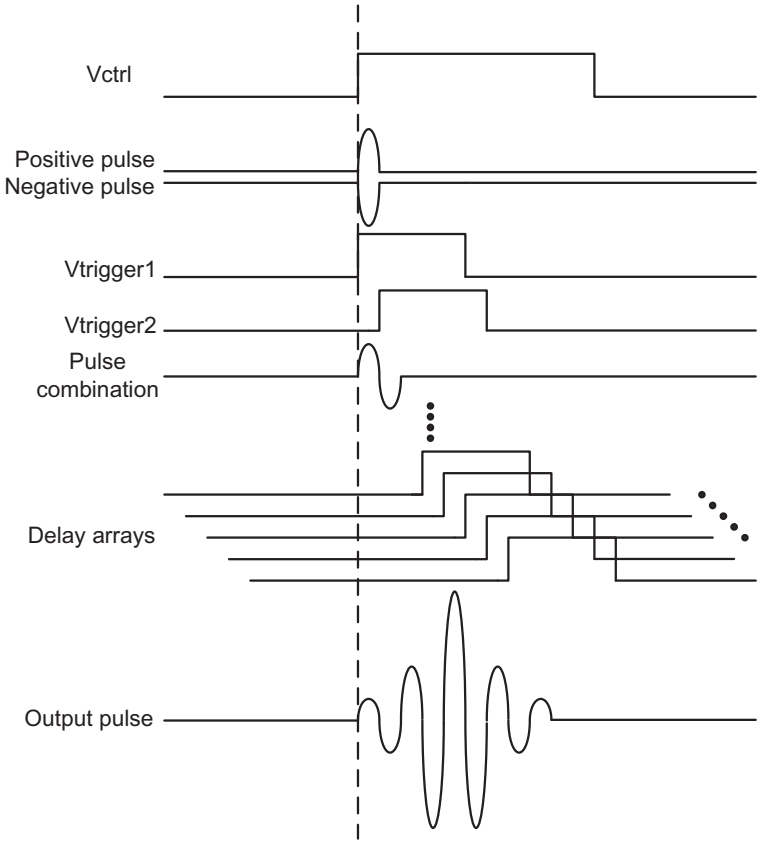

Figure 3.20: Waveforms of the control signal and pulses

the last stage. The final output of the tenth derivative Gaussian pulse is constructed based on each single edge generator output. The total pulse width is $9T_{delay}$.

The waveforms of the pulse generator are illustrated in Figure 3.20. The baseband signal is used as both V_{ctrl} and $V_{trigger}$. After a series of delay and add operations, the desired order Gaussian derivative pulse is constructed. The design is a transmitter prototype. It not only can generate tenth-order Gaussian derivatives, but any pulse combinations, either Gaussian derivatives or rectangular or Gaussian modulated sine pulses by controlling the delay elements in each edge generator and the number of edge generators used based on different orders of derivative of Gaussian pulse, the bandwidth, and the center frequency.

3.4.4 IR-UWB Bi-Phase Keying Transmitter Implementation

The transmitter prototype mentioned in last section was designed and simulated in TSMC 90nm CMOS with 1.0 V voltage supply. The baseband signal was generated at 100 Mbps to give enough relaxation for generating pulse. The positive and negative tenth derivative

Gaussian pulses were generated, as shown in Figure 3.22. The pulse width was adjusted to 0.5 ns through the delay components. The transmitter output peak-to-peak amplitude is 130 mV (a band pass filter was applied).

A Monte Carlos simulation was performed to validate the robustness of the transmitter circuit against process, voltage and temperature variations and mismatches. The Monte Carlos simulation results of the tenth-order Gaussian derivative pulses are shown in Figure 3.23. The simulated power spectral density plot of the transmitter output with simulated output filter added is shown in Figure 3.24. The majority of the pulse energy falls in the desired UWB band mask.

The layout of the proposed transmitter is shown in Figure 3.25 (a). The transmitter core occupies a chip area of 200 μm $\times$ 140 μm. Simulating on a 1 V voltage supply, the transmitter draws an average of 9.037 mW when generating the tenth-order Gaussian derivative pulses. The pulse width is 0.6 ns. The transmitter has an output pulse energy of 3.1 pJ/pulse.

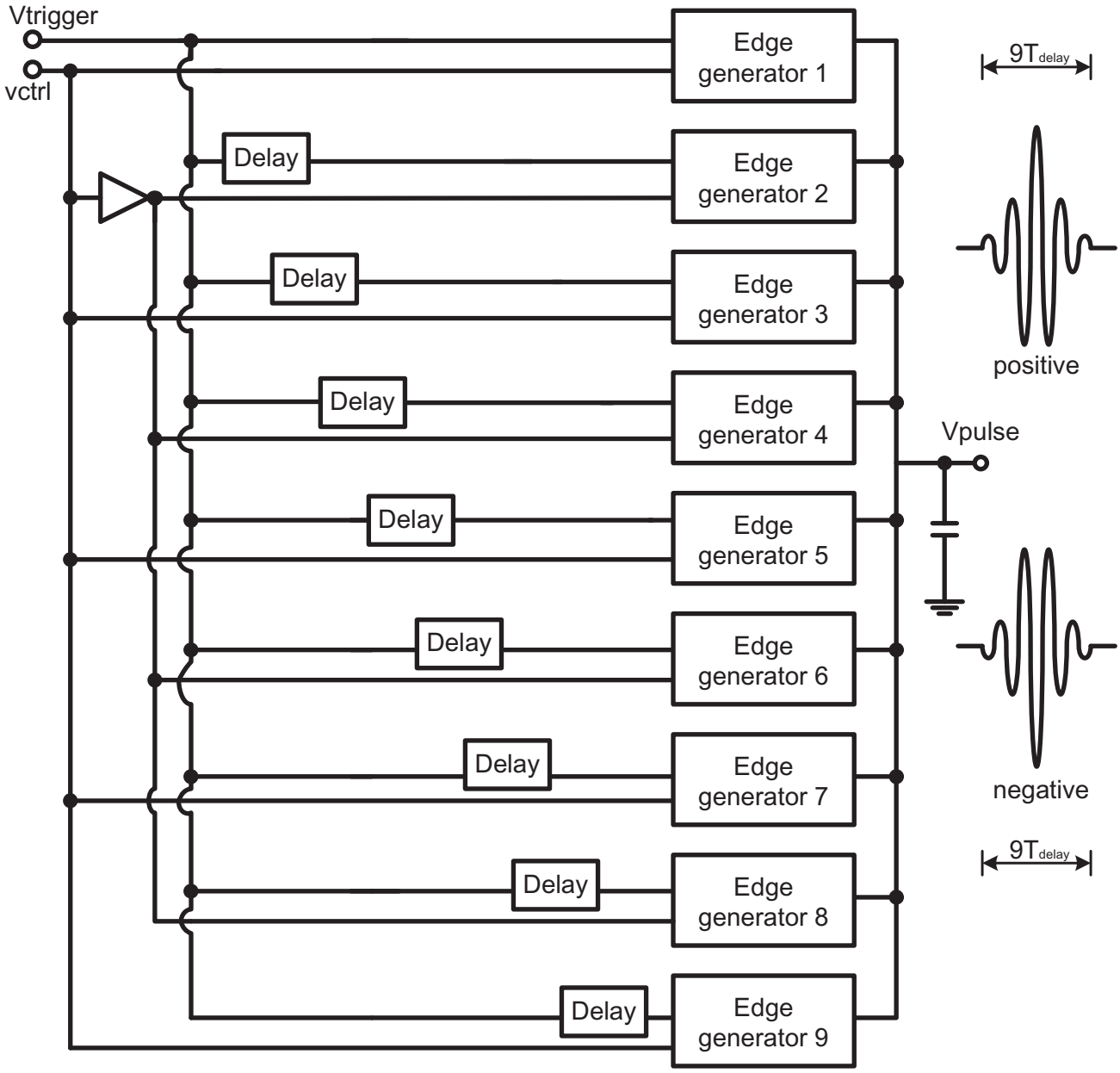

Figure 3.21: Block diagram of the all-digital BPSK pulse generator

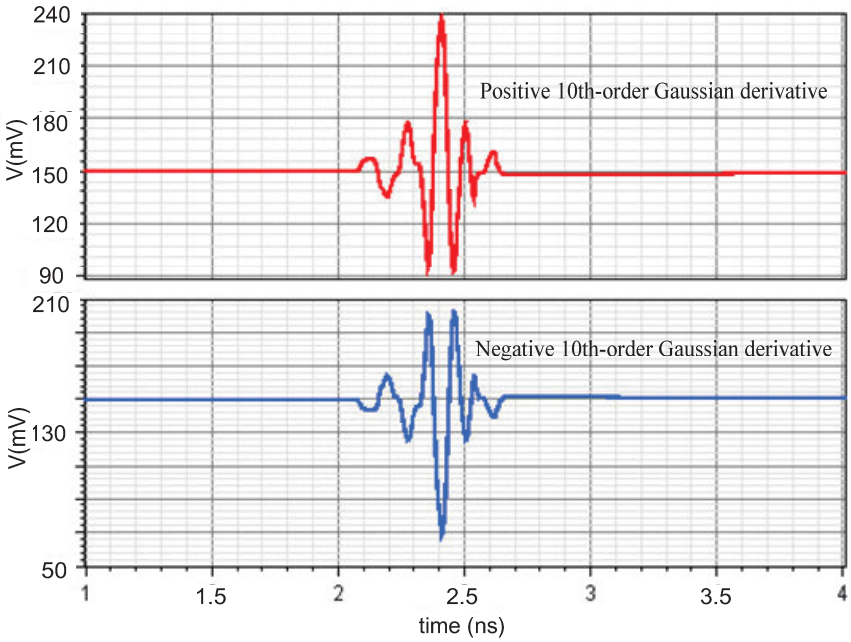

Figure 3.22: Simulated high-order Gaussian pulse

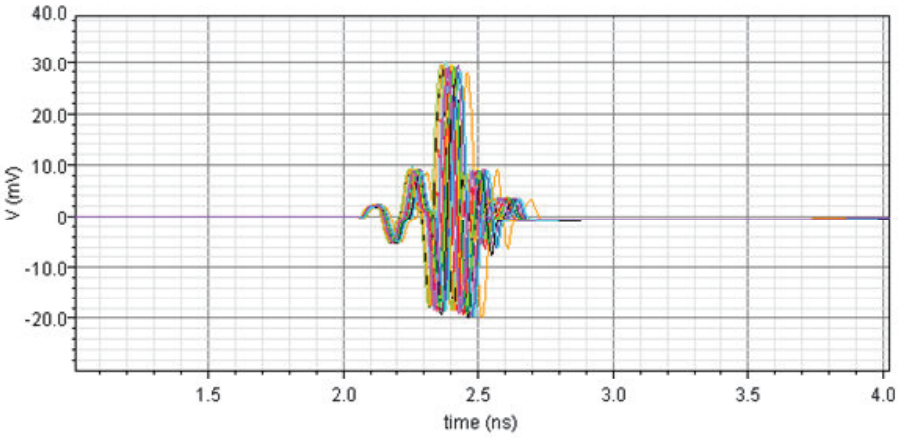

Figure 3.23: Corner simulation of high-order Gaussian pulse

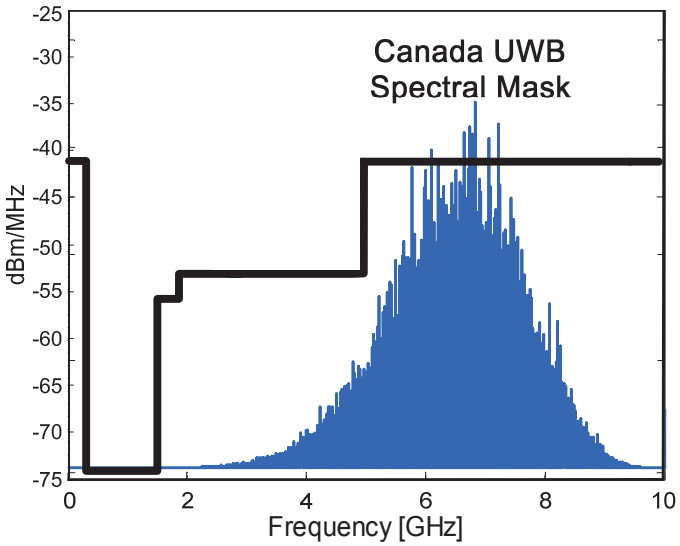

Figure 3.24: Simulated spectrum of Gaussian tenth-order derivative pulse

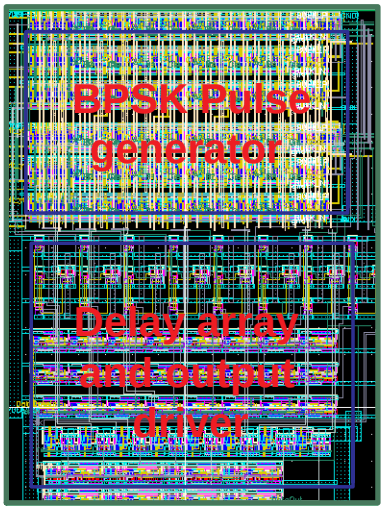

(a) Layout of the proposed digital transmitter

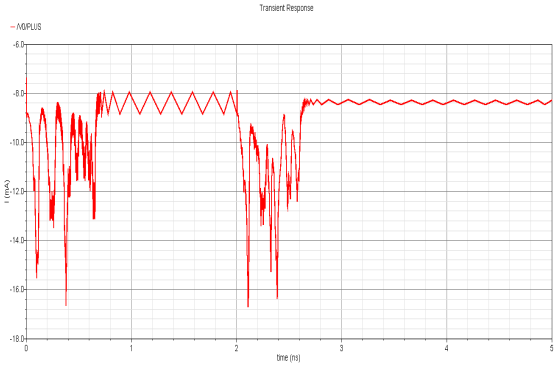

(b) Total power consumption plot

Figure 3.25: (a) Layout of the proposed transmitter; (b) power consumption

Table 3.1: Overall transceiver configuration

Parameter	Value
Process	TSMC 90 nm CMOS
Frequency lower bound	6 GHz
Frequency upper bound	9 GHz
Bandwidth	3 GHz
Pulse type	10th-order Gaussian derivative
Pulse duration	0.6 ns
Modulation scheme	BPSK
Transmitter power consumption	9.037 mW
Pulse energy	3.1 pJ/pulse
Active transmitter area	200 μm×140 μm
Test sensor communication data rate	100 Mbps

Table 3.2: Performance comparison of the proposed transmitter with previously published works

References	Pulse Type	Technology	Supply Voltage	Pulse Amplitude	Pulse Width	Power Consumption
[66] 2006	OOK Gaussian	CMOS 0.18 μm	1.8 V	800 mV	250 MHz	700 pJ/pulse
[75] 2006	OOK Gaussian	SiGe BiCMOS	1.8 V	170 mV	175 ps	132 pJ/pulse
[76] 2007	OOK Gaussian	CMOS 0.13 μm	1.8 V	350 mV	0.7 ns	30 pJ/pulse
[77] 2002	OOK 1st derivative Gaussian	Discrete	3 V	400 mV	300 ps	N/A
[78] 2006	BPSK 2nd derivative Gaussian	CMOS 0.18 μm	1.8 V	30 mV	1 ns	21 mW
[79] 2008	Multi-cycle	CMOS 0.18 μm	1.8 V	160 mV	1 ns	16.8 pJ/pulse
[81] 2009	Multi-cycle	CMOS 90nm	1.0V	165-710mV	NA	17.5pJ/pulse
[82] 2010	BPSK Fifth Gaussian derivative	CMOS 0.18 μm	1.8 V	500 mV	1.5 ns	27 pJ/pulse
[84] 2007	Multi-cycle carrier for MB-UWB	CMOS 90 nm	1.0 V	N/A	N/A	40 pJ/pulse
This work	BPSK 10th Gaussian derivative	CMOS 90 nm	1.0 V	30-500 mV	0.6 ns	9.037 mW(total) 3.1 pJ/pulse

3.5 UWB Gaussian Pulse Transmitter Fabrication and Measurement

The IR-UWB Gaussian pulse transmitter proposed in Section 3.3 was designed and implemented using the standard ST 90nm CMOS technology with 1.2 V power supply to verify its functions. A chip photograph of the fabricated test circuit is shown in Figure 3.26. The active transmitter area is 50 μm $\times$ 100 μm. The transmitter die is housed using a CQFP44 package. The fabricated impulse transmitter module is tested under a normal operating environment (room temperature). Figure 3.27 shows the measurement setup. For digital data input, a pattern generator is used to provide a 250 Mb/s bit sequence data. The internal clock generator of the transmitter provides a 500 MHz square wave clock signal. The output of the transmitter is connected to a high frequency oscilloscope through a sub-miniature version A (SMA) cable. The power supply of the chip package is 1.2 V.

In one of the tests, the pattern generator inputs a digital sequence with a pattern of 111001 at 250 Mb/s, as shown in Figure 3.28, to the transmitter module. The corresponding transmitter output pulses are shown in Figure 3.29 with the scale doubled. The first derivative of the Gaussian pulse at the receiver side is shown in Figure 3.30. Each pulse-width is 1 ns and has an amplitude of 177 mV. Figure 3.31 shows the measured output pulse waveforms of the implemented transmitter in another test where a single bit data is applied as an input. The pulse has a maximum amplitude of 521 mV at a 50 Ω load and a pulse width of 1 ns when the VGA control voltage was set at 0.14 V. Figure 3.32 is the measured output pulse with an amplitude of 357 mV and pulse width of 0.5 ns. The output pulse has a minimum amplitude of 30 mV when the VGA control voltage is 0 V.

The power spectral density of the transmitter modulated output pulse train is calculated using discrete Fourier transform on the measured UWB signal. Figure 3.33 shows the measured power spectrum of the output Gaussian pulses at four different pulse repetition rates with the FCC spectral mask. Table 3.3 lists the transmitter parameters, while Table 3.4 shows the performance comparison of the proposed transmitter with previously published works.

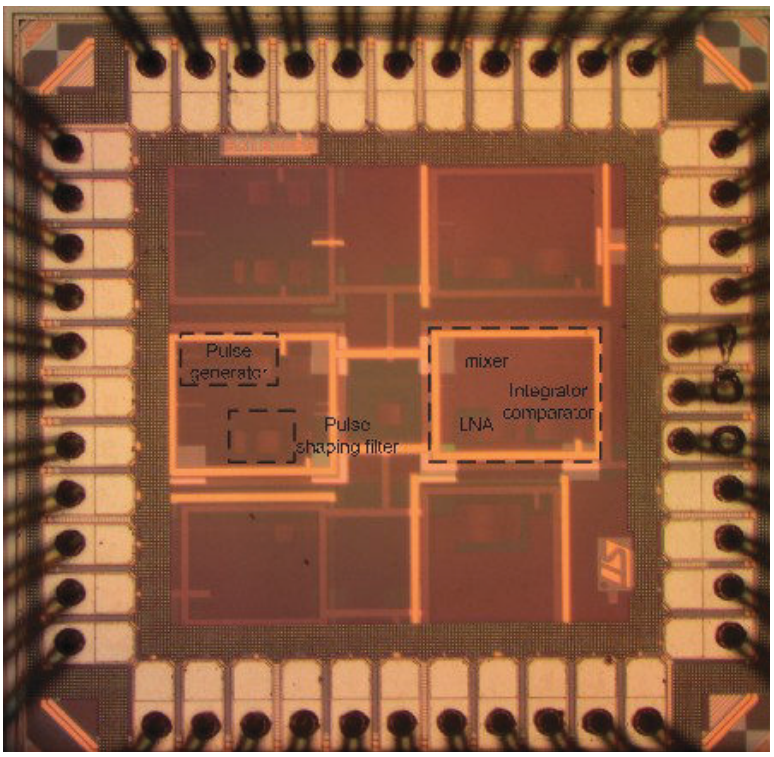

Figure 3.26: IR-UWB transceiver die micrograph

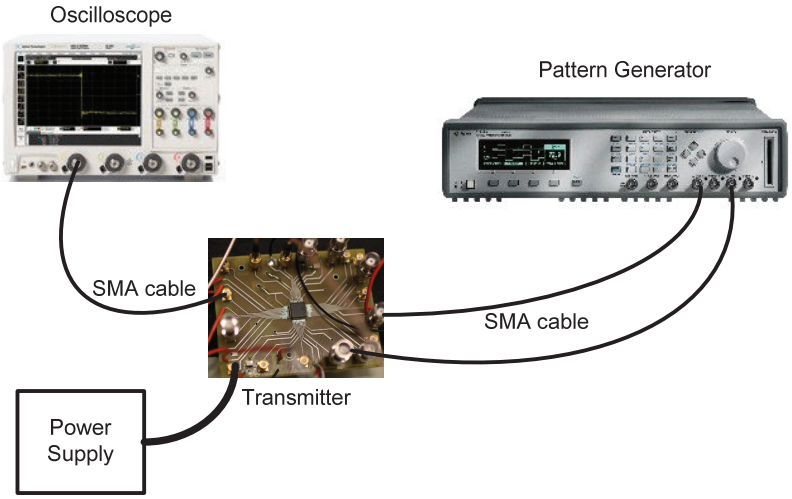

Figure 3.27: IR-UWB transmitter measurement setup

Figure 3.28: Input waveform

Figure 3.29: Measured transmitter output pulses

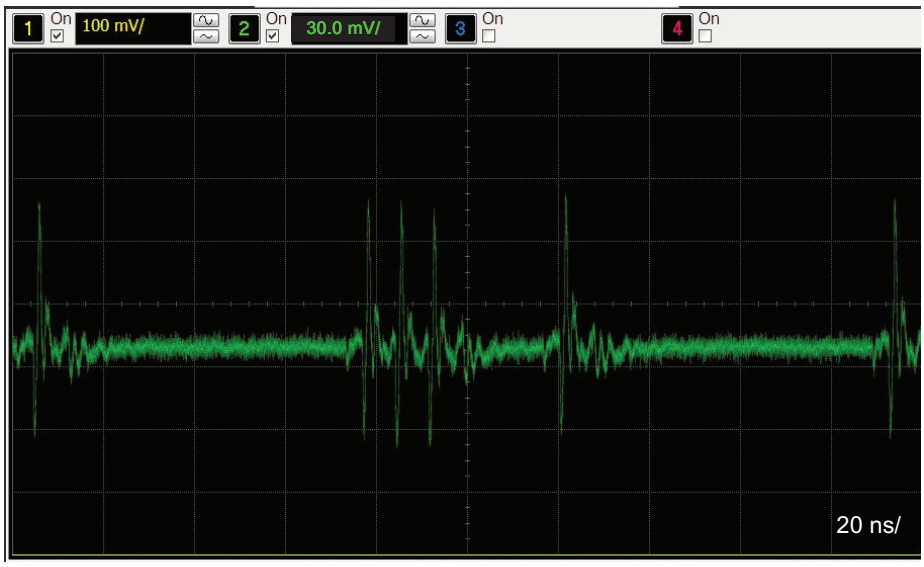

Figure 3.30: Measured first derivative of the pulses at receiver antenna

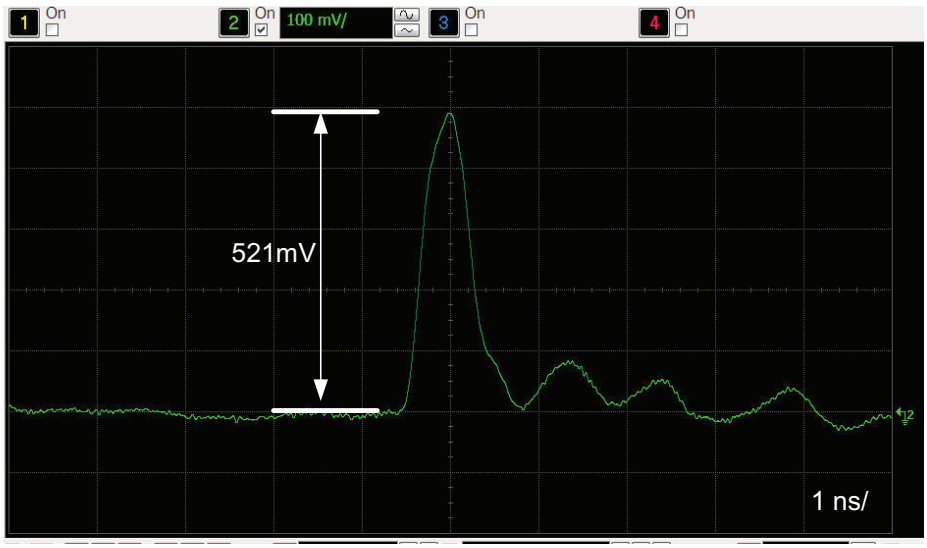

Figure 3.31: Measured single Gaussian pulse

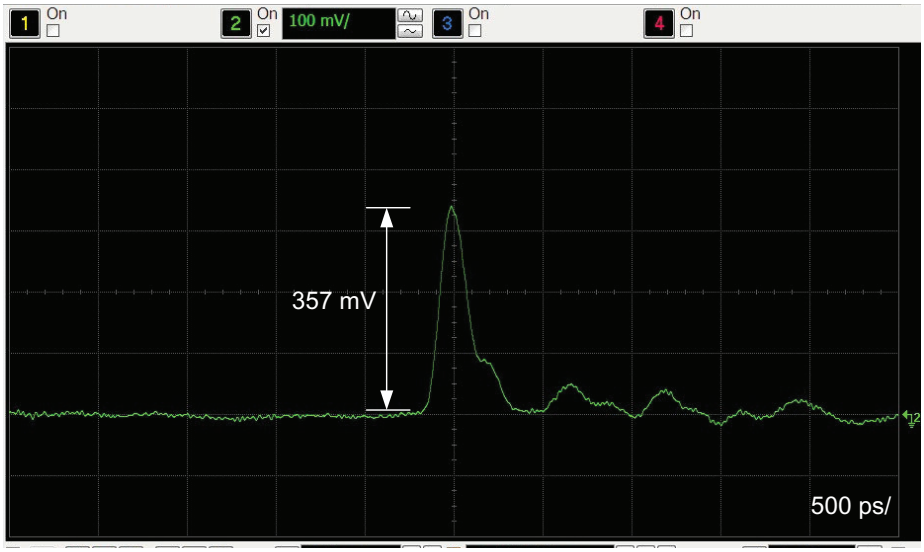

Figure 3.32: Single measured Gaussian pulse with different amplitude and pulse width

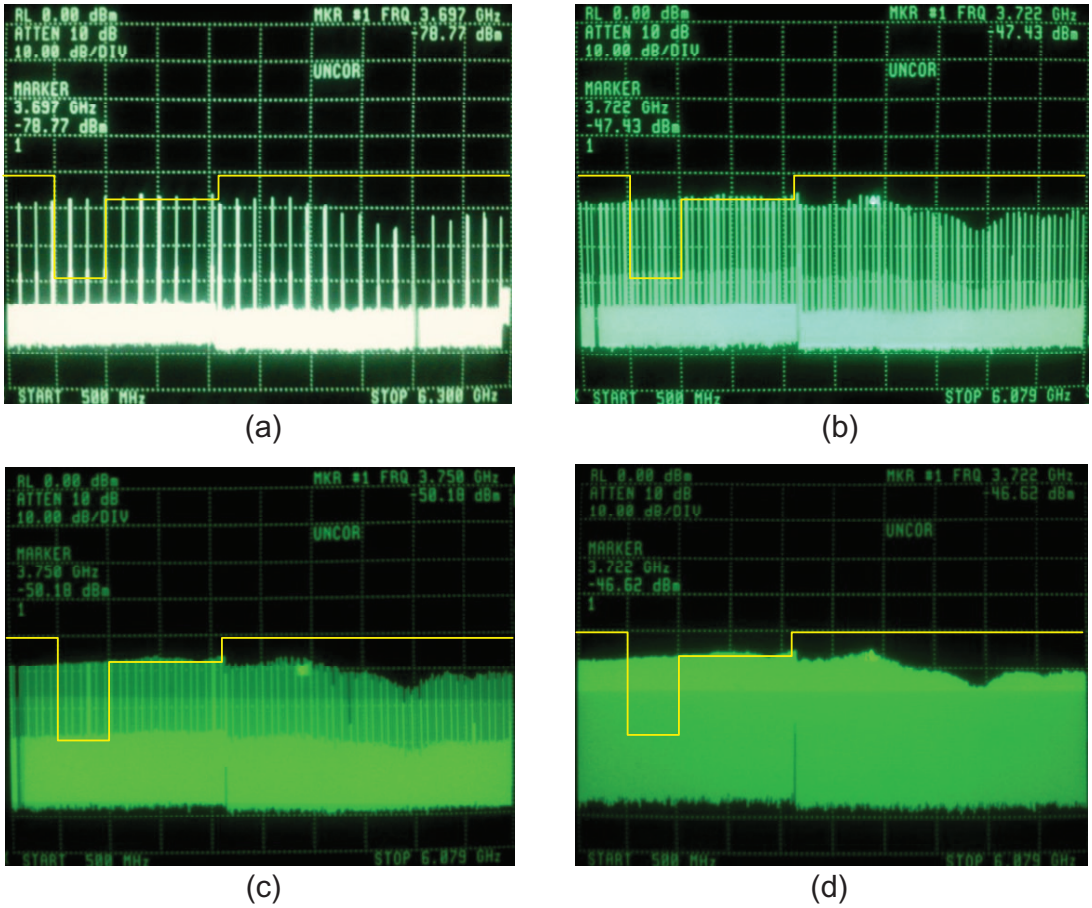

Figure 3.33: Power spectrum of the output Gaussian pulses at different pulse rates: (a) pulse rate at 10 KHz; (b) pulse rate at 30 KHz; (b) pulse rate at 10 MHz; (c) pulse rate at 100 MHz

Table 3.3: Overall IR-UWB transmitter configuration

Parameters	Values
Process	ST 90 nm CMOS
Frequency lower bound	1 GHz
Frequency upper bound	6 GHz
Number of sub-bands	1 lower UWB band
Pulse type	Gaussian
Pulse duration	Adjustable range 0.5-3 ns
Modulation scheme	On-Off Keying
Output pulse amplitude	Adjustable 30-560 mV
Transmitter power consumption	5.32 mW

Table 3.4: Performance comparison of the proposed Gaussian transmitter with previously published works

References	Pulse Type	Technology	Supply Voltage [V]	Pulse Amplitude [mV]	Pulse Width [ns]	Power Consumption [pJ/pulse]
[66] 2006	Gaussian	CMOS 0.18 μm	1.8 V	800	250 MHz	700
[75]	Gaussian	SiGe BiCMOS 0.18 μm	1.8 V	170	0.175	132
[76] 2007	Gaussian	CMOS 0.13 μm	1.8 V	350	0.7	30
[77] 2002	1st derivative Gaussian	Discrete	3 V	400	0.3	N/A
[78] 2006	2nd derivative Gaussian	CMOS 0.18 μm	1.8 V	30	1	21 mW (Tx)
This work	Gaussian	CMOS 90 nm	1.2 V	30-560	1	5.32 mW(Tx)

3.6 Summary

The first half of this chapter presents the design and implementation of an impulse range-gated UWB wireless transmitter in 90 nm CMOS for medical radar sensing and sensor communications. The transmitter uses the OOK modulation scheme to transmit the pulses. Amplitude of the transmitter output pulse can be adjusted within the range from 30 mV to 520 mV by a VGA for different levels of power emitting to fit a particular application. The fully integrated UWB transceiver occupies a core area of 50 μm by 100 μm. The average power consumption of the transmitter is 5.32 mW. The measured input data rate is 250 Mbps, and the transmitter generates a clock signal of 500 MHz internally. Measurement results confirm the workability of the transmitter. The energy-collection based receiver design is also presented, with simulation results. The implemented transmitter is well suited for the non-coherent IR-UWB receiver adopting an energy detection mechanism. In addition, this work demonstrates the design possibility of an extremely low power wireless sensor node with different power levels for radar sensing network.

In the second half of this chapter, an UWB transmitter generating tenth-order derivative of Gaussian pulse with Bi-phase modulation is proposed for real-time bio-medical sensing. The proposed IR-UWB radar transmitter requires no clock and consumes lower power. The transmitter prototype is designed and simulated in TSMC 90 nm CMOS with 1.0 V voltage supply. The baseband signal is generated at 100 Mbps to leave enough headroom for pulse generation. The positive and negative tenth derivative Gaussian pulses are generated. The pulse width is 0.6 ns. The transmitter output peak-to-peak amplitude is 130 mV. Simulating on a 1 V voltage supply, the transmitter draws an average of 9.037 mW when generating the tenth-order Gaussian derivative pulses at a pulse repetition frequency of 50 MHz. The transmitter output pulse has the energy of 3.1 pJ/pulse. The designs in this chapter are the compatible solutions for radar sensing applications with a low power, low complexity, and frequency-tunable capability (when changing the pulse combination). This design prototype can be modified to generate a full category of the different orders Gaussian derivative pulses and modulated multi-cycle sinusoidal pulses.

Chapter 4

Carrier-Based Ultra-Wideband Transmitter

This chapter presents the design, analysis, and implementation of an UWB carrier-based transmitter in 130 nm CMOS process and provides measurement results that demonstrate the radar concepts described in previous chapters. The previous chapter's impulse-based UWB transmitter leans more on the mixed-signal circuit techniques and analysis in time domain. Starting from this chapter, we will have more discussion on analog design techniques and extra attention will be paid to signal matching and signal integrity.

4.1 Introduction

Compared to the impulse-based technique, the carrier-based UWB system uses sinusoidal waves instead of short pulses to represent signals. These signals are easier to manage within the FCC spectrum and produce less distortion by the antennas. A few designs on carrier-based transmitters have been reported [85, 86, 87] but none of them utilizes the full designated UWB band. In this chapter, a power-efficient radar sensing transmitter design and implementation using a carrier-based UWB technique is proposed. This non-coherent UWB transmitter generates on/off modulated signals at different carrier frequencies within the full 3-10 GHz band. The frequency diversity technique allows the radar to detect the targets with more details since more waves at different frequencies are reflected from the dielectric boundaries.

The major motive behind this proposed transmitter is to demonstrate the feasibility of implementing a full band UWB radar transmitter with well-controlled frequency selectivity across its range of operation.

The pulse modulated sinusoidal signal is generated through multiplying a sinusoidal signal and an UWB pulse. The transmitter consists of a DCO, a pulse generator, a mixer, and an

output driver. This chapter will mainly focus on the full-band UWB digitally-controlled oscillator (DCO) design since it is the vital block of the transmitter. The first few sections from 4.2 to 4.5 discuss the proposed transmitter architecture and DCO design issues. Section 4.6 briefly discusses the timing blocks for pulse modulation and the mixer block. Section 4.7 and 4.8 demonstrates the radar transmitter implementation and measurement results.

4.2 Proposed Transmitter Architecture

Figure 4.1 shows the system architecture of the newly proposed UWB radar transceiver IC. This UWB transceiver integrates a diplexer with a full band UWB transmitter and a receiver circuit. The transmitter consists of a tunable UWB frequency oscillator, a mixer, a pulse generator, and a driver amplifier.

As discussed previously, the UWB signal is defined and restricted within the UWB band between 3.1 GHz to 10.6 GHz. To accurately control the signal frequency spectrum and create frequency diversity for the purpose of radar sensing, the 7.5 GHz UWB bandwidth is divided into several tunable sub-bands. A digital signal with a specific envelope shape is multiplied with a digitally controlled oscillator (DCO) output to generate a modulated sinusoidal signal. This sinusoidal carrier frequency can be tuned over the entire UWB frequency band by varying the capacitance value of a capacitor bank. For radar sensing applications, a low repetition rate is used to maintain a low average output power level. The transmitter employs a switching mechanism to reduce the power consumption and avoid the oscillation start-up transient delay and oscillation leakage.

In this proposed design, the outside control signal $V_{control}$ at the transmitter input is split into two paths. One goes into the UWB oscillator and controls the on/off switch of the oscillator, mixer, and the output driver. This means most of the transmitter blocks are turned off most of the time, and only turned on when $V_{control}$ is high. On the other path, passing through a time-delay inverter chain, delayed $V_{control}$ enters the pulse generator to trigger a voltage pulse with controllable pulse width. $V_{control}$ has a longer window time than V_{pulse}, and as a result, the oscillation starts a few nanoseconds before the pulse generator is triggered. An inverter chain is inserted into the second path to introduce a time delay before the pulse generator. After $V_{control}$ switches both the LC oscillator and the mixer on and the

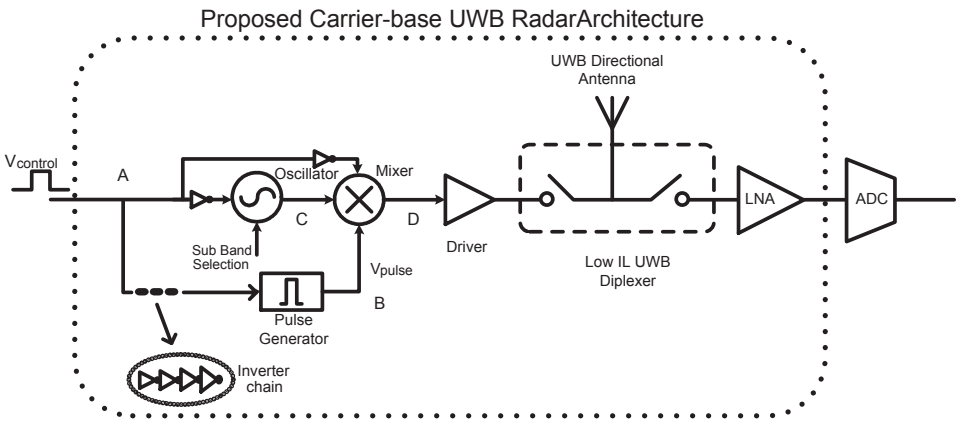

Figure 4.1: System architecture of the proposed UWB radar transceiver

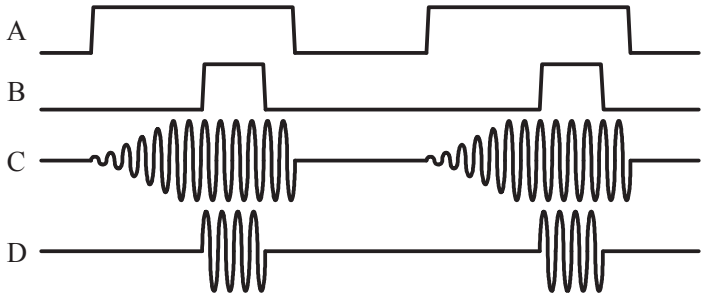

Figure 4.2: Signal flow in transmitter

oscillation reaches its steady state, the output of the pulse generator V_{pulse} with a narrower time window is then multiplied with the sinusoidal carrier to produce the transmitter output signal. The output driver amplifier is used to drive a 50 Ω output load.

The signal flow in the proposed transmitter is illustrated in Figure 4.2. The transmitter input signal $V_{control}$ at point A controls signals at C and B, and the signal at B generates the signal at D. The DCO generates the carrier signal with a different center frequency within the 3-10 GHz UWB band. The coarse tuning is achieved through selecting different capacitors by turning on and off the load capacitors in a capacitor bank. A three-capacitor combination divides the total 3-10GHz band into eight sub-bands. The fine frequency tuning is achieved through tuning the bias voltage of the varactor in the DCO.

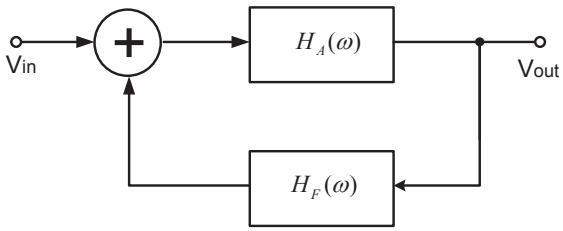

Figure 4.3: Mathematical model of the oscillator

4.3 Digitally Controlled Oscillator Design Considerations

In the carrier-based transmitter proposed, perhaps one of the most important and most challenging core functional blocks is the UWB DCO, which is designed to generate signals at frequencies ranging from 3 GHz to 10 GHz. This section will begin by reviewing some of the important oscillator design parameters and issues, followed by the DCO design approach in the next few sections.

The oscillator is a circuit block that transforms DC energy into a periodic alternating signal in time domain without external stimulus. The oscillator core is a positive-feedback closed loop under a particular oscillating frequency. Figure 4.3 shows the feedback model of an oscillator, where $H_A(\omega)$ is the forward transfer function and $H_F(\omega)$ is the feedback gain. The overall loop gain is thus equal to

$$H(\omega) = H_A(\omega)H_F(\omega) \tag{4.1}$$

According to Barkhausen fundamental criterion, a circuit has to meet the following two requirements for oscillation to start:

$$\begin{aligned} |H(j\omega_0)| &\geq 1 \\ \angle H(j\omega_0) &= 360^o \end{aligned} \tag{4.2}$$

To generate a working oscillating signal, the feedback system must have a frequency selection mechanism to fulfill the Equation (4.2) only at the designated frequency. This frequency selection mechanism is usually realized by two widely considered methods in integrated circuit

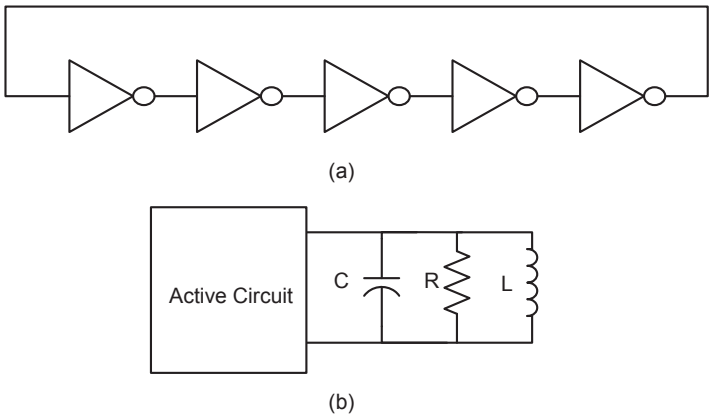

Figure 4.4: Different oscillator topologies: (a) Ring oscillator, (b) LC oscillator

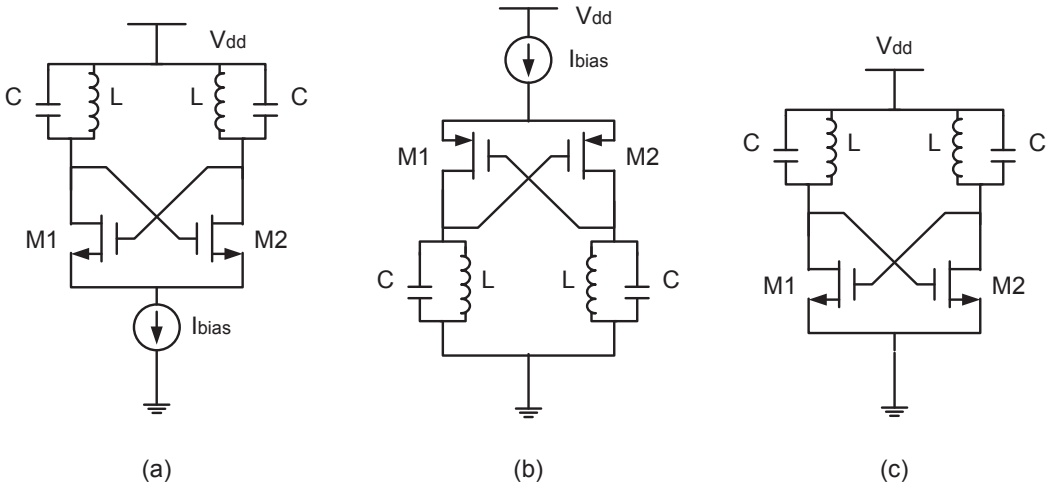

Figure 4.5: Different LC oscillators:(a) NMOS cross-coupled oscillator with current source at bottom, (b) PMOS cross-coupled oscillator with current source at top, (c) NMOS cross-coupled oscillator with no current source

design: waveform oscillator (or ring oscillator), as shown in Figure 4.4 (a), and resonant oscillator (LC oscillator), as shown in Figure 4.4 (b) [91, 94].

The ring oscillator can be realized through an all digital CMOS process without using any on-chip inductors, saving die area and cost. The ring oscillator consists of a few identical delay cells formulating a closed loop, with a loop gain satisfying Equation (4.2) at 1/T frequency, where T is the total delay time. The ring oscillator output swings between ground and power supply, resulting in a very noisy substrate owing to the charge injection.

The LC oscillator uses a LC bandpass filter as a frequency selective network at the feedback loop to attenuate all other frequencies and pass only the desired frequencies. The

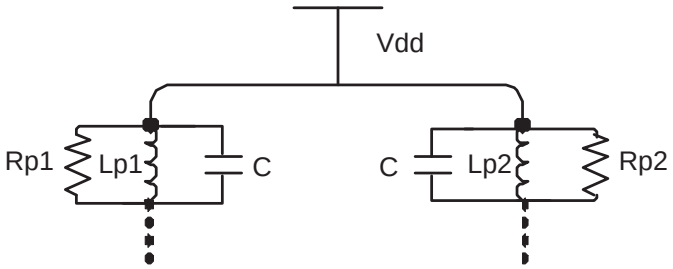

Figure 4.6: Equivalent LC load circuit

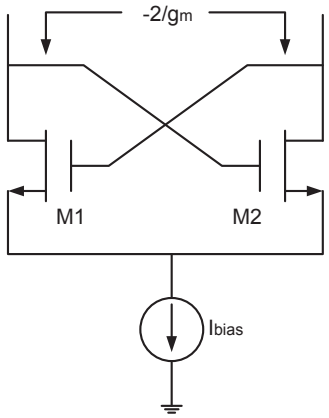

Figure 4.7: The equivalent resistance seen by the LC circuit

LC oscillator is a better choice since it can generate a signal at GHz range with low phase noise and much better jitter performance (even though in wideband radar applications, where phase noise is not the most important concern, an accurate frequency control is still desirable).

4.3.1 Integrated LC Oscillator Topology

There has been much recent research carried out to implement integrated LC oscillator using various techniques [65-70]. However, most of the integrated LC oscillators are originated from a few types of LC oscillator topology, as shown in Figure 4.5.

Figure 4.5 (a) adopts NMOS cross-coupled transistors to provide loop gain, with a current source at the source nodes of the NMOS pair. Figure 4.5 (b) adopts PMOS cross-coupled transistors as well, with a current source at the common-mode ground on the top of the configuration. The drain nodes of the transistor pairs are connected to the LC core. This PMOS configuration is more often applied in low frequency applications. Due to the slower mobility of the PMOS transistor compared to the NMOS transistor, the NMOS LC oscillator

configurations are more preferable to use in RF frequency applications.

The function of the tail current source in an oscillator is to provide controlled current to the cross-coupled NMOS pair and reduce loss. The oscillator in Figure 4.5 (c) is similar to the configuration in Figure 4.5 (a), but with the exclusion of the tail current source. In Figure 4.5 (c), the source node of M1 and M2 are directly connected to ground. The gate-drain voltage V_{gd} of M1 and M2 are equal to the amplitude of the oscillating voltage across the LC load. When the oscillator output voltage is zero, both M1 and M2 are in the saturation region. When the oscillating voltage is larger than the threshold voltage V_{th} of the transistor, the V_{gd} of either M1 or M2 will be larger than V_{th}, pushing the transistor into the linear region. At the same time, the other transistor V_{gd} will decrease, pushing the transistor further into the saturation region. The transistor working in linear region is equivalent to a resistor, consuming voltage headroom and extra power. This equivalent resistor is changing as the amplitude of the oscillating voltage changes, introducing extra loss. This gives a good reason to go back to the configuration in Figure 4.5 (a). By adding a tail current source I_{bias}, the current flowing through M1 and M2 are both equal to $I_{bias}/2$ when the oscillating amplitude is zero. With proper size of M1 and M2, the overdrive voltage V_{gs}-V_{th} is less than V_{th}. Thus, when the oscillating voltage is higher than the voltage that the transistor linear region can reach, either M1 or M2 will be pushed into the linear region, and the other into the cut-off region. The transistor in the linear region will have a current flow that is equal to a constant I_{bias}. The constant current will not add extra loss to the LC load.

For each oscillator configuration in Figure 4.5, the LC core can be redrawn as Figure 4.6. The resistor R_p is the equivalent parallel resistance of the inductor and capacitor on each LC tanks. To ensure an oscillation, the condition $R_p > -\frac{2}{g_m}$ must be satisfied, where g_m is the transconductance of the single transistor.

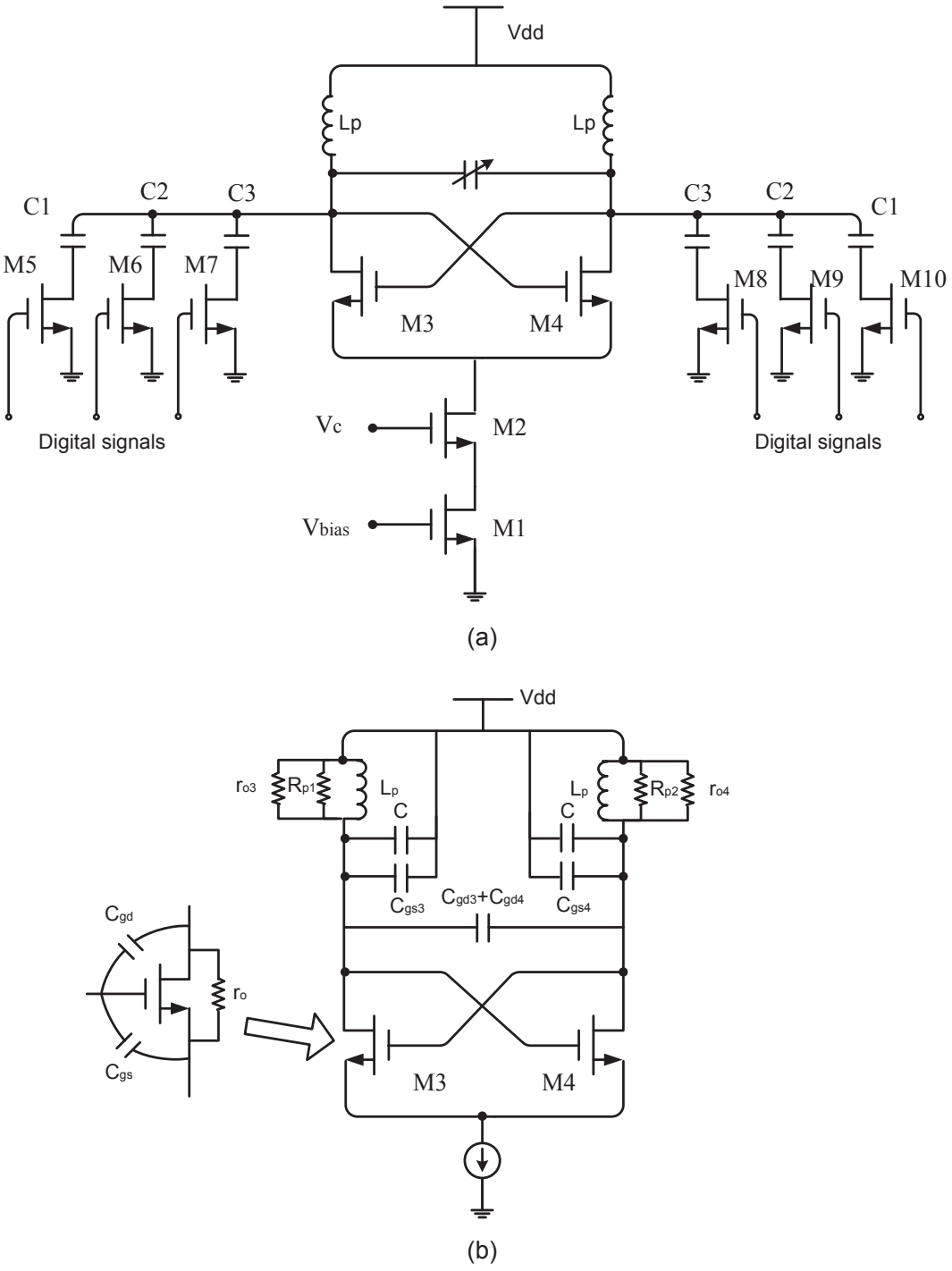

Figure 4.8: (a) UWB digitally controlled oscillator circuit, (b) The equivalent circuit model of the DCO core

The proposed DCO circuit is shown in Fig. 4.8 (a). The common source amplifier transistors M3 and M4 are cross-coupled in a positive feedback configuration with a total loop gain of H(jω) that is greater than unity and with 360^o phase shift. The common source pair LC load can be redrawn as shown in Fig. 4.8 (b). R_{p1} represents the equivalent parallel resistor of the parasitic resistance in L_{p1} and R_{p2} represents the equivalent parallel resistor for L_{p2}.

$$R_{p1,2} = R_S Q_L^2 = \frac{\omega_0^2 L_p^2}{R_S} \tag{4.3}$$

where Q_L is the quality factor of the inductor and R_s is the inductor parasitic series resistor. Large R_Ps are desirable for a stable oscillation. The quality factor of the load of the cross coupled pair M3 and M4 Q_{load} is

$$\frac{1}{Q_{load}} = \frac{1}{Q_L} + \frac{1}{Q_C} \tag{4.4}$$

where Q_c is the quality factor of on-chip capacitor and Q_C is much larger than Q_L. Thus $Q_{load} \approx Q_L$.

The gain of each common-source configured transistor is expressed as

$$A_{3,4} = g_{m3,4}(R_{p1,2} || r_{o3,4}). \tag{4.5}$$

where r_{o3} and r_{o4} are the transistor drain-source resistors. The overall closed loop gain is now expressed as

$$H(\omega) = A_3 \cdot A_4 = g_{m3} g_{m4} (R_{p1} || r_{o3})(R_{p2} || r_{o4}) \tag{4.6}$$

4.3.2 Cross Coupled Pair Parasitic

In the GHz frequency range, the parasitic capacitance of the device is no longer ignored owing to the fact that a small parasitic capacitance value will generate a large frequency shift at the DCO output. Thus, a more realistic model with transistor parasitic capacitance is shown

in Fig. 4.8 (b). For a single transistor, the gate-source and gate-drain capacitance are

$$\begin{aligned} C_{gs} &= \tfrac{2}{3} C_{ox} W L \\ C_{gd} &= C_{ov} W \end{aligned} \tag{4.7}$$

where C_{ox} is the gate oxide capacitance per unit area and C_{ov} is the overlap capacitance per unit width. The equivalent total parasitic capacitance $C_{parasitic}$ at each load is expressed as

$$C_{parasitic} = C_{gs3,4} + 4C_{gd3,4} = W(\frac{2}{3} C_{ox} L + C_{ov}) \tag{4.8}$$

where W and L are the width and length of the transistors.

Then, the DCO oscillation frequency can be expressed as

$$\omega_0 = \frac{1}{\sqrt{L_{P1,2}(C + C_{parasitic})}} \tag{4.9}$$

Combination of Equation (4.2) and (4.6) suggests that the minimum transconductance $g_{m3,4}$ of each NMOS transistor satisfies

$$g_{m3,4} > \frac{R_{S1,2}(C + C_{parasitic})}{L_{p1,2}} + \frac{1}{r_{o3,4}} \tag{4.10}$$

For a robust design to overcome the loss in on-chip inductors and parasitic capacitance in transistors and on-chip capacitors, a closed loop gain of 5 or larger is desired based on the simulation results.

4.3.3 Operational Regimes

At oscillation stage, the NMOS transistors are working in the non-linear switching mode. The DCO output waveform can be described by

$$V_{out} = \frac{4V_{sqr}}{\pi} \sum_{n=1}^{\infty} \frac{\sin(n\omega t)}{n} \tag{4.11}$$

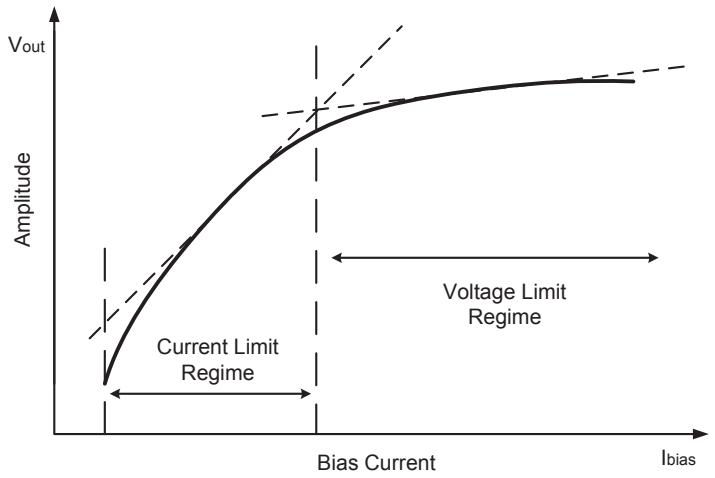

Figure 4.9: Oscillator operational regimes under different bias currents

where V_{sqr} is the switched square wave amplitude and n is an odd number. At resonant frequency ω_0, n=1, the voltage swing across the LC load is

$$V_{out} = \frac{4}{\pi} I_{bias} R_{P1,2} = \frac{4}{\pi} I_{bias} \omega_0 L_p Q \tag{4.12}$$

where I_{bias} is the bias current provided by transistor M1 in Fig. 4.8 (a).

The oscillating waveform amplitude is proportional to the bias current and quality factor of the load [104]. When the NMOS transistors are biased at a low current, the DCO output amplitude is limited by the overdrive voltage V_{or}=V_{gs}-V_{th} of each amplifying transistor. When the output voltage is greater than the overdrive voltage V_{or}, these two transistors M1 and M2 are working in the deep triode region (switch mode) and the bias current flows alternatively between M1 and M2. The LC load acts as a band pass filter to filter out the low and high frequency components to yield a pure sinusoidal signal at resonant frequency. The oscillator is now in the current-limited regime. In this regime, the swing voltage is directly proportional to the tail bias current.

Increasing the gate voltage of the current source transistor M1 will make M1 spend more time in the linear region in one oscillation cycle. However, the oscillating amplitude will not increase by increasing the gate voltage of M1. The oscillator now enters voltage-limited regime. The curve in Figure 4.9 shows the relationship between bias current and output oscillation amplitude. When the bias current is small, the increase of the output amplitude

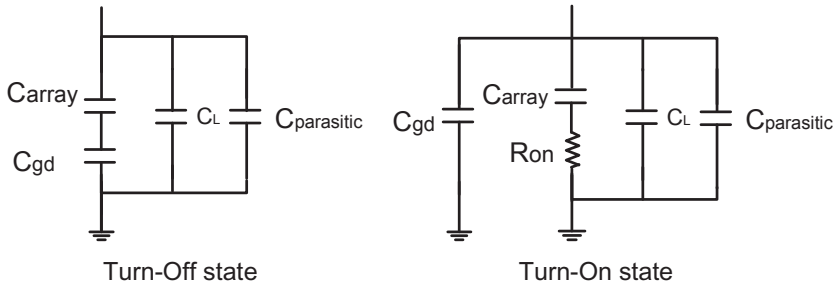

Figure 4.10: Capacitor array NMOS switch turn-off and turn-on model

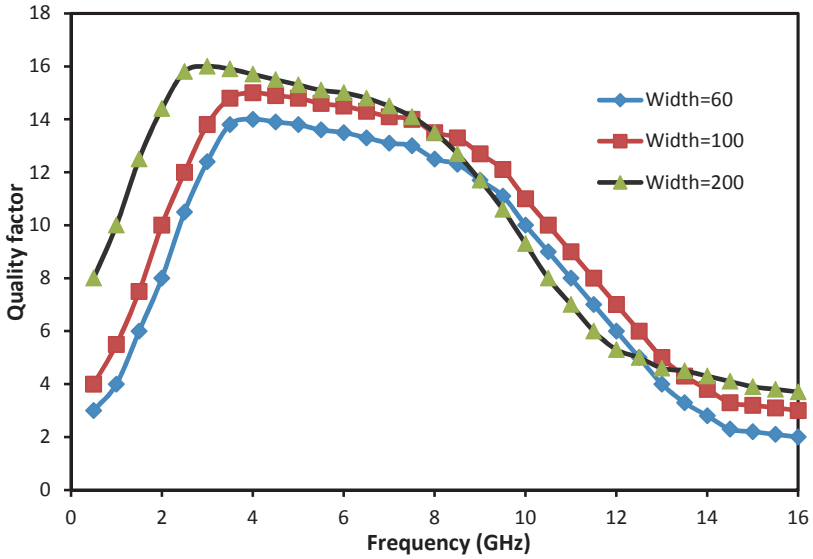

Figure 4.11: Quality factor of capacitor array resonators with different switch transistor width W=60 μm, W=100 μm, and W=200 μm

is in the linear region. As the bias current increases further, the slope of the amplitude change starts to decrease. The voltage at the source of the cross-coupled pair will approach V_{dd} and the oscillation amplitude will reach a maximum value, at a cost of high current consumption. For a low power design, it is desired to bias the oscillator in the current-limited regime.

4.4 Coarse Frequency Tuning

The frequency tuning range capability by a MOS varactor is limited to a few hundred MHz due to the low $C_{var-max}/C_{var-min}$ ratio. To meet the design requirement for UWB frequency bandwidth, a digitally controlled capacitor array topology is adopted along with the MOS varactor for UWB frequency tuning to further extend the frequency tunability of the oscilla-

tor. The coarse frequency tuning is achieved by band switching through NMOS transistors M5, M6, and M7 (M8, M9 and M10 are the replica of M5, M6, and M7, the left capacitor array shares the same control signals with the capacitor array on the right, as shown in Figure 4.8). The designed tunning range is from 3 GHz to 10 GHz. The capacitor array is binary weighted with C_3=$2C_2$=$4C_1$. A three-bit digital signal control eight array combinations which results in eight frequencies spanning a 7GHz bandwidth.

In the previous section, only the parasitic capacitance of the cross-coupled transistors has been discussed. However, when the capacitor arrays are turned-on, the parasitic capacitance of the switches is inevitably large. A simplified NMOS switch is modeled for turn-off and turn-on state, as shown in Fig. 4.10. The total capacitance, C_{Tot}, when all the capacitor array switches are turned off is

$$C_{Total\_array\_\min} = C_L + C_{parasitic} + \frac{1}{\frac{1}{C_1}+\frac{1}{C_{gd1}}} + \frac{1}{\frac{1}{C_2}+\frac{1}{C_{gd2}}} + \frac{1}{\frac{1}{C_3}+\frac{1}{C_{gd3}}} \tag{4.13}$$

And the total capacitance C_{Tot} when all the switches are turned on is

$$C_{Total\_\max} = C_L + C_{par} + C_1 + C_2 + C_3 + C_{gd1} + C_{gd2} + C_{gd3} \tag{4.14}$$

The parasitic capacitance and the drain-source resistance of each NMOS switch of the capacitor array deteriorate overall quality factor Q_{load} at each resonance frequency. This variation in Q_{load} reduce the oscillating waveform amplitude at lower frequencies.

The switch NMOS transistors have turn-on resistance of R_{on}:

$$R_{on} = \frac{1}{\mu_n C_{ox} \frac{W}{L}(V_{GS} - V_{TH})} \tag{4.15}$$

Under current standard CMOS technology, the lossy on-chip spiral inductor has lower Q (for CMOS 130 nm on-chip inductor, Q is approximately 10) and higher loss. Fig. 4.11 shows the plot of LC resonator quality factor curves at different capacitor array switch transistor widths. In this design, the width of the capacitor array switch transistor is 150 μm. The size of the cross-coupled pair transistor is W=100 μm and L=130 nm while bias current is set at 3 mA. Small L is chosen to have a high cut-off frequency and to reduce the parasitic capacitance.

4.5 Oscillation Start-Up Transient

The DCO is turned on/off and switched between different frequencies repeatedly depending on the digital control input. Therefore, a fast start-up time and switching time are important to reduce the oscillation leakage at the start-up and switching transient time. The trade-off between the setting time and other design constraints are discussed in this section.

An equivalent circuit model of the oscillator core is shown in Figure 4.12. The oscillation start-up transient stage is analyzed under the small-signal model. The small-signal model becomes unprecise in the oscillator saturation region. Using KCL nodal approach (i.e, I_{gm}=I_c+I_L+I_R), a differential equation is obtained

$$C\ddot{v}(t) + \frac{1}{R_p}\dot{v}(t) + \frac{1}{L}v(t) = g_m\dot{v}(t) \tag{4.16}$$

and rearranged to be

$$C\ddot{v}(t) + (\frac{1 - g_m R_p}{R_p})\dot{v}(t) + \frac{1}{L}v(t) = 0 \tag{4.17}$$

The characteristic equation is

$$Cs^2 + \frac{(1 - g_m R_p)}{R_p}s + \frac{1}{L} = 0 \tag{4.18}$$

since the under-damped condition yields

$$(1 - g_m R_P)/2R_P C < \omega_0 \tag{4.19}$$

Therefore, the roots of the characteristic equation are complex numbers and solved to be

$$s = \frac{g_m R_p - 1}{2R_P C} \pm j\sqrt{\frac{1}{LC} - \left(\frac{g_m R_P - 1}{2R_P C}\right)^2} \tag{4.20}$$

Thus, the analytical solution to this differential equation, which is the exponential envelope

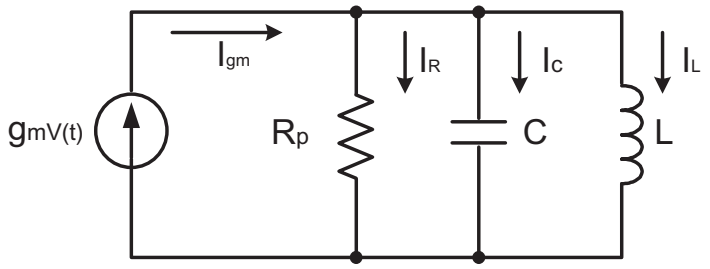

Figure 4.12: Equivalent circuit model of oscillator core for KCL analysis

function of the oscillating waveform, can be expressed as

$$\begin{aligned} v(t) &= A_1 \cdot e^{\frac{g_m R_p - 1}{2R_P C} \cdot t} \\ &= A_1 \cdot e^{\frac{\omega_0 (g_m R_P - 1)}{2Q} \cdot t} \end{aligned} \tag{4.21}$$

where A_1 is the initial voltage amplitude, and the parallel Q equals to $\omega_0 C R_P$. The imaginary part is excluded for simplicity. The exponential growth rate increases faster as exponential constant ($g_m R_P$ - 1)ω_0/2Q increases. A large transistor gain $g_m R_P$ gives a faster oscillation rise time. A large Q favors a better phase noise performance, but reduces the signal rise time. Compromise has to be made between these two design constraints. Figure 4.13 demonstrates the oscillation start-up response for different transistor g_m. Equation (4.21) also shows that the rise time of the oscillation depends on the resonance frequencies of the LC tank: higher resonance frequencies correspond to a faster rise time.

Equation (4.2) and (4.21) suggest that the gain of the NMOS transistor must be larger than unity to start an oscillation, as previously discussed. Since the oscillation after start-up is a highly non-linear process, the oscillator loop gain is reduced to unity to retain a stabilized oscillation at oscillation stage.

Figure 4.14 shows the oscillation signals switching between different frequencies from 3.2 GHz to 9.8 GHz in UWB band. The switching time is less than one nanosecond. When the oscillating frequency decreases, the DCO load increases and the DCO load Q decreases. As a result of DCO load variation at different frequencies switching, the output amplitude is decreasing with frequency.

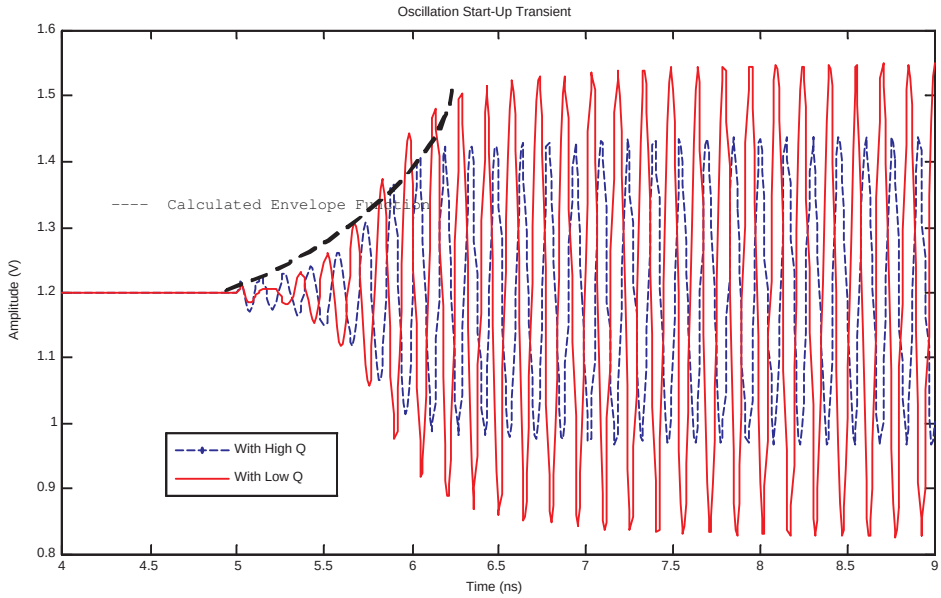

Figure 4.13: Simulated start-up transient with different LC load Q values

4.6 Pulse Generator and Mixer

Figure 4.15 shows the pulse generator. Some detailed discussion of pulse generator implementation has been presented in Chapter 3. The input signal V_data, which is also named Tx_EN in Figure 4.16, passes through an inverter chain to improve the rising and falling edges of each input signal. The input signal V_data is split into two signal paths and both are fed into an AND gate. Signals in one path are delayed by six inverters. The AND gate only outputs high when both inputs are high, and the time for both inputs be high is the delay time set by the inverter chain in the delay path. The output pulse width is determined by this delay time. The output pulse width can be adjusted by changing the delay of the inverter chain [95, 67]. This is achieved by adjusting the load capacitance.

Figure 4.16 (a) shows the circuit for the pulse generator, mixer and output driver. The Tx_trigger signal is the delayed Tx_EN signal. This delay allows the DCO, mixer, and driver to start-up before the pulse generator is turned on. The delay unit employs a current-starving technique to control the pulse width through the Delay_ctrl signal. The pulse slope is controlled using capacitors at each delay stage. By changing the capacitor load, the pulse generator can generate a Gaussian-shaped or rectangular-shaped pulse envelop.

A differential pair with a controlled current source using the pulse envelope is employed

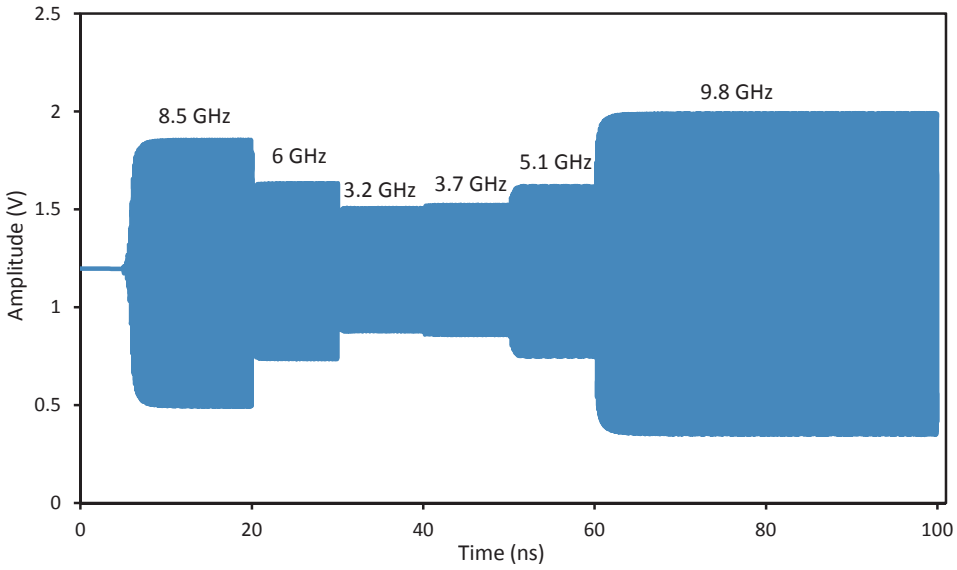

Figure 4.14: Output signal switching between different frequencies

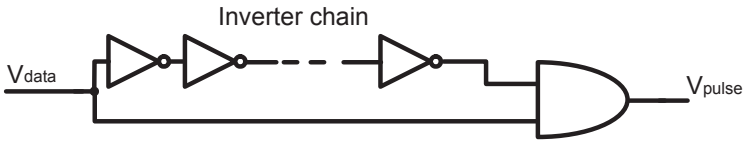

Figure 4.15: Single pulse generator unit

as a single balanced voltage mixer, as shown in Figure 4.16 (a). Transistor M6 and M7 form the differential pair and transistor M5 is the tail current source. The pulse envelope voltage controls the gain of the differential pair as a function of time by controlling the gate-source voltage of M5 and the bias current I_5. The differential pair output voltage and output current can be expressed as

$$V_{out} = V_{out}^{+} - V_{out}^{-} \tag{4.22}$$

$$I_{out} = I_6 - I_7 \tag{4.23}$$

The pulse envelope, which is either a rectangular function or a Gaussian function, can be represented by the signum function sgn[pulse(ω_{pulse},t_{pulse})] in Equation 4.24, where ω_{pulse} and

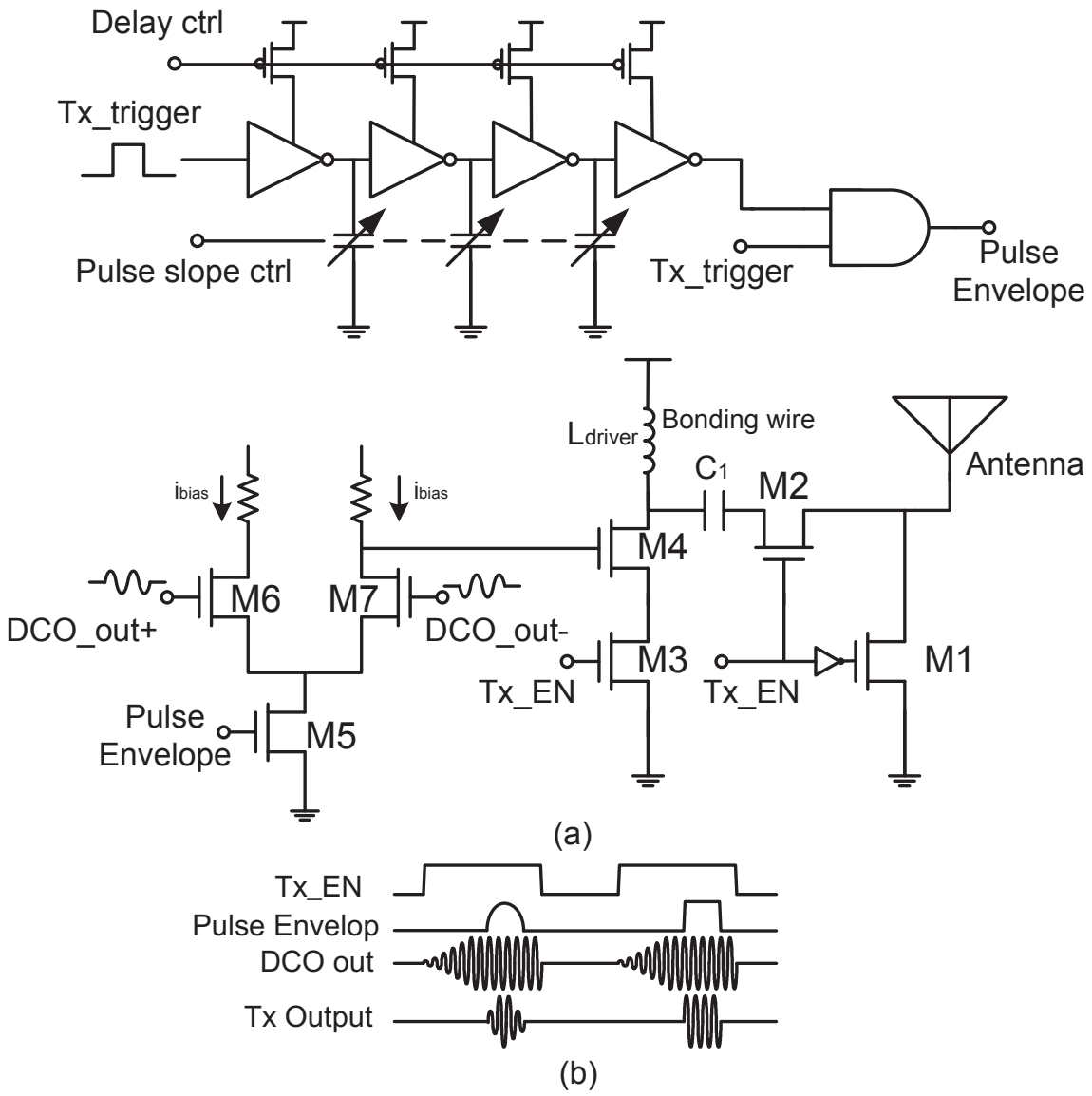

Figure 4.16: Modulated pulse generation

t_{pulse} are the pulse repetition rate and pulse width, respectively.

$$\text{sgn}[pulse(\omega_{pulse}, t_{pulse})] = \begin{cases} -1 & if \quad pulse(\omega_{pulse}, t_{pulse}) < 0 \\ 0 & if \quad pulse(\omega_{pulse}, t_{pulse}) = 0 \\ pulse(\omega_{pulse}, t_{pulse}) \approx 1 & if \quad pulse(\omega_{pulse}, t_{pulse}) > 0 \end{cases} \tag{4.24}$$

The transconductance of the differential pair is

$$g_m = \sqrt{2\mu_n C_{ox} \frac{W}{L} (1/2) I_5} \tag{4.25}$$

The bias current I_5 is a function of the gate-source voltage of M5. Therefore, it can be expressed as the function of the pulse envelope as

$$I_5 = \{\text{sgn}pulse(\omega_{pulse}t_{pulse})\}I_{ss} \tag{4.26}$$

where I_{ss} is the peak bias current. The Fourier series representation of sgn[pulse(ω_{pulse},t_{pulse})] can be expanded into the form:

$$\text{sgn}[pulse(\omega_{pulse}t_{pulse}) = \sum_{k=1}^{\infty} A_k \cos\omega_{pulse}t \tag{4.27}$$

where A_k is the coefficients of the Fourier series and is expressed as

$$A_k = \frac{\sin(k\pi/2)}{k\pi/4} \tag{4.28}$$

The gain of the mixer G_{mixer} is expressed based on the differential pair gain:

$$\begin{aligned} G_{mixer} &= g_m \cdot R_{load} \\ &= \sqrt{2\mu_n C_{ox}\frac{W}{L}(\sum_{k=1}^{\infty} A_k \cos\omega_{pulse}t)(1/2)I_{ss}} \cdot R_{load} \end{aligned} \tag{4.29}$$

An inductive peaking common-source amplifier driver drives the pulse-modulated signal to the output antenna. The driver inductive peaking inductor L_{driver} is realized using bonding wire. C1 is the pulse-shaping capacitor. M1 and M2, controlled by Tx_EN, are the shunt-series connected diplexer switches. High impedance resistors are connected at the gates of M1 and M2 to provide better isolation. To minimize the turn-on resistance of the switches, a large transistor size is chosen for M1 and M2.

Figure 4.16 (b) shows the signal flow at each circuit block. The gating signal Tx_EN turns on the transmitter, and the pulse envelop is generated by the pulse generator. Tx_Output shows different pulse-modulated UWB signals.

4.7 Implementation of the Carrier-base Transmitter

The UWB radar carrier-based transmitter is implemented in a 130 nm seven-metal CMOS process. The on-chip capacitor array are implemented using a metal-insulator-metal structure. The spiral inductors were implemented on the top metal with a shield ground plane.

The schematic of the UWB oscillator is shown in Figure 4.8. Table 4.1 shows the component values for the transmitter DCO core. Even though the size of cross-coupled NMOS does not affect the noise of the oscillator, the oscillator noise is affected by the size of the tail current source transistor. The oscillator noise is inversely proportional to the product of the transconductance g_{mbias} of M1 and the LC equivalent resistance R_p. Once the LC resonance core is determined, R_p is a fixed parameter. Therefore, a small g_{mbias} is desired for current source M1. For M1, a large W/L ratio will reduce the oscillator noise and minimize the override voltage to leave more voltage headroom for output. The width of the current source transistor M1 is chosen to be 100 μm and the width of the oscillator switch M2 are chosen to be 100 μm as well. The size of M1 and M2 is limited by the parasitic capacitance M1 and M2 contributing to the source node of the cross-coupled pair. If M1 and M2 are too large, the parasitic capacitance will provide a high frequency pass from source node to ground. The current flowing through M3 and M4 are no longer a constant when the cross-coupled pair is working in linear region, degrading LC load quality factor and inducing extra loss.

The width of M3 and M4 are 100 μm. The bias current I_{bias} is providing 9 mA current. The transconductance $g_{m3,4}$ of the cross-coupled pair NMOS M3 and M4 is approximately 14 ms, 1/gm is 71.42. The minimum transistor length L=130 nm is chosen to have a high cut-off frequency and reduce the parasitic capacitance. The width of capacitor array switch transistors are 160 μm. The transmitter output driver NMOS transistor width is 200 μm.

4.8 Measurement Results

The proposed transceiver (transmitter and receiver) circuit was fabricated using the IBM 130 nm standard CMOS technology, packaged in high frequency cavity and test fixture for testing and prototyping. The overall die area including analog I/O pads is 2 mm^2.

Both the fabricated transmitter and the receiver were measured using test equipments. In

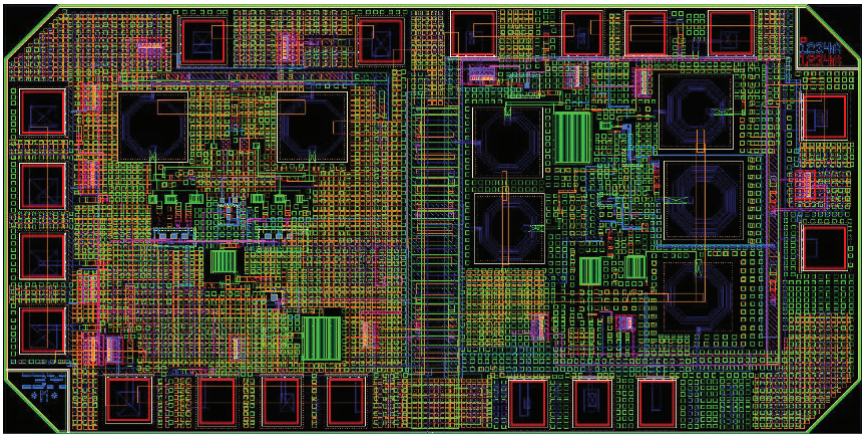

Figure 4.17: Transmitter and receiver layout (receiver will be discussed in chapter 5)

Table 4.1: DCO LC network components

Components	Values with physical dimensions
L_{p1}	581 pH 140 μm
L_{p2}	581 pH 140 μm
C_p1	80.36 fF 5.33 μm / 7 μm
C_p2	80.36 fF 5.33 μm / 7 μm
C_1	279.95 fF 14.26 μm / 10 μm
C_2	569.96 fF 14.37 μm / 19 μm
C_3	679.94 fF 16.79 μm / 20 μm
C_4	279.95 fF 14.26 μm / 10 μm
C_5	569.96 fF 14.37 μm / 19 μm
C_6	679.94 fF 16.79 μm / 20μm

this chapter, only transmitter measurement results are discussed, and the receiver is covered in Chapter 5. The power supply voltage is 1.2 V. For measurement purpose, additional analog I/O pads are designed at the output of the transmitter and input/output of the receiver front-end.

The measurement setup is shown in Figure 4.20. The Agilent 81110A Pulse Pattern Generator was used to generate a control signal for the transmitter. The HP spectrum analyzer and Agilent 16000 series scope were used to measure DCO output spectrum and transmitter pulse-modulated output waveform in time domain.

The frequency spectrum of different tuned frequencies at the transmitter output are shown in Fig. 4.22. The tuning range is from 3.2 GHz to 10 GHz. The internal attenuation of the

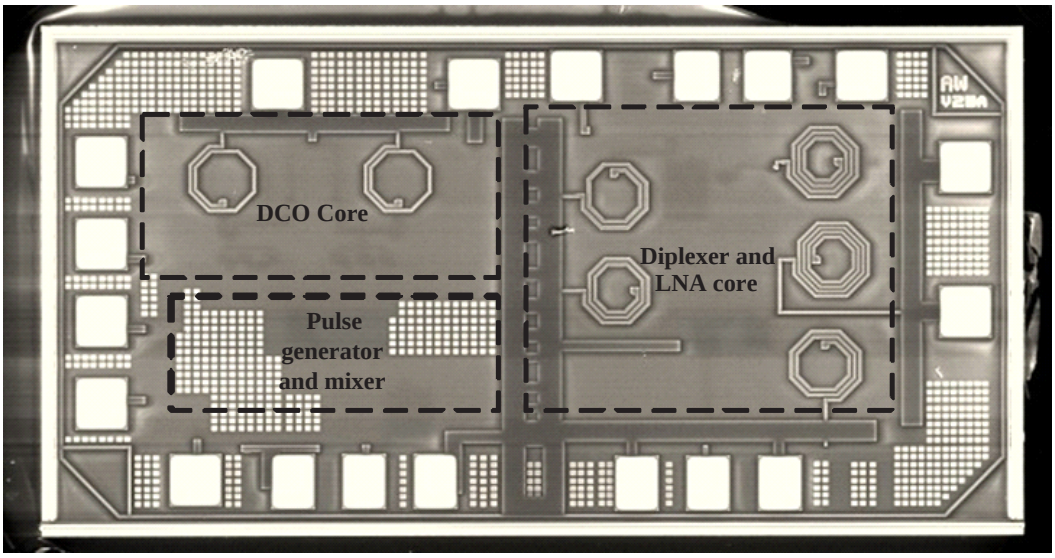

Figure 4.18: Micrograph of the transceiver die

spectrum analyzer was set to 10 dB. The output peak power at 8.312 GHz is -1.97 dBm. The average power of the output is duty cycle dependent. Fig. 4.21 shows the measured UWB signal under the modulated-pulse mode at the receiver side. The carrier frequency of the waveform in Fig. 4.21 is 3.6 GHz. The peak-to-peak amplitude of 300 mV was observed. The pulse duration is set to 3 ns.

Table 4.2 summarizes the performance of the proposed transmitter DCO, with comparison to previously published UWB VCOs. Compared to other works, this design achieved the widest frequency tuning range with a small chip area. The transmitter average power could reach an extremely low level owing to the low duty cycle.

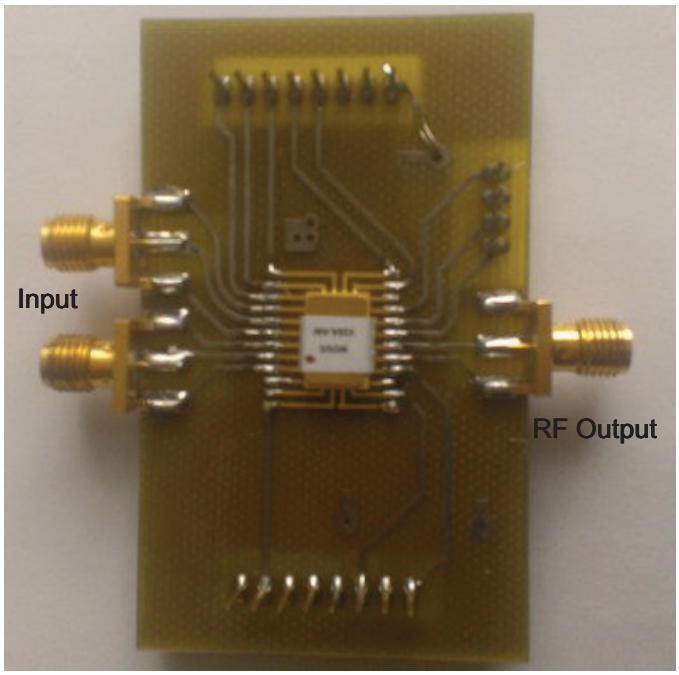

Figure 4.19: Transmitter test PCB

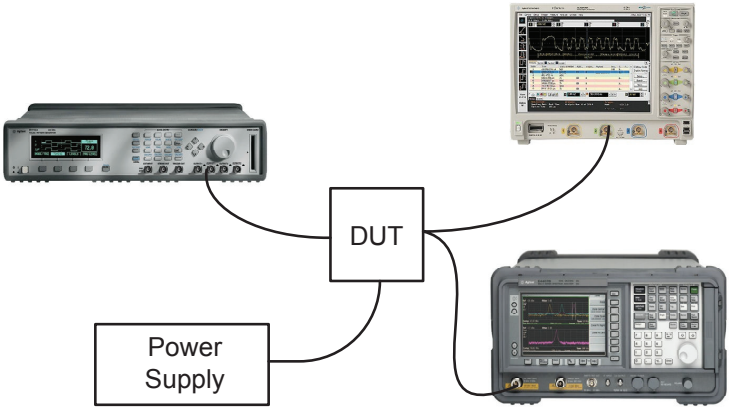

Figure 4.20: Transmitter measurement setup

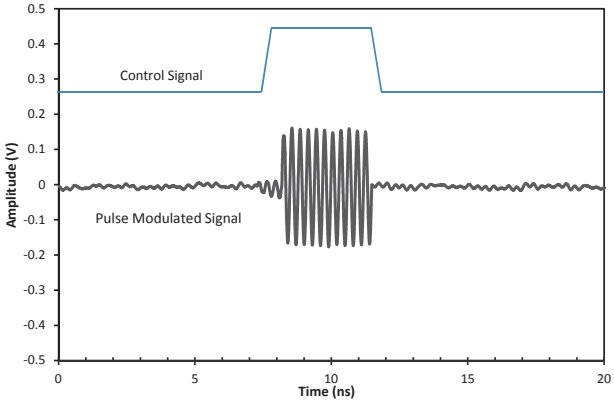

Figure 4.21: Measured pulse-modulated signal at 3.7 GHz in time domain

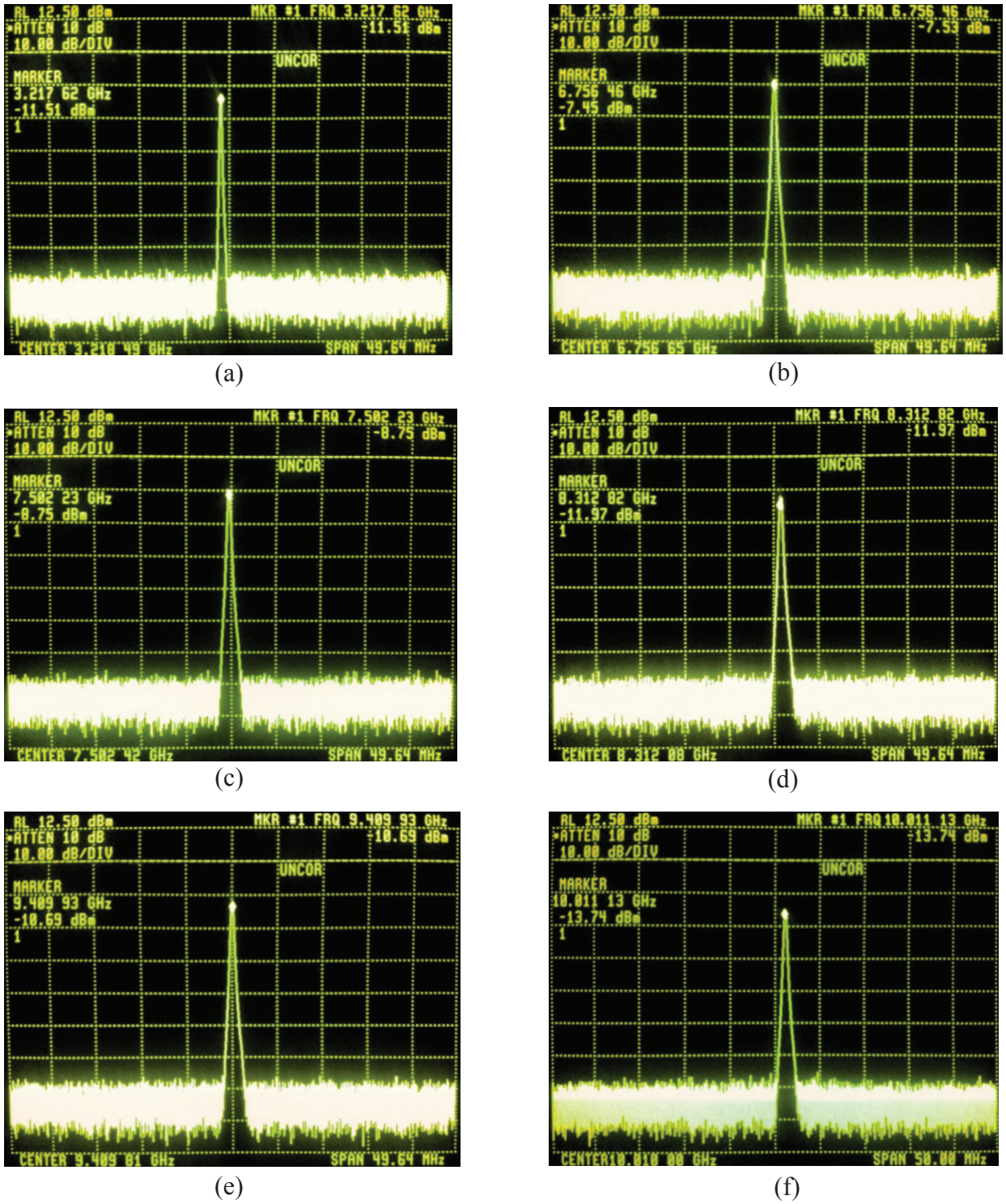

Figure 4.22: Measured carrier frequency spectrum tuning of transmitter output at (a)3.22 GHz, (b) 6.76 GHz, (c) 7.50 GHz, (d) 8.31 GHz, (e) 9.49 GHz, (f) 10.03 GHz

Table 4.2: Summary of UWB transmitter core DCO performance and comparison with previously published wideband voltage oscillators

Designs	Technology	Tuning Range (GHz)	Tuning Range (%)	BW [GHz]	Power (mW)	Core Area (mm^2)
This Design	130 nm CMOS	3.2 - 10	105	6.9	7 (average power)	0.3
[91]	130 nm CMOS	3.4-7	69	3.6	1-8	0.65
[92]	180 nm CMOS	0.5-3	143	2.5	6-28	0.045(active inductor)
[93]	130 nm CMOS	3.1-5.2	50	2.1	2.5-8.5	N/A
[94]	130 nm CMOS	1.3-6	128	5.7	4.3-9.1	0.295

4.9 Summary

This chapter proposes a fully integrated UWB carrier-based radar transmitter in standard 130 nm CMOS process. The design approach and implementation of each circuit block is presented in different sections of this chapter. The DCO design issues and design approach were discussed. A binary-weighted capacitor array NMOS LC oscillator topology was adopted for the transmitter core design. The pulse generator and mixer circuits were briefly discussed as well. The transmitter implementation was presented and discussed, followed by the measurements results of the transmitter.

The frequency spectrum of different tuned frequencies at the transmitter output are shown in Fig. 4.22. The tuning range is from 3.2 GHz to 10 GHz. The internal attenuation of the spectrum analyzer was set to 10 dB. The output peak power at 8.312 GHz is -1.97 dBm. The pulse-modulated waveform at 3.6 GHz is observed. The peak-to-peak transmitter output amplitude is 300 mV. The pulse duration is 3 ns. The transmitter consumes less than 0.1 mA of static current and the average power consumption of the transmitter is 9 mW.

The transmitter measurement results demonstrates the feasibility of implementing a full band UWB radar transmitter with well-controlled frequency diversity across its range of

operation. The good phase noise performance, high integration, and low area of the proposed UWB carrier-based transmitter makes it a very attractive SoC solution for a low-power UWB transceiver.

Chapter 5

Ultra-Wideband Receiver Front-end

The previous chapters largely focus on the UWB impulse and carrier-based transmitter front-end design. However, the more challenging part falls on the UWB radar receiver front-end. In an UWB radar receiver, the UWB LNA is the most critical block since it dominates the performance of the receiver sensitivity and selectivity. This chapter begins with a discussion about the important receiver performance measurements in Sections 5.1 and 5.2, and UWB receiver front-end circuit topology in Section 5.3. The later sections of this chapter covers the receiver front-end design, analysis, implementation, and measurement results.

5.1 Receiver Sensitivity

Receiver sensitivity is the most important figure of merit in the UWB radar receiver performance. It is defined as the minimum detectable signal at the receiver front-end, given that there is large enough signal-to-noise ratio (SNR) at the receiver front-end output. The maximum distance of signal transmission and detection is determined by this parameter. The receiver sensitivity is largely dominated by the internal noise generated inside the building blocks of the receiver front-end.

5.1.1 Receiver Noise Figure

The nature of noise generation is a random process, caused by the current flowing through the device. It can be only represented in term of statistical expressions. The most common noise associated with each receiver building blocks are thermal noise and flicker noise (1/f noise). The average thermal noise power P_{av} in a frequency band of interest can be expressed

as

$$P_{av} = kT\Delta f \tag{5.1}$$

where k is the Boltzmann constant ($\approx 1.38\times10^{-23}$), T is the absolute temperature, and Δf is the bandwidth. Thermal noise is independent of the operating frequency, therefore is the most widely considered noise type. The flicker noise (or 1/f noise) is inversely proportional to the operating frequency. For applications in UWB frequencies, the flicker noise is no longer a significant source of noise.

Noise factor is used to measure the noise performance of a receiver system. The noise factor of a system is defined as

$$F = \frac{P_{out\_total}}{P_{out\_source}} = \frac{P_{out\_source} + P_{\text{internal}}}{P_{out\_source}} = \frac{SNR_{in}}{SNR_{out}} \tag{5.2}$$

where P_{out_total} is the total output noise power from the receiver system, P_{out_source} is the noise power introduced from signal source, $P_{internal}$ is the noise power induced by the system itself, SNR_{in} is the receiver system input SNR, and SNR_{out} is the system output SNR. Noise figure (NF) is defined as 10logF.

In a receiver system consisting of cascaded blocks, the system overall noise factor is expressed as

$$F = F_1 + \frac{F_2 - 1}{G_1} + \frac{F_3 - 1}{G_2 G_1} + \cdots \tag{5.3}$$

where F_i is the noise factor for each individual block and G_i is the forward gain for each individual block. Equation (5.3) clearly indicates that the overall system noise is dominated by F_1 and G_1, the noise factor and the gain of the first block. Therefore, for a high sensitivity UWB receiver, a receiver front-end LNA with low noise and good gain is desired.

5.1.2 MOS Noise Model

Same as the signal, noise is also a function of time, but with an average of zero amplitude over a prolonged period. However, the average power of noise is a positive number, and noise

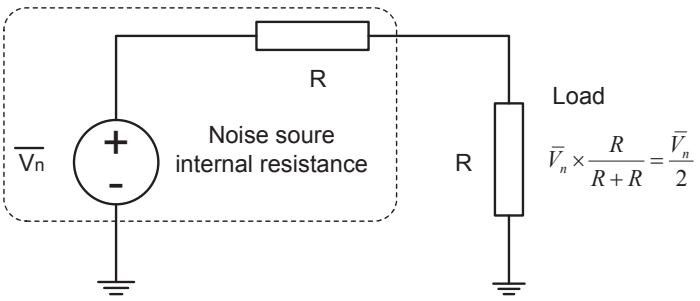

Figure 5.1: Thermal noise definition and representation

does contains energy.

The MOS transistor, in another point of view, can be seen as a variable small-signal resistor, in both linear and saturation regions. Thus, the major noise source of the MOS transistor considered here is the thermal noise, induced from the channel resistor of the transistor.

Equation (5.1) shows the noise power in a defined frequency band. The thermal noise is represented in Figure 5.1. $\overline{V_n}$ represents the thermal noise source and the load has the same resistance value as the internal resistance of the noise source. The power on the load R is the maximum available noise power that can be measured. The noise potential on the load is

$$\overline{V}_n \times \frac{R}{R+R} = \frac{\overline{V}_n}{2} \tag{5.4}$$

The available thermal noise power is

$$P_{av} = \frac{V_R^2}{R} = \left(\frac{\overline{V}_n}{2}\right)^2 \cdot \frac{1}{R} = \frac{\overline{V}_n^2}{4R} \tag{5.5}$$

Combining Equation (5.1) and Equation (5.5) yields a thermal noise expression in voltage:

$$\overline{V_n^2} = 4kTR\Delta f \tag{5.6}$$

and in current:

$$\overline{i_n^2} = 4kT(\frac{1}{R})\Delta f \tag{5.7}$$

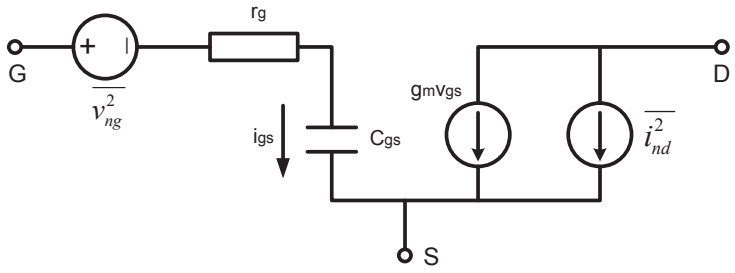

Figure 5.2: A single MOS small signal noise equivalent circuit

The MOS small signal noise equivalent circuit is shown in Figure 5.2. In the noise equivalent circuit, only small signal channel resistance exists between the transistor drain node and source node. In UWB frequency, the noise caused by the small signal channel resistance is coupled to the gate, which is represented by $\overline{v_{ng}^2}$. Derived from Equation (5.7), the drain-source noise is represented as

$$\overline{i_{nd}^2} = 4kT\gamma g_{d0}\Delta f \tag{5.8}$$

where g_{d0} is the transconductance of the MOS when V_{ds} is equal to zero. Thus, at linear region, γ is equal to 1. As the MOS enters into the saturation region, γ decreases. The coupled gate noise is expressed as

$$\overline{v_{ng}^2} = 4kT\delta r_g\Delta f \tag{5.9}$$

where the equivalent gate resistor r_g is

$$r_g = \frac{1}{5g_{d0}} \tag{5.10}$$

and δ is the gate noise coefficient, usually equal to 2γ [103].

5.2 Receiver Linearity

Similar with the narrow band system, receiver linearity is also an important figure of merit of the UWB receiver performance since it describes the degree of signal distortion caused by the receiver non-linearity, as well as the maximum signal the receiver can receive.

Most of the RF circuit system can be described using the following transfer function:

$$signal(V_{DC} + v) = k_0 + k_1 v + k_2 v^2 + k_3 v^3 \tag{5.11}$$

where k_0, k_1, k_2, and k_3 are the coefficients of DC signal, gain, second order nonlinearity, and third order nonlinearity, respectively. If an input signal is v=Acosωt, substitute this into Equation (5.11), the system output signal can be expressed as

$$\begin{aligned} &signal(V_{DC} + v) = k_0 + k_1 A\cos\omega t + k_2 A^2 \cos^2 \omega t + k_3 A^3 \cos^3 \omega t \\ &= (k_0 + 0.5k_2 A^2) + (k_1 A + 0.75k_3 A^3)\cos\omega t + 0.5k_2 A^2 \cos 2\omega t + 0.25k_3 A^3 \cos 3\omega t \end{aligned} \tag{5.12}$$

Equation (5.12) shows that the baseband signal is interfered by the third order non-linearity k_3. k_3 is usually a negative number [103], therefore, after the nonlinear system, the amplitude of baseband signal is reduced by a factor of $0.75k_3A^3$. The 1dB compression point is the performance measure of how much the baseband signal is suppressed by the third order nonlinearity. It is defined as the point where the output gain drops 1dB lower than the ideal linear gain, and is derived as

$$A_{1dB} = \sqrt{0.145 \left| \frac{k_1}{k_3} \right|} \tag{5.13}$$

The intermodulation signal is another issue caused by the system nonlinearity. The second and third order terms, after polynomial expansion, contain baseband signal components. And this could as well degrade the quality of the baseband signal. In the UWB receiver system, the useful bandwidth covers several GHz of frequency. For an UWB signal, a continuous spectrum is observed over a few GHz, thus it is hard to observe the intermodulation for such a signal. In this case, it is more meaningful to discuss the signal distortion caused by nonlinearity in time domain, in terms of group delay. But for a carrier-based UWB signal, the conventional measures of nonlinearity still comply.

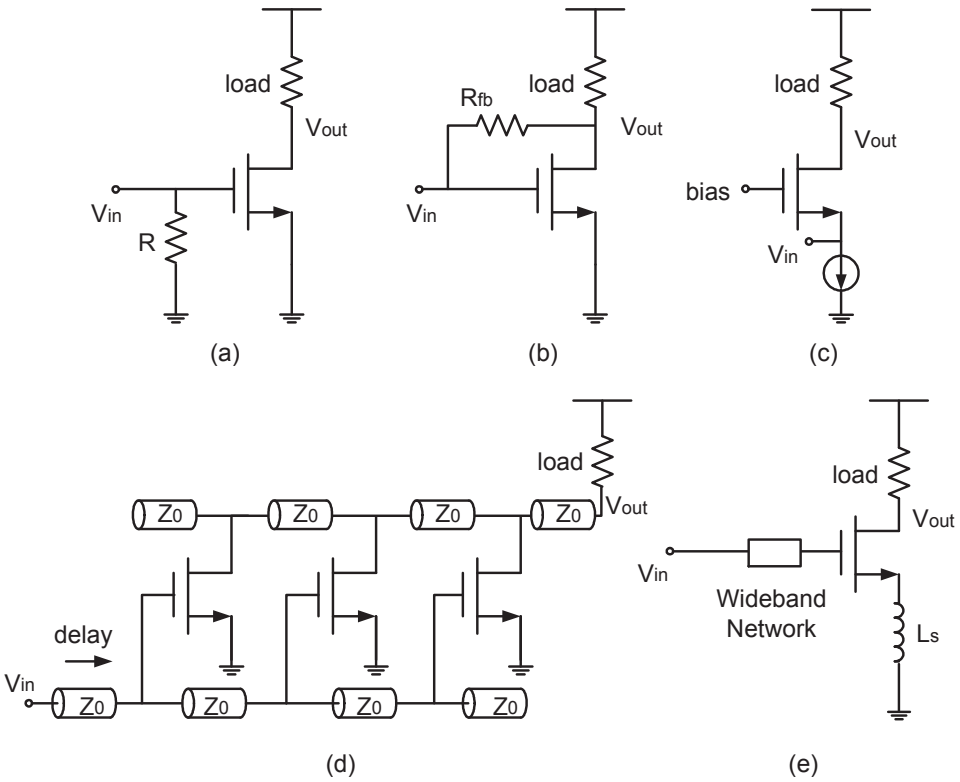

Figure 5.3: Different wideband LNA: (a)Resistor matching wideband LNA, (b) resistive shunt-feedback LNA, (c) common-gate wideband LNA, (d) distributed wideband LNA, and (e) inductive degeneration wideband LNA.

5.3 UWB Receiver Circuit Topology

The UWB LNA plays a vital role in the UWB radar and UWB sensor systems. A UWB LNA must operate with an acceptable gain and have an input matching to a 50 Ω antenna over the entire UWB frequency band. A truly integrated UWB SoC solution requires the seamless integration between the transmitter, the antenna, and the receiver. Implementation in a standard CMOS process allows integration of the RF front-end with the baseband digital blocks. The most recently reported UWB CMOS radar transceivers in [96, 97, 98] employ a simple wideband amplifier as the first stage LNA in the receiver without UWB band impedance matching. The reported receivers use two different ports for one transmitting antenna and one receiving antenna or separated diplexer built on a different substrate. To data, none of the reported UWB receivers have been fully integrated with a diplexer on the same substrate to achieve the complete seamless integration.

Several circuit topologies, such as distributed structure, resistive feedback structure, and balanced structure, common-gate structure, and inductive degeneration structure can be adopted for UWB front-end amplifier design [99, 100, 102, 106, 105, 101, 108, 109, 110, 111]. Each topology has its own advantages and disadvantages in different applications. This section reviews each receiver front-end topology, and then introduces the proposed receiver front-end topology.

The resistor-terminated amplifier, as illustrated in Figure 5.3 (a), is the simplest circuit topology that can achieve wideband input matching, while providing wideband gain at the same time. The major drawbacks of this topology is that the termination resistor R introduces an additional 3dB noise. In addition, as the frequency increases, both noise performance and gain are badly deteriorate.

Figure 5.3 (b) shows the circuit structure of a resistive shunt-feedback amplifier. This configuration, when applying a feedback resistor R_{fb}, has an input impedance and an output impedance of

$$R_{in} = \frac{R_{load} + R_{fb}}{1 + g_m R_{load}} \tag{5.14}$$

$$R_{out} = \frac{R_{source} + R_{fb}}{1 + g_m R_{source}} \tag{5.15}$$

When the source impedance R_{source} and the load impedance R_{load} are equal, both good input and output matching in a very wide band are achieved [99, 100]. At RF frequency, the Miller effect from the gate-drain capacitance C_{gd}, together with R_{fb}, moves the dominant pole to lower frequency and significantly degrades the gain at high frequency. This dominant pole can be reduced by a neutralization technique at the cost of an additional circuit complexity and noise and power headroom. In terms of noise performance, this topology is not the best candidate because R_{fb} and a possible degeneration resistor contribute a large amount of noise. Another drawback of the shunt-resistive feedback topology is that the feedback loop is sensitive to the process variation and parasitic capacitance C_{gd} and C_{gs}. Since the shunt feedback control the bias, gain, and input/output impedances, the feedback loop values need to be precisely controlled. The on-chip resistor process variation can affect the performance

of the shunt-resistive feedback amplifier.

Another very attractive UWB LNA topology is the common-gate configuration, as shown in Figure 5.3 (c). The real part of the input impedance of the common-gate structure, seen at the source, is approximately a constant, $1/g_m$. This configuration can easily achieve a wide band input match if $1/g_m$ is adjusted to the signal source impedance R_s. The common-gate transconductance g_m is often a small value when biased under a strong inversion region and less frequency dependent. The only major drawback is the significantly degraded noise figure at frequencies in GHz range.

The distributed amplifier structure, as shown in Figure 5.3 (d), can achieve high gain for high bandwidth. This topology embeds the input capacitance at the gate of each transistor into a LC network corresponding to a transmission line. Since the characteristic impedance Z_0 is equal to the source impedance, the input signal sees each node as a matched load rather than a frequency pole. Ideally, the transmission line has an infinite bandwidth. Therefore, an extremely high bandwidth is achieved, and only the output pole dominates the bandwidth. However, this structure employs lumped LC networks, which is very expensive in terms of chip area for input 50 Ω matching. The on-chip inductor has a low quality factor and high loss, which will lead to a poor noise performance. Since the LC transmission line does have delay, the distributed amplifier output could be delayed differently from each amplifier stage. Furthermore, the total power consumption and chip area of the overall circuit are inevitably large [101, 102].

Figure 5.3 (e) shows the inductive degeneration common-source amplifier structure. The degenerative inductor L_s introduces a real part impedance at the gate of the transistor [105]. A small signal equivalent circuit of this topology is shown in Figure 5.4. The inductive component at the gate cancels with the parasitic capacitance C_{gs}, leaving only the real part of the input impedance Z_{in}. Z_{in} can be derived from the small signal circuit as

$$Z_{in} = \frac{1}{sC_{gs}} + sL_s + \frac{g_m}{C_{gs}} \cdot \frac{sL_s}{s} + sL_g = s(L_g + L_s) + \frac{1}{sC_{gs}} + \omega_T L_s \tag{5.16}$$

where the cut-off frequency ω_T is defined as $\omega_T{=}g_m/C_{gs}$. The gate-drain parasitic capacitance C_{gd} will introduce the Miller effect, which will be discussed in later sections.

Equation (5.16) shows that the input impedance matching only occurs at the resonance

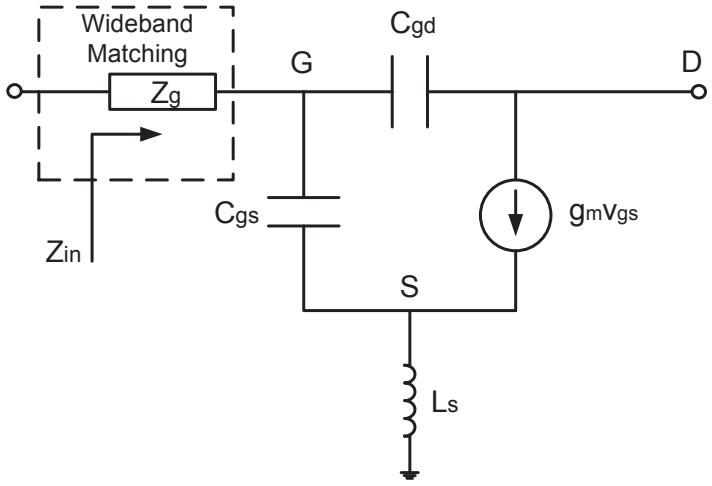

Figure 5.4: Small signal equivalent circuit of the inductor degenerative common-source amplifier

frequency

$$\omega_0 = \frac{1}{\sqrt{(L_s + L_g) \cdot C_{gs}}} \tag{5.17}$$

To expand this narrow band input matching, a wideband matching network is proposed at the gate to achieve an input matching from 3 GHz to 10 GHz [105]. Compared with all of the topologies above, the common source configuration is the best choice in terms of design performance and design robustness.

5.4 Diplexer and LNA Co-design

In a UWB system, the separated LNA and diplexer laminates and the bonding wires between them may cause large distortion and loss to the signals. To reduce the signal path loss between two separate laminates or substrates and improve the receiver system performance margin, integration of the diplexer and the receiver front-end onto the same chip is becoming an inevitable trend in the SoC era. A co-designed antenna diplexer and LNA on the same substrate with a careful UWB frequency impedance matching not only increases the integration level and reduces costs, but also greatly improves the overall receiver system performance.

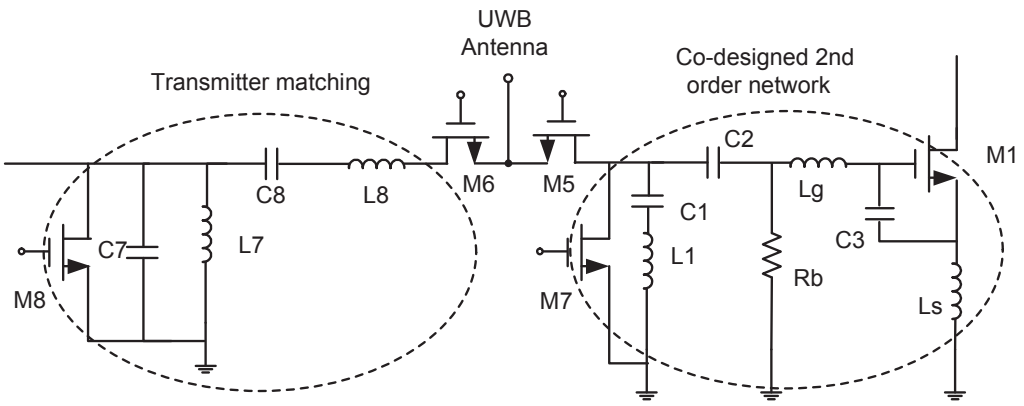

Figure 5.5: Schematic of proposed UWB band diplexer

The proposed receiver front-end LNA, integrated with an UWB band antenna diplexer, is shown in Figure 5.5. Figure 5.6 shows the complete circuit of the LNA stage. The LNA stage (M1 and M2) employs a shunt-peaking cascode common source configuration with inductance degeneration as the amplifier core. NMOS transistors M5 and M7 connected as a shunt switch to control the incoming RF signal path to the LNA input. This section focuses on the design approach of the integrated receiver front-end.

5.4.1 Antenna Diplexer Input Matching

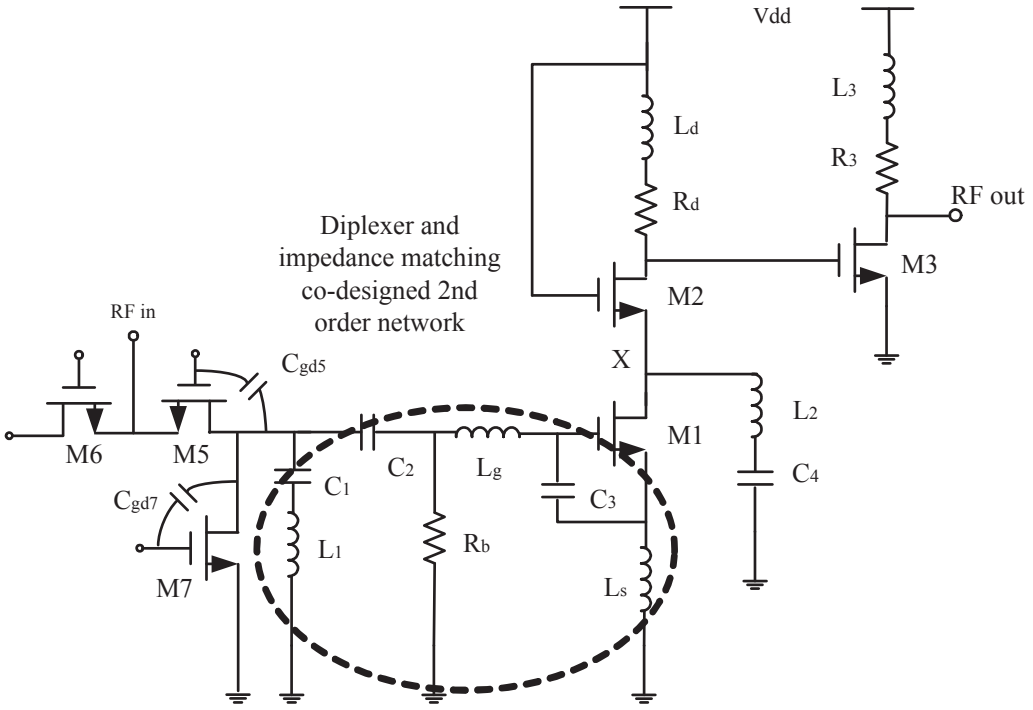

Figure 5.6: Schematic of the proposed UWB receiver front-end

A few types of matching networks, such as T type network, π network, L type network, Butterworth network, and Chebyshev network, can be applied for RF matching. When designing for UWB frequency matching, the choices are limited to Butterworth and Chebyshev network. The Chebyshev network provides a steeper roll-off than the Butterworth network, with a lower insertion loss at a cost of in-band ripple. For a receiver front-end, the input reflection coefficient Γ can be expressed in term of the pass band ripple R_{ipple} as

$$|\Gamma|^2 = \frac{R_{ipple} - 1}{R_{ipple}} \tag{5.18}$$

Equation (5.18) shows that for a -10 dB or smaller reflection coefficient, the ripple of the front-end matching network should be smaller than 1.11 or 0.915 dB in logarithm.

A second order Chebyshev input network is shown in Figure 5.7. C_2 and L_2 are the shunt connected branch. Both the source and the load are 50 Ω. This matching network is constructed from low-pass to band-pass filter transformation and de-normalization using the normalized low-pass coefficients with a ripple of 0.1 dB. These coefficients are tabulated in Table 5.1 [107]. The bandwidth is set from 3.0 GHz to 10.6 GHz with a center frequency at

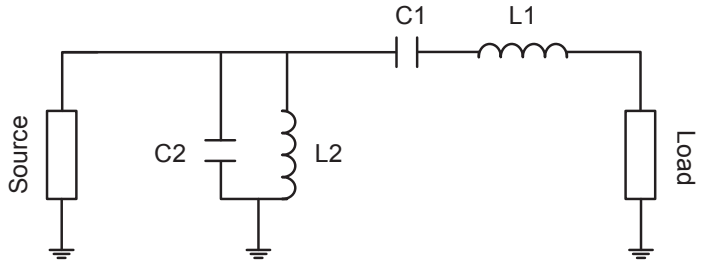

Figure 5.7: Schematic of the second order Chebyshev network

6.8 GHz.

Table 5.2 shows the nominal structure values for a second order Chebyshev input network and a second order Butterworth input network. The Chebyshev structure is a good compromise between area and power consumption. For the Butterworth structure, the C_1, which will be replaced by the gate-source capacitance, is calculated to be 1.32 pF. This value would require a large transconductance g_m in order to achieve a moderate gain, and this is not preferable in a high frequency design.

Table 5.1: Chebyshev normalized table at ripple=0.1 dB [107]

n	g_1	g_2	g_3	g_4	g_5	g_6
1	0.3052	1.0000	-	-	-	-
2	0.8430	0.6220	1.3554	-	-	-
3	1.0315	1.1474	1.0315	1.0000	-	-
4	1.1088	1.3061	1.7703	0.8180	1.3554	-
5	1.1468	1.3712	1.9750	1.3712	1.1468	1.0000

Table 5.2: Nominal input network component for different structure types

Type	n	L_2 (nH)	C_2 (fF)	L_1 (nH)	C_1 (fF)
Chebyshev	2	1.787	335	0.619	869
Butterworth	2	2.2	350	0.65	1320

In the proposed schematic in Figure 5.6, the parasitic capacitance of transistor M5 and M7, C_3, C_{gs1}, the gate, and the source inductors form a second order shunt-series Chebyshev matching network to match 50 Ω antenna impedance in 3.1-10.6 GHz UWB band. The

parasitic capacitance C_{gd5}+C_{gd7} and L_1 form the shunt branch corresponding to C_2 and L_2 in Figure 5.7. C_{gs1}, L_g, and L_s are embedded in the series branch corresponding to C_1 and L_1 in Figure 5.7. Capacitor C_3 is added to increase the degree of freedom in design. The passband ripple is designed to be 0.1 dB, the center frequency is located at 6.8 GHz, and the frequency span for S_{11}≤-10 dB is designed to be from 3 GHz-10.6 GHz.

Again, we come back to revisit the narrow band scenario: For the LNA core local matching network, the input impedance seen from the transistor M1 gate inductor L_g is

$$Z_{in} = (Ls + Lg)\, s + \frac{1}{(C_3 + Cgs1)\, s} + \omega_T Ls \tag{5.19}$$

where the cut-off frequency ω_T is equivalent to the gain bandwidth product and is a function of g_{m1} and nodal dominant capacitance. The degenerative inductance L_s introduces a real part for the input impedance, while L_g and (C_{gs1}+C_3) dominate the imaginary part of the input impedance. At resonance frequency, L_g and (C_{gs1}+C_3) cancel with each other and the impedance appears to be a pure real resistance, which is dominated by g_{m1}/(C_{gs1}+C_3) and L_s. By choosing appropriate g_{m1}, C_3, and L_s, the input impedance can be matched to 50 Ω. At the same time, this local matching network is embedded inside the full UWB band matching network to achieve a full band resonance and 50 Ω matching.

In GHz frequencies, the non-quasi static gate resistance $r_{g,NQS}$ and the parasitic gate resistance R_G start to play an important role. Therefore, the real part of the input impedance becomes

$$\mathrm{Re}(Z_{in}) = r_{g,NQS} + R_G + \omega_T L_S \tag{5.20}$$

The $r_{g,NQS}$ and R_G need to be compensated by reducing L_s in order to have Re(Z_{in})=R_s.

One series NMOS switch and one shunt NMOS switch are employed on each side of the antenna port. Two switches are turned on and off in a complementary fashion. This series-shunt connection is a compromise between insertion loss and port isolation. Knowing that the typical on-chip inductor Q is approximately 10, the insertion loss of the diplexer with different switch sizes, including the impedance matching network, is plotted in Figure 5.8 (a). Switch size with W=120 μm has the lowest insertion loss, and switch with W=40 μm

has the highest insertion loss of 1 dB, but achieves the maximum flatness inside the UWB band. Figure 5.8 (b) shows the isolation plot for different switch sizes. Switch with W=40 μm apparently has the best isolation owing to its small parasitic capacitance and large resistance.

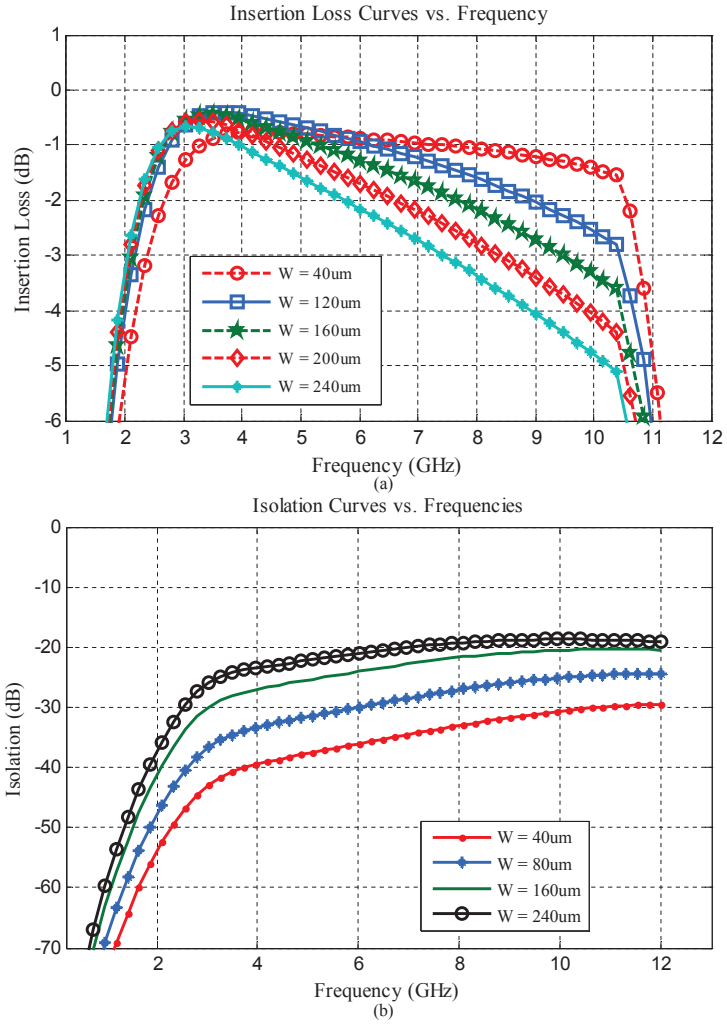

Figure 5.8: (a) Insertion loss for switch transistor W=40 μm, W=120 μm, W=180 μm, W=200 μm, and W=240 μm, (b) Ports isolation for switch transistor W=40 μm, W=120 μm, W=180 μm, W=200 μm, and W=240 μm

5.4.2 Gain Stage

In high frequency CMOS design, the transistor transconductance g_m becomes the key parameter governing most of the design tradeoffs. This g_m can be rewritten as

$$g_m = \frac{\partial I_{DS}}{\partial V_{GS}} = 2K\frac{W}{L}(V_{GS} - V_{th})\frac{1}{1 - \Lambda V_{DS}}\frac{1}{1 + \Theta(V_{GS} - V_{th})} \tag{5.21}$$

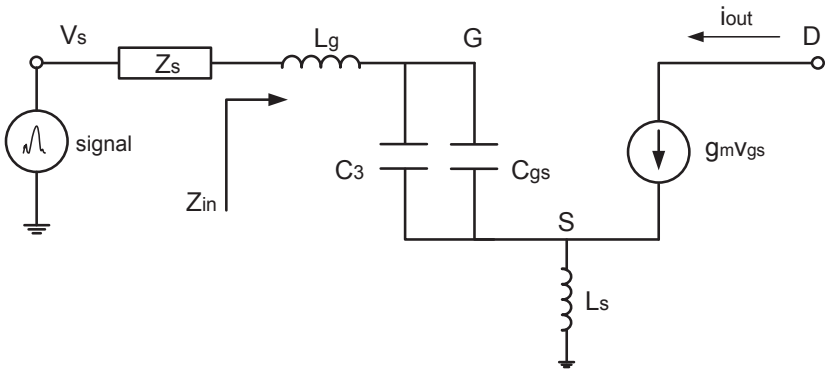

Figure 5.9: Small signal circuit of transistor M1 in LNA

where K = $\frac{1}{2}\mu_n C_{ox}$. The term $1/(1-\Lambda V_{DS})$ describes the effect of channel-length modulation, and $1/(1+\Theta(V_{GS}-V_{th}))$ describes the effect of short-channel velocity saturation in g_m expression. Θ is a process related coefficient. To reduce the short channel effect, a smaller V_{GS}-V_{th} is desired. But reducing V_{GS}-V_{th} will result in a low cut-off frequency ω_T. This is a fundamental trade-off between power and bandwidth in GHz range design, and this trade-off is the main philosophy followed throughout the UWB SoC design.

As seen in Figure 5.6, the stacked transistors M1 and M2 form a cascode topology and provides small-signal gain for the UWB LNA. The major role of transistor M2 is to reduce the Miller effect, improve reverse isolation, and boost the intrinsic output impedance by a factor of $g_{m2}r_{O2}$ as well. Since the currents flowing through M1 and M2 are equal, the overall effective transconductance G_m is donimated by the amplifying transistor M1 and the transfer function H(s) of the impedance matching network. Using the small-signal equivalent circuit of M1 in Figure 5.9, the G_m can be derived as

$$G_m = \frac{i_{out}}{v_s} = g_{m1}H(s) = \frac{g_{m1}}{s(C_{gs1}+C_3)(sL_s+sL_g+Z_s)+1+g_{m1}sL_s} \tag{5.22}$$

The actual $|H(s)|$ is less than unity because the gate-to-source voltage is less than the input voltage due to the input network insertion loss. Equation (5.16) has shown

$$sL_s + sL_g + \frac{1}{s(C_{gs1}+C_3)} = 0 \tag{5.23}$$

Equation (5.22) can be simplified to

$$G_m = g_{m1} \cdot \frac{1}{2R_s s(C_{gs1} + C_3)} \tag{5.24}$$

The LNA voltage gain can be expressed as

$$\begin{aligned} A_V &= \frac{V_{out'}}{V_{in}}(s) \\ &\approx \frac{-G_m \cdot [(g_{m2} + g_{mb2}) r_{O1} r_{O2} || (R_d + sL_d)]}{\left(1 + \frac{s}{\omega_{in}}\right) \cdot \left(1 + \frac{s}{\omega_{out}}\right) \cdot \left(1 + \frac{s}{\omega_X}\right)} \end{aligned} \tag{5.25}$$

where the input pole ω_{in} is

$$\omega_{in} \approx \frac{1}{50\left[C_{gs1} + C_3 + \left(1 + \frac{g_{m1}}{g_{m2}}\right) C_{gd1}\right]} \tag{5.26}$$

the output pole ω_{out} is

$$\omega_{out} \approx \frac{1}{R_d(C_{gs3} + C_{gd2})} \tag{5.27}$$

and the inter-stage pole ω_X is estimated as

$$\omega_X \approx \frac{1}{\left(1/g_{m2} || r_{O1}\right)(C_{gs2} + C_{gd1})} \tag{5.28}$$

To achieve high bandwidth, the transistor M1 is biased in a large V_{GS1} and the transistor length L is kept minimum. However, the overdrive voltage V_{GS1}-V_{th} is not to exceed 0.4 V to avoid getting into the velocity saturation region, where the transconductance g_{msat} becomes a function of transistor width, C_{ox}, and the maximum velocity saturation voltage V_{sat}, and no longer increases with the drain current.

A cascaded common source amplifier is employed to work as a high frequency driver to drive 50 Ω output load. A source follower is a common choice at low frequencies. However, as the frequency increases to GHz range, the output impedance Z_{out3} tends to reach the input impedance Z_{in3} because the gate-source capacitance of M3 C_{gs3} will short the gate and the source. In this case, the output impedance value is several orders of magnitude higher than

50 Ω. This C_{gs3} high frequency pass will degrade the gain to far below the unity. Thus in high frequencies, the common source buffer appears to be a better choice for output impedance matching. The transfer function of a common source buffer is approximated as

$$\frac{Vout}{Vin'} \approx \frac{-g_{m3}[(R_3 + sL_3)||50]}{\left(1 + \frac{s}{\omega_{out}}\right) \cdot (1 + 25 \cdot C_L \cdot s)} \tag{5.29}$$

where the shunt peaking inductor L_3 contributes a zero to extend the bandwidth. Let $1/g_{m3} \approx (R_3||50)$, then the buffer exhibits a unity gain at high frequencies while achieving a 50 Ω output matching. The dominant pole of the overall gain transfer function is located at the drain of the transistor M3. Since this output matching buffer forms a voltage divider, the voltage gain is 6 dB higher than the power gain.

5.5 Noise Analysis of the Receiver Front-End

As we have seen in the previous section, the first stage of the UWB receiver contributes the most of the overall noise in an UWB system. This section begins with the discussion of the receiver noise model, followed by the noise analysis for the complete UWB receiver front-end.

Figure 5.10 (a) shows the simplified noise model of the proposed receiver front-end after applying Thevenin equivalent transformation. Noise of independent drain load is assumed. This model includes the LNA and diplexer matching network for a complete noise analysis. The main noise sources are amplifier transistor M1 and switching transistors M5 and M7. Other noise sources are the equivalent thermal noise from biasing resistor R_b and thermal noise of the low Q lossy on-chip integrated inductors. The noise source of M1, which is the small signal thermal noise of the channel resistor, can be represented as

$$\overline{i_{nd}^2} = 4kT\gamma g_{d0}\Delta f \tag{5.30}$$

$$\overline{i_{ng}^2} = 4kT\delta g_g \Delta f \tag{5.31}$$

where g_g is expressed as $\omega^2 C^2{}_{gs}/5g_{d0}$. This is a frequency dependent term. In another word, $\overline{i_{ng}^2}$ is the induced gate noise at non quasi-static state, i.e., as frequency ω goes to zero, g_g

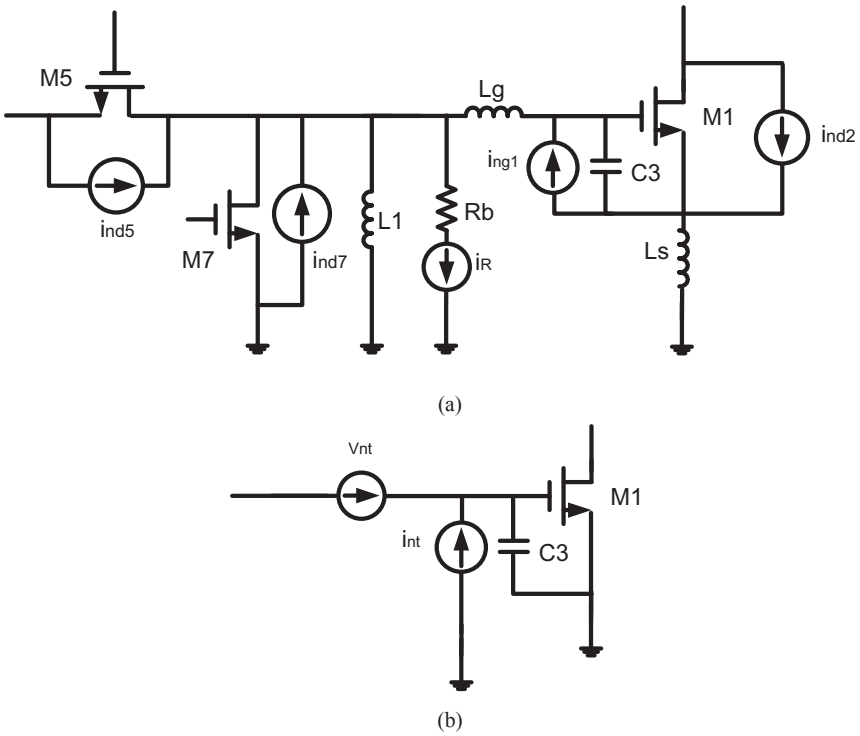

Figure 5.10: Complete noise model of the receiver front-end

goes to zero and the induced gate noise is zero. The noise of switching transistors M5 and M7 are solely represented by the channel noise current i_{nd} since the transistors turned-on state is a steady state.

The thermal noise sources can be replaced by an equivalent input correlated noise source by bringing i_{nd1} to the input gate of transistor M1. The noise sources i_{nd5} and i_{nd7} of M5 and M7 and resistor noise are uncorrelated with i_{ng1}, thus they can be superimposed into a single noise source i_{nt}. The simplified noise model after superimposition is shown in Figure 5.10 (b).

$$\overline{i_{nT}^2} = \frac{[j\omega(C_3+C_{gs1})]^2\overline{i_{nd1}^2}}{g_{m1}^2} + \overline{i_{ng1}^2} + \overline{i_{nd5}^2} + \overline{i_{nd7}^2} + \frac{4kT\Delta f}{R_{Tot}} \tag{5.32}$$

$$\overline{v_{nT}^2} = \frac{\overline{i_{nd}^2}}{g_{m1}^2} + [j\omega(L_S + L_g + L_1)]^2\overline{i_{nT}^2} \tag{5.33}$$

where R_{Tot} represents R_b and loss from the inductors. Similar to the derivation procedure

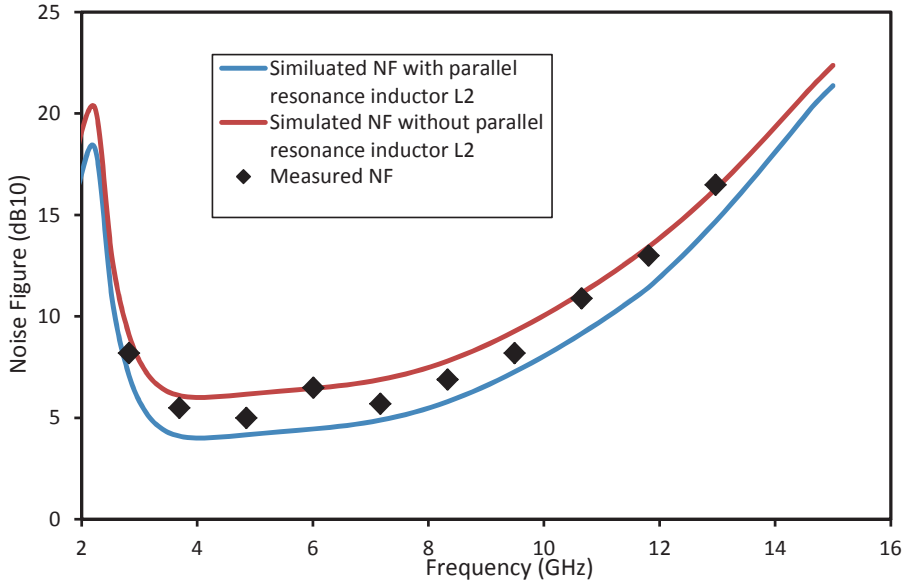

Figure 5.11: Simulated and measured noise figure of the receiver front-end

in [103], the input noise i_{nt} is decomposed into two components: the correlated noise i_{nc} and the uncorrelated noise i_{nu}, where i_{nc} is composed of the correlated terms of i_{ng1}, input-referred form of noise current i_{nd1}, and $i_{nd5,7}$. The correlation admittance Y_c=G_c+jB_c can be expressed as

$$\begin{aligned} Y_c &= \tfrac{i_{nc}}{v_{nt}} \\ &= \left(\frac{i_{nd1} j\omega(C_{gs1}+C_3)/g_{m1} + 4kT\delta g_{g1}|c|\Delta f}{v_{nt}} + \frac{i_{nd5}+i_{nd7}+4kT\Delta f/R_T}{v_{nt}} \right) \\ &= j\omega(C_{gs1}+C_3) - \left(j\omega(C_{gs1}+C_3) g_{m1} c \sqrt{\tfrac{\delta}{5\gamma}} - \frac{4kT\gamma g_{d05,7}\Delta f}{\frac{4kT\gamma g_{d01}}{g_{m1}} + j\omega L_{s,g,1} i_{nt}} - \frac{4kT\Delta f}{R_T v_{nt}} \right) \end{aligned} \tag{5.34}$$

where the value of c is approximately equal to 0.3 [103]. The transistors M5 and M7 are biased in deep linear regions, in which $\gamma_{5,7}$ are equal to the unity.

The equivalent noise resistance R_n and noise transconductance G_u, are defined and expressed as

$$\begin{aligned} R_n &= \frac{\overline{v_{nt}^2}}{4kT\Delta f} \\ &\approx \frac{\gamma}{g_{m1}\alpha} + (j\omega L_T)^2 \left[\frac{(j\omega C_T)^2 \gamma}{g_{m1}\alpha} + \delta g_{g1} + 2g_{d05,7} \right] \end{aligned} \tag{5.35}$$

$$\begin{aligned} G_u &= \frac{\overline{i_u^2}}{4kT\Delta f} \\ &= \frac{\delta\omega^2 C_{gs1}^2(1-|c|^2)}{5g_{d01}} \end{aligned} \tag{5.36}$$

where α=g_m/g_{d0}, and C_T=C_{gs1}+C_3. The noise factor can be expressed using these terms as

$$F = 1 + \frac{G_u + |Y_c + Y_s|^2 R_n}{G_s} \tag{5.37}$$

where G_s is the source transconductance and is equal to 1/50. The minimum noise factor occurs when Y_c and Y_s could cancel out each other. The optimum B_{opt}=-B_c=B_s, the optimum G_{opt}=G_s=$\sqrt{G_u/R_n + G_c^2}$. After expansion and simplification,

$$G_{opt} \approx \alpha\sqrt{\frac{5(1+\omega^4 L_T^2 C_T^2)\gamma g_{d05,7}^2 + \delta\omega^2 C_T^2}{5\gamma(1+\omega^4 L_T^2 C_T^2)}} \tag{5.38}$$

Substituting G_u and Y_c into F, the noise factor expression is

$$F \approx 1 + R_s \left\{ \begin{array}{l} \frac{\delta\omega^2 C_T^2(1-|c|)^2}{5g_{d01}} \\ +A\left[\begin{array}{l} \frac{\gamma(1+\omega^4 C_T^2 L_T^2\gamma)}{g_{m1}\alpha} + \\ \omega^2 L_T^2(\delta g_{g1} + 2g_{d05,7}) \end{array} \right] \end{array} \right\} \tag{5.39}$$

where

$$A \approx \sqrt{g_{m1}^2 + \omega^2 C_T^2\left(1 - g_{m1}|c|\sqrt{\frac{\delta}{5\gamma}}\right)^2} \tag{5.40}$$

To have a small noise figure, a high cut-off frequency ω_T is desired. This can be achieved by a large V_{GS1}-V_{th1} and small transistor length L. This leads to a large drain source current. Therefore, it is the tradeoff between power and noise. The simulated noise figure plot of the overall LNA front-end is shown in Figure 5.11. This includes the noise contribution from the cascade transistor M2 and the buffer stage M3. The simulated minimum noise figure is 3.8 dB.

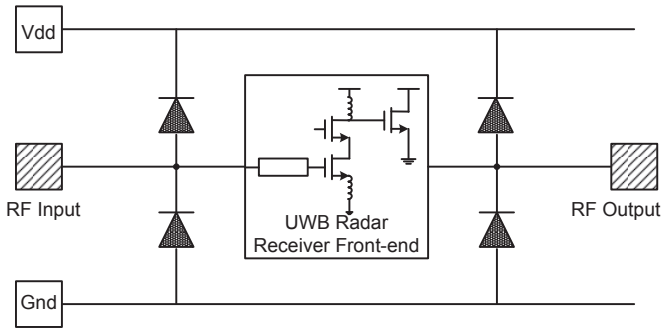

Figure 5.12: ESD protection diode string at RF I/O

5.6 ESD Diode Protection

One of the commonly used input/output electrostatic discharge (ESD) protections in CMOS RF and high speed circuits is shallow trench isolation (STI) diode string. To protect the UWB receiver front-end from potential electrostatic damage during wafer ionization, handling, and testing, STI diode strings have been added at RF signal input/output to protect the receiver core. This protection scheme is illustrated in Figure 5.12.

The STI diode in IBM RF CMOS process consists of P+ region and N+ region, located in an n-well or p-well on top of p-substrate. The design parameters associated with parasitic capacitance include the anode region area, the cathode region area, the perimeter of the device, and the spacing between the anode-cathode regions.

From the ESD performance perspective, the diode string should have as large an area as possible, provided that the design can accommodate the area. From the RF circuit performance perspective, the diode string brings in additional parasitic capacitance, slowing down the signal speed and receiver bandwidth. A compromise has to be made between potential hazardous ESD events and receiver front-end performance.

5.7 Implementation of The Receiver Front-End

The UWB receiver diplexer and LNA are implemented in a 130 nm seven-metal CMOS process. The on-chip capacitors were implemented using metal-insulator-metal structure. The spiral inductors were implemented on the top metal with a shield ground plane.

The LNA stage and output buffer stage draw a total current of 11 mA from the 1.2 V

power supply. The diplexer switch size of transistors M5, M6, and M7 are chosen to be 40 μm for a good compromise between insertion loss and isolation. The width of M1 is chosen to be 200 μm for noise optimization and gain. The width of M2 is chosen to be 80 μm to compromise between bandwidth and noise. The voltage headroom is set by the load R_d, which is selected to be 60 Ω.

For the buffer amplifier, the output will introduce large parasitic capacitance; without the shunt-peaking inductor, the gain will drop at high frequency. An on-chip shunt-peaking inductor was considered at the beginning. However, the low quality factor of the on-chip inductor will bring the same issue: The signal gain is reduced since the equivalent R_p=ωLQ, and R_p is proportional to the gain. We want to use high Q inductor wherever is possible. Since in the buffer stage the shunt-peaking inductor is directly connected to an output pad, the output buffer shunt-peaking inductor L_3 can be realized by the bonding wire inductance. The bonding wire can be regarded as a high Q (20 50) inductor with a few nH (approximately 1 nH per 1 mm bonding wire [48]).

The buffer stage uses a separate pad $V_{ddbuffer}$ for wire bonding from 1.2 V to buffer core. The buffer core M3 size is set to 120 μm. All the transistors in the design are set to minimum length (0.13 μm) in order to have an optimized cut-off frequency.

Table 5.3: Diplexer matching network components

Components	Values
L_s	1.069 nH
L_g	1.6 nH
L_1	1.313 nH
C_3	610.3 fF
C_1/C_2	Coupling capacitor

The diplexer input matching network for the transmitter side is not presented in this paper. The diode strings are employed at the RF input and output pads to provide ESD protection. Each diode string introduces an additional few hundred fF parasitic capacitance to the input and output stage of the receiver. The matching network is re-optimized using the Smith chart impedance circle to compensate the matching frequency shift caused by diode strings. The optimized input impedance is shown in Figure 5.13. Table 5.3 shows

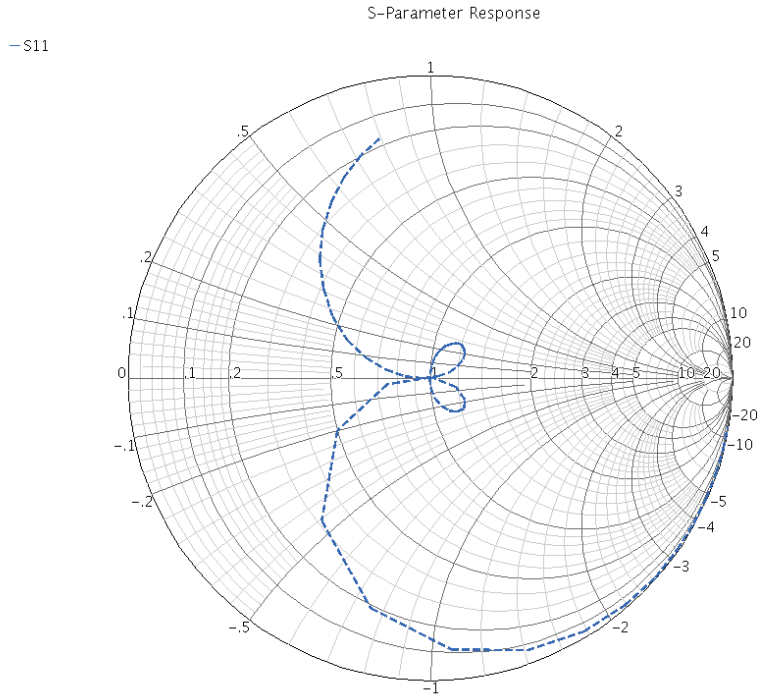

Figure 5.13: Input matching S11 optimization using Smith chart

the finalized component values for the receiver diplexer-LNA matching network after re-optimization. The chip micrograph of the receiver front-end is shown in Figure 5.14. The overall die area excluding the analog I/O pads is 0.5 mm^2.

5.8 Measurement Results

The receiver front-end was fabricated in IBM 130 nm CMOS technology, packaged in a high frequency cavity and test fixture for measurements. The receiver LNA were measured under the power supply voltage of 1.2 V. Agilent network analyzer and spectrum analyzer were used for measurements.

Figure 5.16 shows the measured and simulated input matching of the receiver front-end. Compared to the simulated S11, the measured S11 is shifted to lower frequency due to the introduced parasitic loss. A minimum matching of -14 dB is achieved over the entire UWB band. Fig. 5.17 shows the measured and simulated gain of the receiver front-end under different bias currents. The maximum power gain achieved in the UWB band is 16 dB, and the bandwidth is 3.3-9.9 GHz. Figure 5.18 shows the measured output matching of the receiver front-end and the measured inverse isolation. A good output matching of -10 dB and

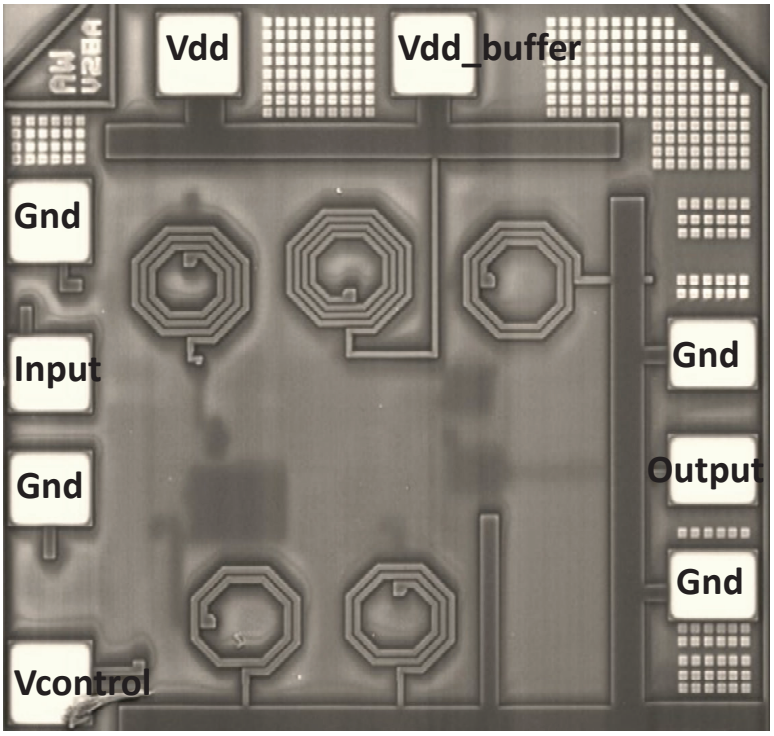

Figure 5.14: Micrograph of the receiver front-end die

reverse isolation of -22 dB are achieved. The simulated and measured forward group delay is shown in Figure 5.19. The forward group delay measures the signal distortion in the UWB band, and this is of particular interest in radar applications over the entire UWB band. The measured average group delay is 400 ps. The sharp variations of the group delay outside the 3.1-10 GHz band can be the result of the un-matched impedance of the pads outside the UWB frequency band, introducing further signal distortions.

The measured noise figure plot of the overall LNA front-end is shown in Figure 5.11. The minimum noise measured in the UWB band is 4.8 dB. The input-refereed 1 dB compression curve of the receiver front-end is shown in Figure 5.20 (a). The test was performed at 6 GHz. The 1dB compression point (IP1) is -13.1 dBm. Figure 5.20 (b) is the plot of the third order intermodulation (IIP3) curve of the receiver front-end at 6 GHz with a tone spacing of 100 MHz. The linearity is depending on V_{gs}-V_{th}. The IIP3 intercept point is -1.53 dBm.

The performance of the complete receiver front-end is tabulated and is compared to recently published values for UWB LNAs in Table 5.4. A figure-of-merit (FOM) is used to compare the performance between this work and the other published work. The FOM is

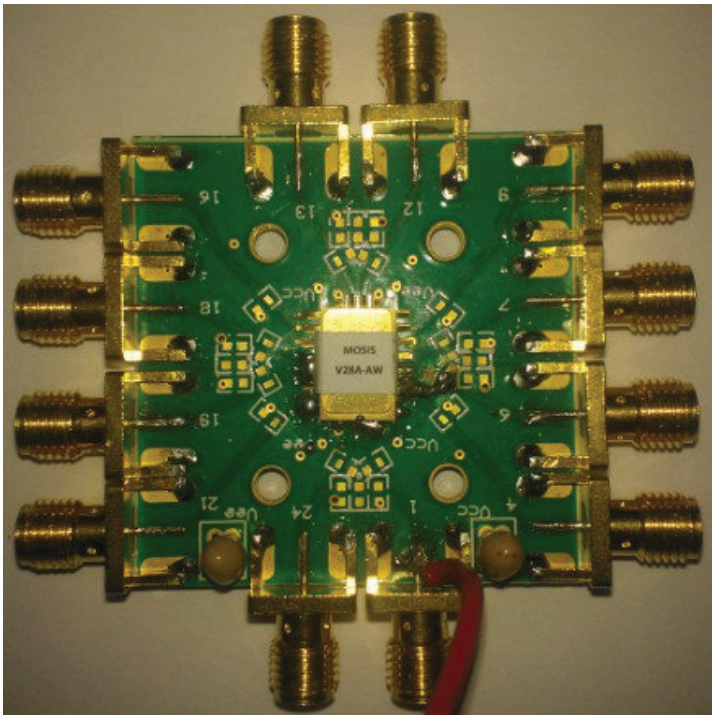

Figure 5.15: Receiver RF test fixture

defined as:

$$FOM = \frac{GBW}{(NF_{\min} - 1) \cdot P_{dc} \cdot |IIP3|} \tag{5.41}$$

where GBW is the product of the absolute value of the forward gain S21 and the bandwidth, while P_{dc} is the power dissipation in mW. NF_{min} is the minimum noise figure of the LNA.

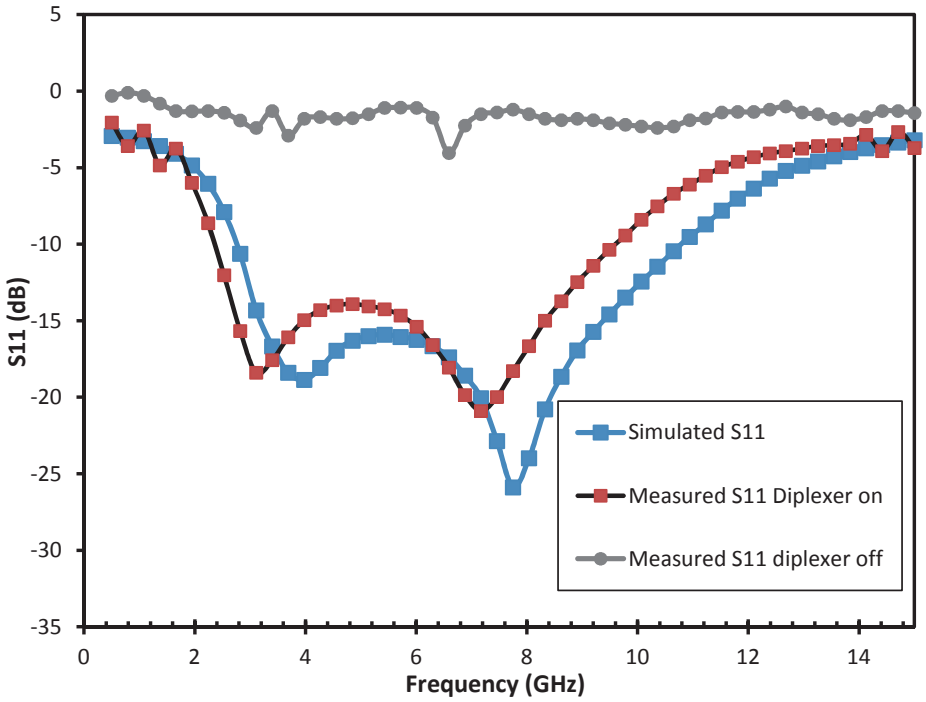

Figure 5.16: Measured and simulated receiver front-end S11

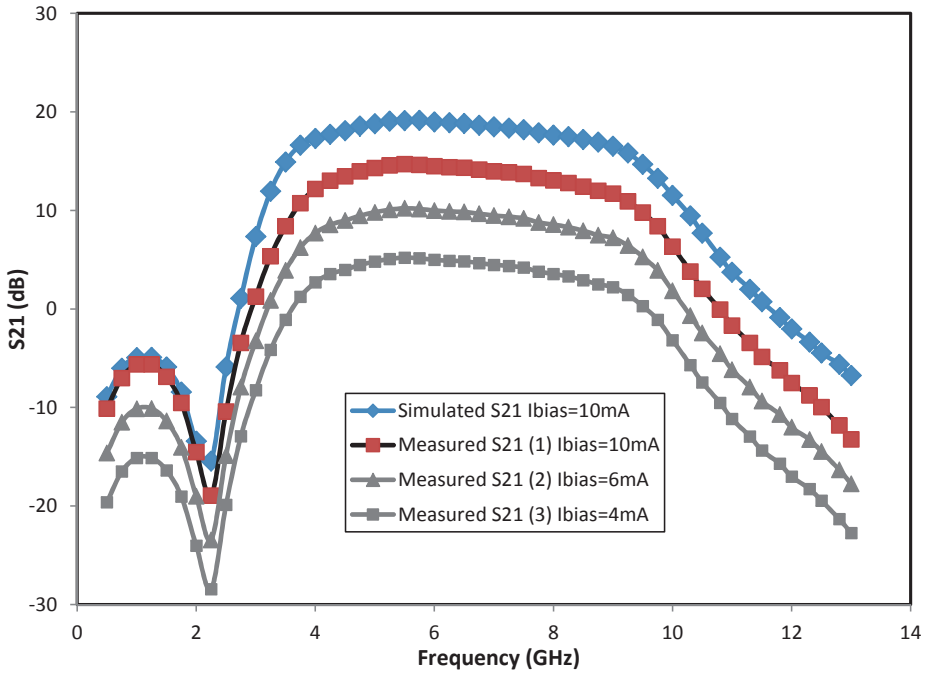

Figure 5.17: Measured and simulated S21 of the receiver front-end

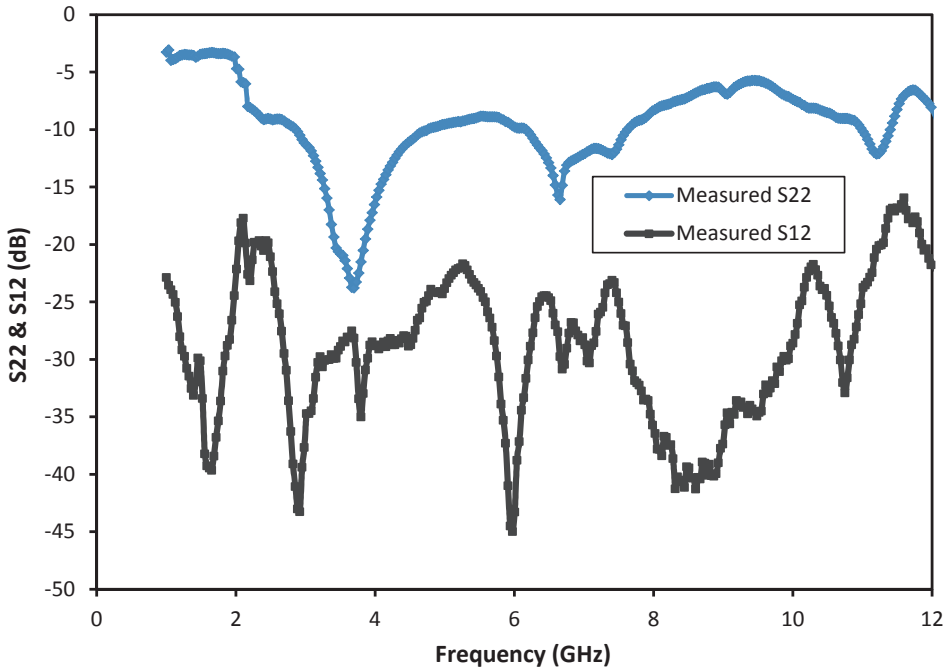

Figure 5.18: Measured S22 and S12 of the receiver front-end

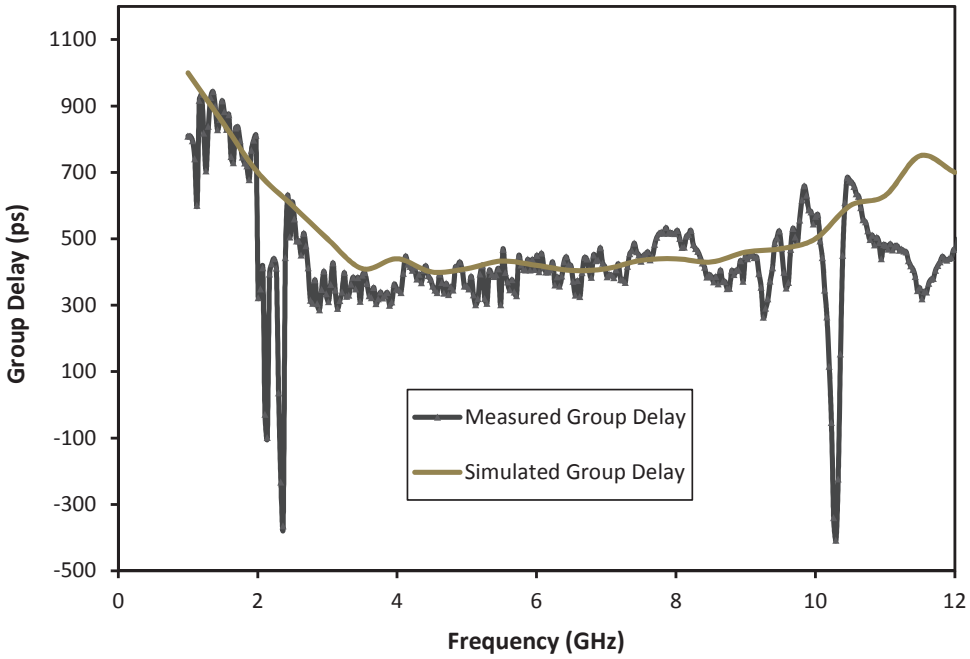

Figure 5.19: Measured forward group delay of the receiver front-end

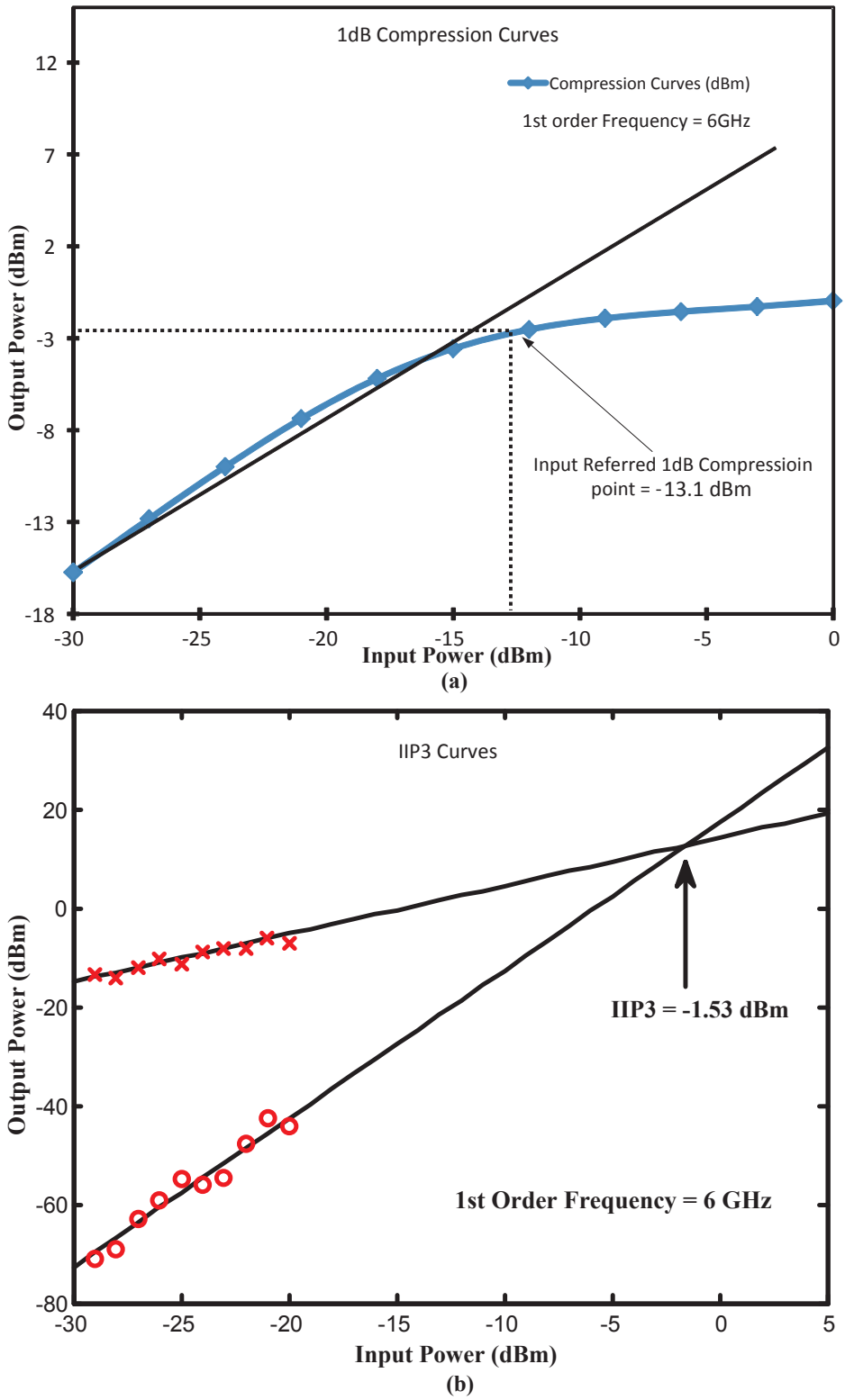

Figure 5.20: (a) Measured 1st compression curve, (b) measured IIP3 curve

The UWB receiver LNA front-end provides comparable performance at low power consumption while achieving a good matching and good linearity. The proposed design in this work exhibits higher FOM compared to other LNAs, except the design in [100] which is a reactive-feedback LNA with an increased circuit complexity due to the use of an on-chip transformer. The design in [101] and [102] are the LNAs with distributed structure, which consume large die area and high power dissipation, making them not a good candidate for low-power UWB system integration.

Table 5.4: Summary of UWB overall receiver front-end performance and comparison with previously published UWB LNA front-end

Designs	Technology	S_{11} [dB]	G_{max} [dB]	BW [GHz]	NF_{min} [dB]	IIP3 [dB-m]	Power [mW]	FOM
This Design(with UWB diplexer)	130 nm CMOS	$\leq$ -14	17	3.5-10	4.8	-1.53	13	1.462
[99]	130 nm CMOS	$\leq$ -7.3	12.4	3.1-10.6	3.7	-3.8	14.4	0.629
[100]	130 nm CMOS	$\leq$ -9.9	16.5	3.1-10.6	2.8	-5.1	9	1.498
[101]	180 nm CMOS	$\leq$ -8	8.1	0.6-22	4.3	N/A	52	N/A
[102]	130 nm CMOS	$\leq$ -12	16	1-10.6	4.5	N/A	26	N/A
[105]	180 nm CMOS	$\leq$ -9.9	9.3	2.3-9.2	4.0	-6.7	9	0.355
[106]	130 nm CMOS	$\leq$ -8.3	11	2-9.6	4.8	-7.2	19	0.161
[108]	130 nm CMOS	$\leq$ -10	14.5	3.1-10.6	4.5	-4.8	7	0.925
[109]	130 nm CMOS	$\leq$ -10	14	3.4-11	4.7	-5.3	30	0.181
[110]	180 nm CMOS	$\leq$ -9.5	13.2	3.1-10.6	4.5	-1.4	28	1.010
[111]	90 nm CMOS	$\leq$ -5	24.4	4-8	2	-7.7	9.2	1.378

5.9 Summary

A fully integrated UWB radar receiver front-end in standard 130 nm CMOS process is presented in this paper. To avoid loss of generality, some of the topics discussed were kept at a simplified level. The design approach and implementation of each circuit blocks were presented in different sections of this chapter. The receiver implementation was presented and discussed, followed by the measurements results of the receiver front-end.

The on-chip diplexer has 1 dB insertion loss and -30 dB isolation. The diplexer switch is co-designed with the receiver's input matching network to optimize for the power matching while achieving a good noise matching. An overall noise figure of 4.8 dB is measured. The receiver front-end achieves a full band matching and a maximum power gain of 16 dB. A good output matching and reverse isolation are demonstrated. The overall receiver front-end consumes an average power of 13 mW.

The good NF performance, high broadband gain, high integration, and low cost of the proposed UWB receiver front-end makes it a very competitive SoC solution for low-power UWB transceiver.

Chapter 6

Radar Performance

This chapter demonstrates the UWB radar prototype and presents the respiration measurement results using the built UWB radar prototype. Section 6.2 discusses the link budget of the transceiver and signal propagation of the UWB radar signal based on the Friis propagation model. Section 6.3 shows the overall performance summary of the radar transceiver, as well as the comparison to recently published similar radar transceiver work. Section 6.4 summarizes this chapter.

6.1 Radar Measurement

The entire radar transceiver circuit was fabricated using IBM 130 nm CMOS technology, packaged in a high frequency cavity and test fixture for testing and prototyping. The overall die area including the analog I/O pads is 2 mm^2. The micrograph of the transceiver chip is shown in Figure 6.1 (a).

The transmitter DCO was measured separately to verify the functionality, and the measurement results were shown in Chapter 4. The stand-alone measurement results of the receiver front-end were also shown in Chapter 5. The UWB radar transceiver measurement setup is shown in Figure 6.2. A pattern generator sends a gating signal at a pulse repetition frequency (PRF) of 10 MHz and a duty cycle of less than 3% to the transmitter input. The transmitter generates a Gaussian-modulated pulse and a rectangle-modulated pulse at a PRF of 10 MHz for testing. The pulse width is 1.5 ns and 2.5 ns, respectively. For both envelopes, the carrier frequency is set to 3.7 GHz, 6 GHz, and 7.5 GHz. The spectra of these two groups are shown in Figure 6.4. We can see that rectangular-modulated pulses have a higher sideband power and greater spectrum leakage in the adjacent GSM band. Gaussian-modulated pulses have a better fit in the FCC mask.

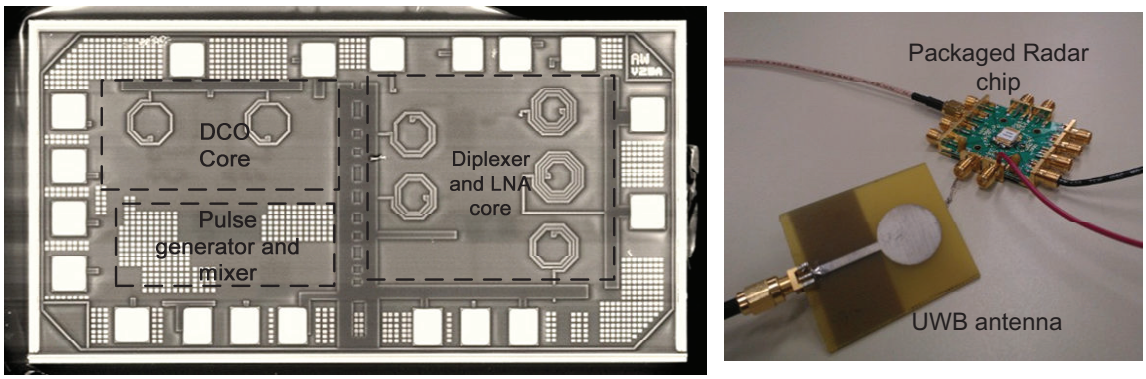

Figure 6.1: UWB radar prototype

Figure 6.1 (b) shows the UWB radar prototype built on a high frequency texture. The full band UWB circular patch antenna was built using a FR4 PCB board [113, 117]. A pattern generator was used to send a data sequence with a PRF of 10 MHz to the transmitter Tx_EN input. A fast digital scope was used to display the transmitter output at channel one and receiver-front output at channel two.

Both the measured transmitter output UWB signal in the Gaussian-modulated mode and the signal at the receiver output are shown in Figure 6.3. The PRF was 10 MHz. The carrier frequency was 3.7 GHz. The single pulse duration was 1.5 ns. In the radar test, a subject was sitting 30 cm away in front of the antenna so that the breathing of the subject could be detected. The measured TOA was about 4.2 ns (this includes the probe and cable propagation time). Figure 6.5 (a) illustrates the breathing mechanics and the UWB radar sensing mechanism when the human chest surface was at positions A, B, and C. Figure 6.5 (b), (c), and (d) show the measured waveforms during exhalation and inhalation when the chest surface is at different positions. The breathing measurement data were collected for 30 consecutive seconds and processed using the fast fourier transform (FFT) method. Figure 6.6 shows the breathing pattern in the time and frequency domains. The measured breathing rate was about 0.33 Hz.

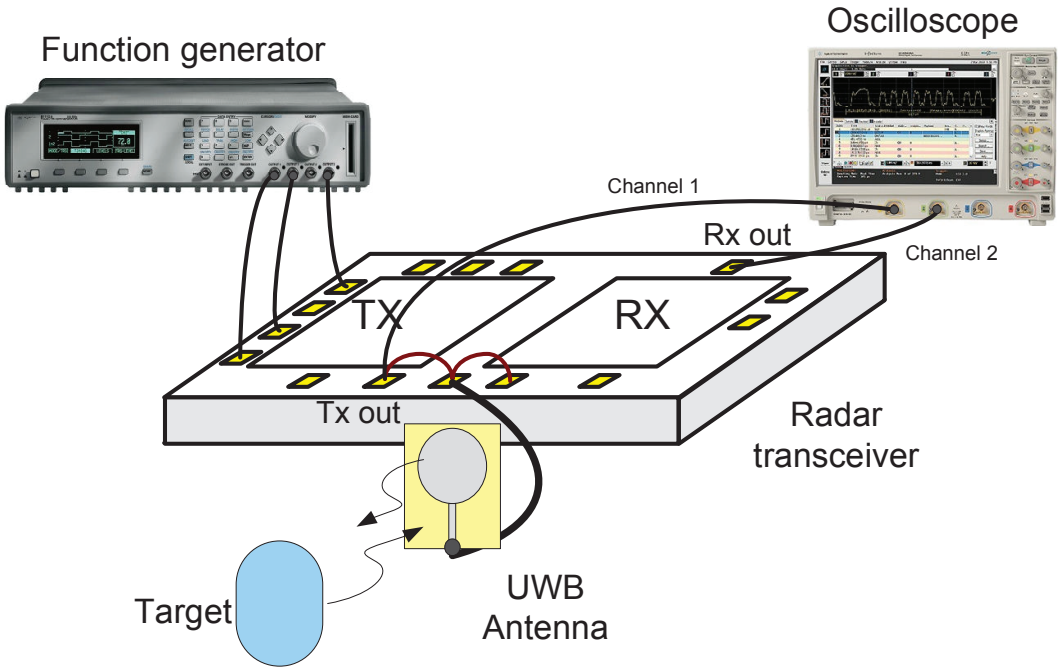

Figure 6.2: Experimental setup for the UWB modulated-pulse radar

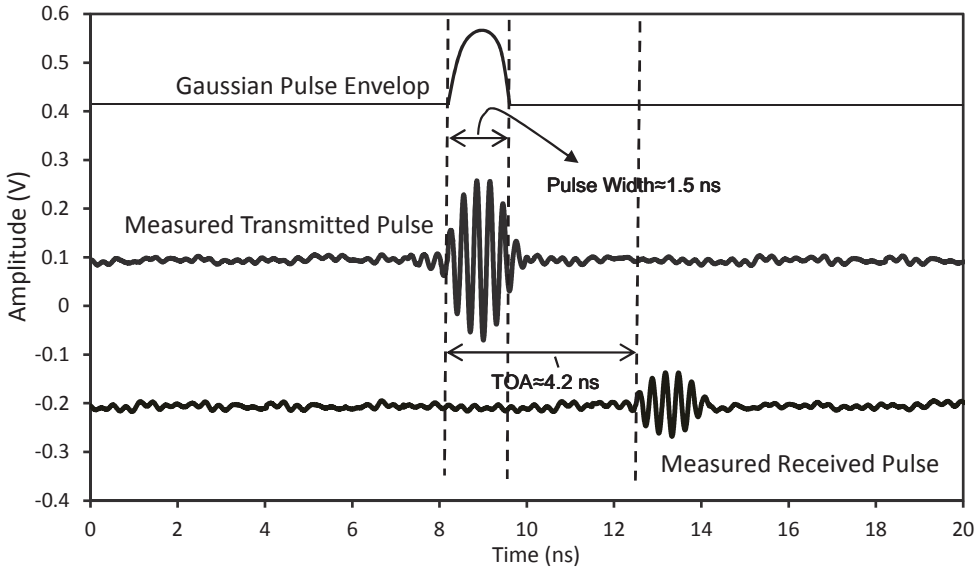

Figure 6.3: Measure transmitted pulse and received pulse

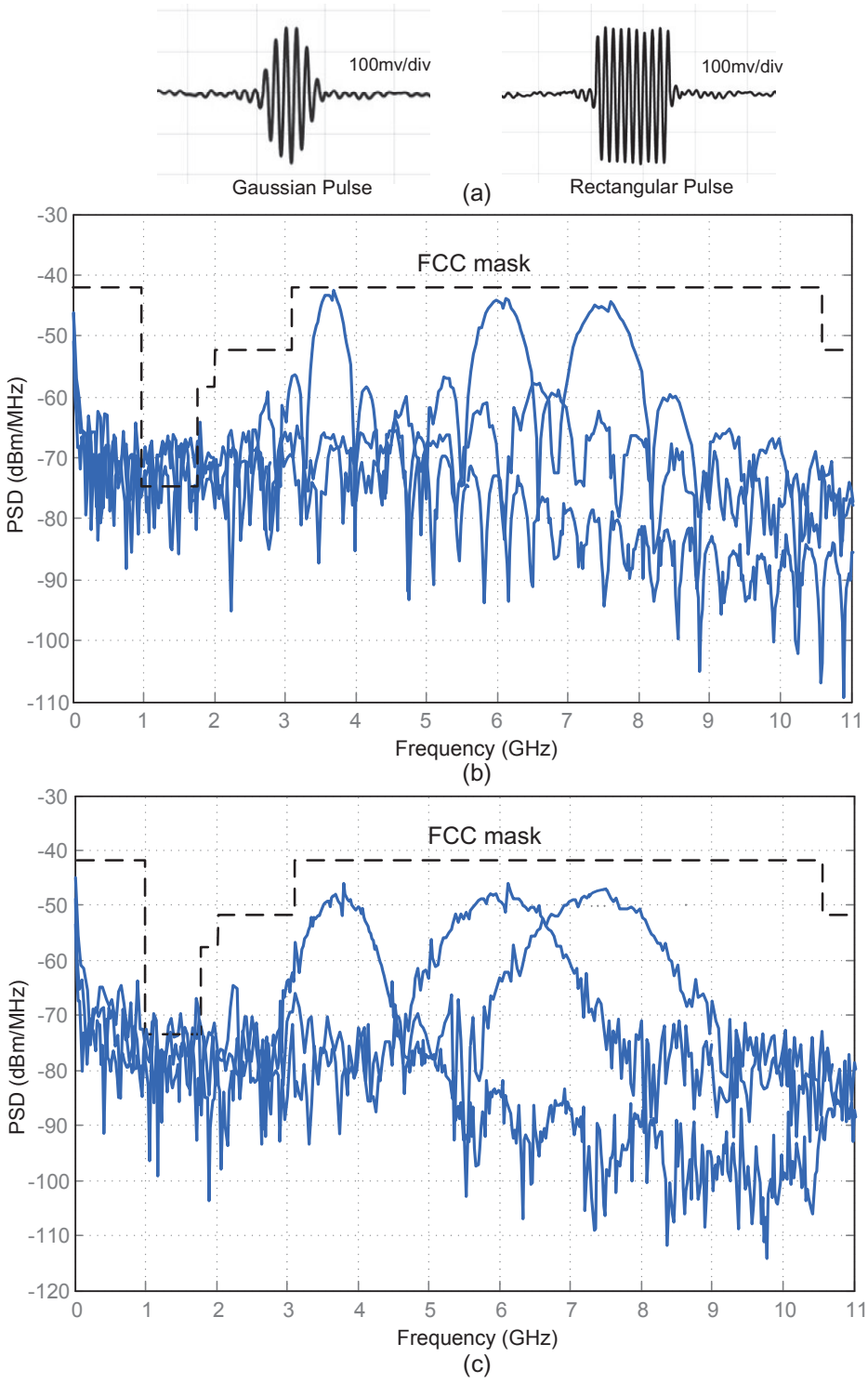

Figure 6.4: Spectrum of UWB radar signal centered at different frequencies

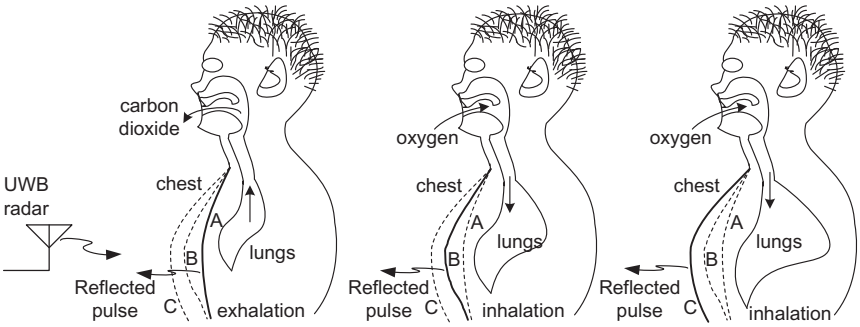

(a) The breathing and radar detecting mechanics

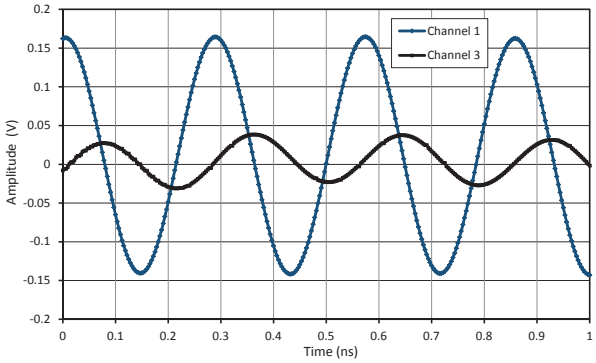

(b) Measured UWB radar waveform at position A

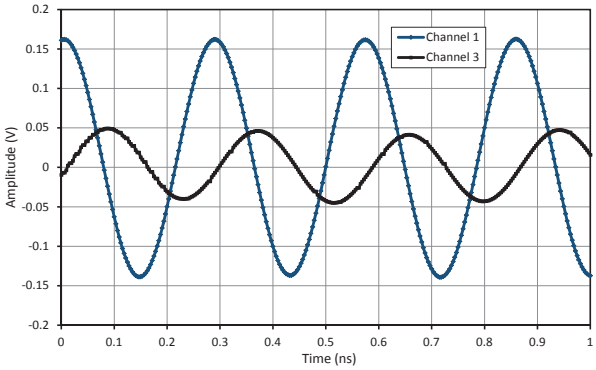

(c) Measured UWB radar waveform at position B

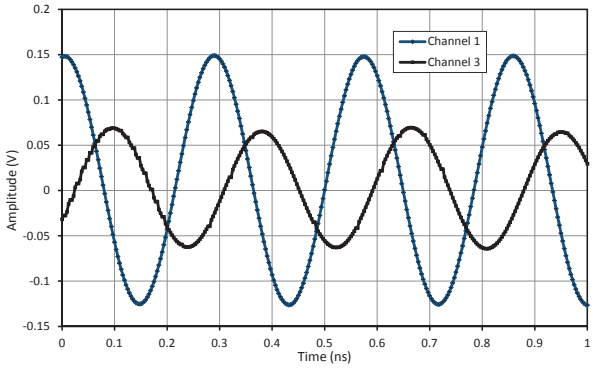

(d) Measured UWB radar waveform at position C

Figure 6.5: Measurement of chest movement and breathing

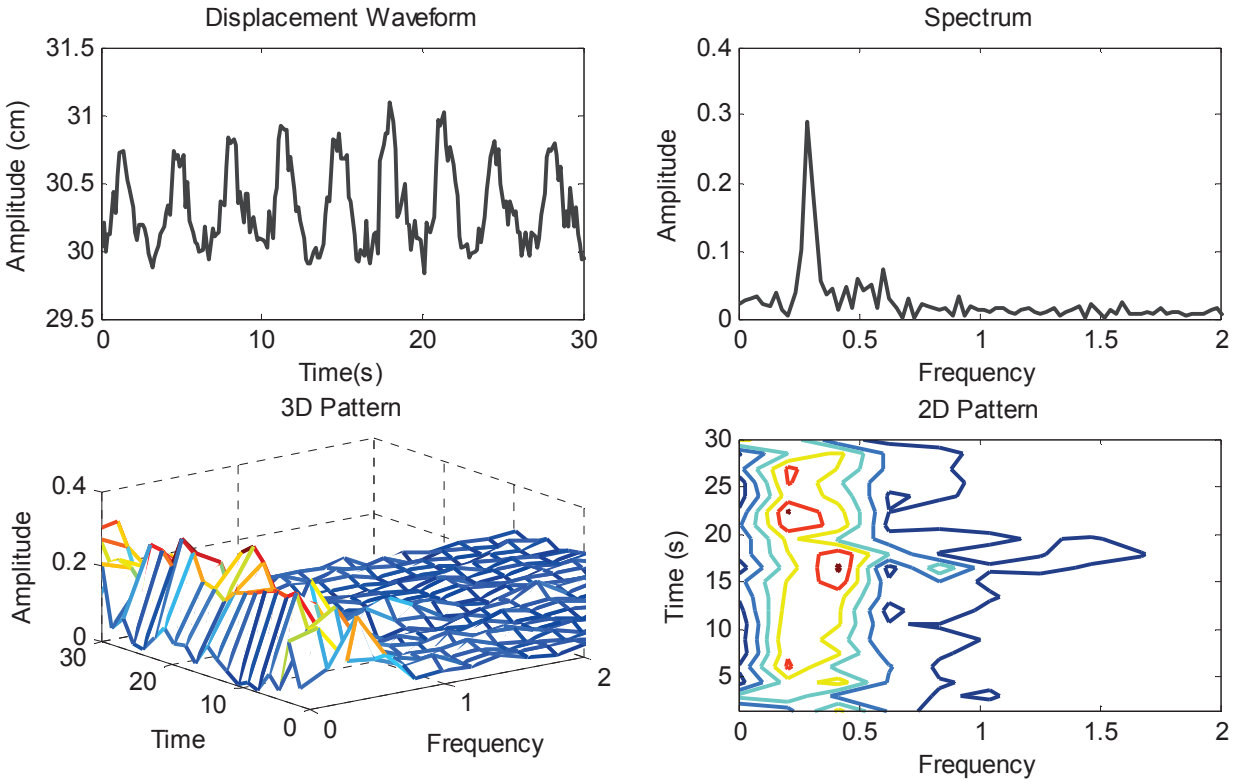

Figure 6.6: Measured radar pulse displacement breathing waveform and its spectrum in frequency domain

6.2 Bio-Radar Performance Analysis

The measured pulse amplitude of the radar transmitter output is about 170 mV on the antenna load. This indicates about -3.47 dBm of instant power at center frequency of 3.7 GHz with a bandwidth of 3 GHz. The FCC's spectral mask limits the power for indoor to the value of -41.3 dBm/MHz. For the output pulse having a bandwidth of 3 GHz, the maximum effective isotropic radiated power is set by

$$\begin{aligned} P_{\max} &= -41.3dBm/MHz + Bandwidth_{dBMHz} \\ &= -41.3dBM/MHz + 34.77dBMHz \\ &= -6.53dBm \end{aligned} \tag{6.1}$$

With the FCC wavier of the Part 15 rules (ET Docket No. 04-352 explicitly removes the requirement to reduce power for gated systems that burst intermittently), -3.47 dBm output power is allowed since this power is only calculated based on the pulsing time. The averaged power emission during the total cycle period still meets the spectral regulation, as shown in Figure 6.4. Within a few meters range, the UWB propagation model can be represented by the Friis equation [114]. A similar analysis method used in [114] was applied here to calculate the detection range. For an UWB radar with a backscatter area σ on a target, exists the relationship [34]

$$P_{rx} = \frac{P_{tx} \cdot G_{ant} \cdot \sigma}{4\pi R^2} \tag{6.2}$$

Here an assumption is made that the human chest is spherical and it behaves as an isotropic radiator sending back a pulse energy with the same polarization as the transmitted signal. The estimated diameter of the chest sphere is 40 cm. The target backscatter area σ is computed based on the area of the target seen from the transmitter and the target reflectivity Γ_{target} at the vertical polarization of the transmitter. The relationship can be expressed as follow:

$$\sigma = 4\pi R^2 \frac{E_r^2}{E_{in}^2} \tag{6.3}$$

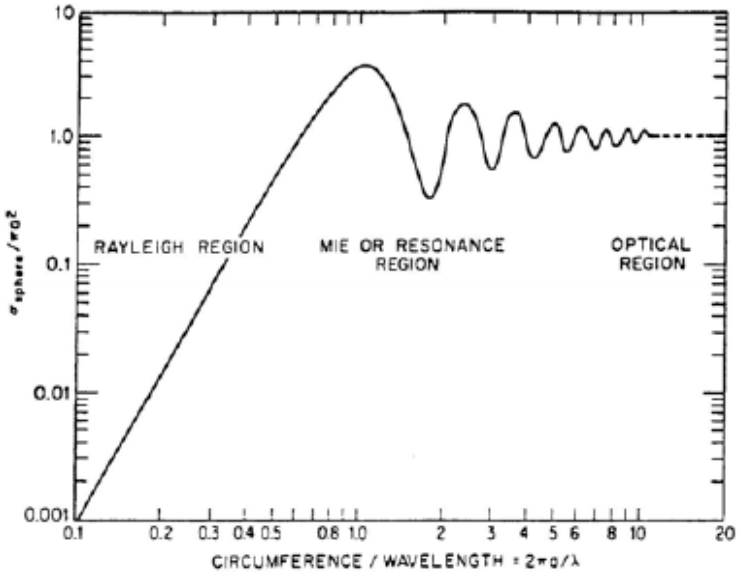

Figure 6.7: Backscatter area versus frequency plot (a chart from [34, 118, 119])

$$\sigma = |Area \cdot \Gamma_{t\arg et}| \tag{6.4}$$

where the Γ_{target} can be defined as the ratio of the power reflected by the target and the power transmitted to the target. The scatter area of the subject's chest is similar to the projection area of a sphere surface with a diameter of 40 cm. Based on a study of the relation between sphere backscatter area and frequency [34, 118, 119], shown in Figure 6.7 [34, 118, 119], the backscatter area can be indexed and calculated from the chart as 0.1256 m^2, where the wavelength λ is computed using the center frequency of the pulse, 3.7 GHz.

The theoretical calculation of the receiver sensitivity is based on the expression

$$Rx_{Sensitivity} = NoiseFloor + NF_{receiver} + SNR_{\min} \tag{6.5}$$

where the noise floor is calculated as:

$$\begin{aligned} NoiseFloor &= kTB \\ &= (1.38 \times 10^{-23}) \cdot 300 \cdot (7.5 \times 10^{9}) \\ &= -105.079 dBm \end{aligned} \tag{6.6}$$

k is the Boltzmann constant, T is the temperature in Kelvin, and B is the signal bandwidth of

interest (here the entire UWB bandwidth is considered). The measured NF of the receiver is 4.8 dB. For a 3-bit ADC with a 19.82 dB SNR (6.02·N+1.76 dB, where N is the bit number), the receiver sensitivity is estimated as

$$Rx_{Sensitivity} = -105.079dBm + 4.8dB + 19.82dB = -80.459dBm \tag{6.7}$$

The reflection coefficient Γ_{target} is described as $(Z_L - Z_s)/(Z_L + Z_s)$ and Z_L is the propagation impedance of the inner layer and Z_s is the propagation impedance of the outer layer. Z can be expressed as $Z = \sqrt{\mu_0/\varepsilon_r\varepsilon_0}$. Based on [6], a coarse estimation concludes the muscle or similar tissue impedance is 60 Ω measured around 3.7GHz and the impedance of free space is 376.7 Ω. Therefore, the calculation shows that the reflection coefficient Γ_{b-m} from free space to skin is (376.7-60)/(376.7+60)=72.5%. This is the dielectric boundary where the most reflection occurs. The total reflection coefficient Γ_{target} will be roughly 72.5%. Based on this information, the final backscatter area is computed as σ_{target}=0.09106 m^2.

The minimum power that can be detected by the UWB receiver is

$$P_{rx} = P_{tx} \cdot G_{ant}^2 \cdot (\frac{\sigma_{t\arg et}}{4\pi R^2}) \cdot (\frac{\lambda^2}{4\pi} \cdot \frac{1}{4\pi R^2}) \cdot FSPL \tag{6.8}$$

The transmitter and receiver patch antenna gains are 10 dBi here to approach a conservative scenario. The signal propagation loss in free space FSPL is estimated based on several iterations.

$$FSPL = (\frac{4\pi d}{\lambda})^2 \tag{6.9}$$

where d is the distance from the antenna to the target. The maximum detectable range R is therefore can be estimated using Equation 2.9 as:

$$R_{\max} = \left[\frac{P_{tx}G_{ant}^2 \cdot FSPL \cdot \lambda^2\sigma_{t\arg et}}{64\pi^3 \cdot P_{rx\_\min}}\right]^{\frac{1}{4}} \tag{6.10}$$

where the receiver power $P_{rx\_\min}$ is the receiver sensitivity of -80.459 dBm. Given all the values for the variables, the estimated maximum sensing range is estimated to be 55 cm. This is a rough estimation because the free space propagation loss calculation is based on

a far field model. For a more accurate calculation, a near field approach could be a better choice.

6.3 Performance Comparisons

Table 6.1: Performance summary of the short-range UWB radar transceiver chip

Designs Parameter	Performance Index
Technology	130 nm CMOS
Supply Voltage	1.2 V
Modulation scheme	OOK
Pulse center frequency	3 - 10 GHz
Pulse width	1 - 5 ns
10 dB pulse BW	1.5 GHz @ 2ns
Minimum detection range	15 cm
Maximum detection range	50 cm
Noise figure	4.8 dB
Receiver sensitivity	-80.459 dBm with 3-bit ADC
Receiver front-end gain	16 dB
Chip area	1 mm× 2 mm
Pulse energy	0.58 pJ @ 2 ns
Total power consumption	20 mW @ 10 MHz

Table 6.1 summarizes the performance of the UWB radar transceiver front-end. Table 6.2 compares the performance to previously published UWB transceivers. The transmitter pulse energy is not compared in this table because the pulse energy is mainly pulse-width dependent.

Both the works reported in [96] and [97] use Gaussian shape impulse generators to generate short impulses to detect respiration rate. Their frequency spectrum are located in the lower UWB band. The centered frequency is hardly tunable. The bandwidth is controlled by changing the pulse width. The transmitter design reported in [98] employs a triangular pulse modulated voltage-controlled oscillator to generator pulse modulated UWB signals. But the

Table 6.2: Summary of UWB overall transceiver front-end performance and comparison with previously published UWB radar IC

Designs	Technology	Technique	Pulse Width [ns]	Freq. Band [GHz]	Supply Voltage [V]	Pulse Energy [pJ/pulse]	Transceiver Power [mW]	Area $[mm^2]$
This Work	130 nm CMOS	Pulsed DCO	1-5	3.1-10	1.2	0.58 @2ns	20 @10MHz	1×2
[96]	90 nm CMOS	Impulse	0.35	2.8-5.4	1.2	N/A	73.2	2
[97]	130 nm CMOS	Impulse	≈1	2-5	1.9	N/A	695	3.6×3.3
[98]	90 nm CMOS	Pulsed VCO	2	3-5	1	N/A	N/A	1.9
[116]	130 nm SiGe BiCMOS	Pulsed VCO	0.5-1.2	BW=2.5 center @24	2.5	N/A	115	1.3×1.2

tuning range is only limited to 3-5 GHz lower UWB band. The design in [116] is another radar transmitter based on a pulsed VCO technique using 130 nm SiGe BiCMOS technology. The center pulse frequency is at 24 GHz with a bandwidth of 2.5 GHz.

6.4 Summary

In this chapter, the measurement results of the UWB radar transceiver IC are presented. This UWB radar transceiver integrates an UWB diplexer with a full UWB band carrier-based transmitter and receiver front-end. The output signal is compliant with the FCC spectrum mask. The experiment demonstrates that a human breathing rate up to 50 cm away can be effectively detected. The UWB radar performance is also compared to the recently published similar UWB radars. To the best of our knowledge, this proposed radar transceiver is the first to use the entire 3-10 GHz band with an ultra-wide frequency tuning capacity. It is one of the first designs in the literature that demonstrates the respiration rate detection using a DCO-type UWB transceiver integrated with an on-chip diplexer. This frequency diversity capability, along with low-cost and high integration of the proposed UWB radar transceiver, makes it a very competitive and cost effective SoC solution for a low-power biomedical radar sensing applications.

Part IV

Epilogue

Chapter 7

Conclusions

7.1 Thesis Summary

In this thesis work, we have investigated and analyzed the possibility of a new generation human-respiration monitoring sensor using UWB radar technology opened after the release of the unlicensed UWB spectrum by the FCC, and we have researched and developed a new prototype of UWB radar sensor for system-on-chip solutions using current standard CMOS technology.

The thesis starts with first two chapters briefly introducing the current status and future trend of the UWB sensing technology, research motivation, and an overview of UWB radar sensing concept, UWB radar systems, and design issues. The thesis proceeded to discuss the research in two sections: impulse UWB radar and carrier-based UWB radar.

The first section is a low-power Gaussian impulse UWB transceiver architecture presented in Chapter 3. An UWB Gaussian pulse transmitter and energy-detection receiver were implemented and fabricated using 90 nm ST CMOS technology. Since the energy of low order Gaussian pulse is mostly condensed in the UWB lower frequency band, in order to transmit the pulse in an efficient way and reduce the frequency leakage at 1-2 GHz band, a higher order Gaussian derivative pulse is desired as the baseband signal. This motivates the advancement of the design into UWB high-order pulse transmitter. Both the Gaussian impulse UWB transmitter and Gaussian higher-order impulse UWB transmitter take the low-power, high-speed advantage of digital circuit to generate different waveforms. The measurement results are analyzed and discussed.

The second section is a low-power carrier-based UWB radar transceiver architecture that exploits the full benefit of UWB bandwidth in radar sensing applications, presented in Chap-

ter 4 and 5. This proposed carrier-based UWB radar transmitter achieves a full UWB band frequency tuning range. The transmitter was fabricated using 130 nm IBM CMOS technology. The measurement results are analyzed and discussed. The proposed fully-integrated UWB diplexer and receiver front-end achieves a 16 dB gain and 3-10 GHz bandwidth, with a 4.8 dB minimum noise figure. The diplexer contributes a 1 dB insertion loss and -30 dB isolation. The receiver front-end was implemented and fabricated using 130 nm IBM C-MOS technology. The measurement results are analyzed and discussed as well. The radar experimental results are demonstrated and discussed in Chapter 6.

7.2 Research Conclusions

This research demonstrates that the UWB technology implemented in the standard CMOS process can be a good alternative to conventional narrow-band technology for bio-radar sensing purpose, in terms of power, cost, and selectivity.

The Gaussian pulse IR-UWB transmitter generates Gaussian pulses with variable pulse width and amplitude at low power and ultra low area cost. However, in order to resolve the limitation of this type of Gaussian pulse transmitter for the need of a high pass filter to eliminate energy contents at the low frequency band and to fit the spectrum requirement, an adaptable all-digital impulse radar transceiver to generate poly-cycle gaussian pulses is proved to be a better evolvement.

In order to improve spectrum controllability, tunability, and spectrum efficiency, an UWB radar transceiver front-end using carrier-based UWB and DCO topology for bio-medical radar sensing is developed, and the performance results prove that the proposed design is a good alternative approach to sensing applications.

The fully integrated mono-static UWB radar transceiver front-end in standard 130 nm CMOS shows the human breathing rate up to 50 cm can be effectively detected. To our best knowledge, this proposed radar transceiver is the first to utilize the entire 3-10 GHz band with ultra-wide frequency tuning capacity. It is one of the first designs in the literature that demonstrates the respiration rate detection using a DCO-type UWB transceiver integrated with on-chip diplexer. This frequency diversity capability, along with low-cost and high integration of the proposed UWB radar transceiver, makes it a very competitive SoC solution

for low-power biomedical radar sensing applications.

The designed radar transceiver outperforms its predecessors that have been reported in literature with respect to die area, power, bandwidth, and chip integrity. The performance improvement and transceiver architecture introduce a new possibility for radar sensor implementation, and move a step forward to the possible economical solution for the future bio-sensor network implementation.

7.3 Future Research Work

This research of UWB radar technology has an impact in major area such as health care and sensor communication. The research paves a path to either replace or integrate wireless technology with current bio-medical system.

Meanwhile, this thesis work provides a starting point for researchers to further study UWB radar sensing. Several interesting research topics in this area are briefly discussed in the remaining sections.

7.3.1 UWB Radar Transceiver Improvement

There are several performances that can be improved in the future design of the radar transceiver:

- The detection range could be improved by increasing the transmitting power. This could be achieved with a more efficient power amplifier that transmits high instaneous power at a low PRF. According to FCC waiver of the Part 15 rules, the average transmitting power over low RPF will still meet FCC spectrum regulation.

- To further extend transceiver integratability, and to further reduce connection loss between antenna and diplexer, an on-chip UWB antenna can be implemented onto the radar transceiver die in the future work. This will enormously reduce the size and cost of the radar sensor and make it more economically feasible to construct a bio-sensor network. The design can be implemented using SOI process to achieve better signal isolation between each block.

- Die characterization is no longer limited to itself. The die needs to be packaged and the packaging greatly affects the performance. Accurate prediction of the effect of packaging at high frequency is increasingly important as the die size continuously shrinks and operates at higher frequencies. Package loss should be modelled and simulated in 3D view for better signal integrity (SI) performance.

- An all-digital transmitter can be synthesized and implemented on an FPGA for re-configurability. Technology migration to the extreme-short sub-micron process is the future research goal to achieve an extremely low-power sensing network and longer operation time.

- The simulation has already demonstrated a data transmission rate of 500 Mb/s using the proposed transceiver; the transceiver implementation needs to be refined to achieve this sensor communication rate for testing. Future design will integrate both the communication function and radar sensing function in the same UWB transceiver chip.

- Currently the transceiver adopts a non-coherent detection scheme. The transceiver can be designed to work with coherent signal processing to extend the sensing range and increase SNR, at the cost of increased complexity and reduced radar PRF. The digital baseband will be included on the transceiver chip in the future.

7.3.2 UWB Human Body Propagation Model

An accurate human body propagation model will offer more insightful information about the received signal. A more sophisticated analysis can be built upon this model [6].

The propagation model and UWB sensing method can be applied to detect and diagnose tumours inside a human body and to build up suitable models for high-frequency wave scattering in living tissue inside the human body. Physiological characteristics can be investigated by UWB signals [6, 120, 121]. Many biological changes in humans are known to be associated with a change of water content [6, 120, 121]. Hence UWB sensing potentially offers a broad spectrum of application in clinical diagnosis [120].

To be more specific, studies to characterise the permittivity of different tissues in the

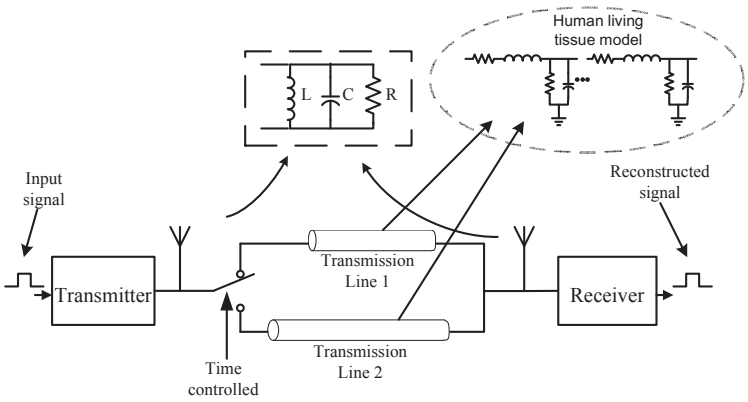

Figure 7.1: UWB propagation channel modeling

frequency range of 3 GHz to 10 GHz will construct the fundamental structure for a human body propagation model used for radar sensing. When measuring the dielectric properties of tumour, dielectric constants are determined by the mixture of cancerous tissue, the skin covering the tumour, and the blood circulation [122, 123]. In contrast, healthy tissue dielectric constants are formed by the skin and normal connective and fatty tissue [122, 123]. The different in dielectric constants will be reflected by the receiving waves and reflection signatures [120, 121]. Different signal processing techniques can be applied to form a spatial image of scattered reflection energy, and extract information from the scattering signatures. Different tissues structure can be identified. This can be applied to detect objects such as breast tumors. [123]

The potential modelling techniques that could be applied include single frequency model, time domain model, and finite-difference time-domain (FDTD) method. Right now, we only know that frequency scattering of the UWB signal will contain information for different target dielectrics. But we have not yet had any quantized analysis to model this difference. In the future work, we will do more work to try to answer these several questions: Why does frequency exactly matter? Which frequency band is more favorable for a specific target dielectric? We believe it is an interesting research topic to carry on.

7.3.3 UWB Bio-radar Sensor Network Implementation

As mentioned in Chapter 2, the final goal of this research is to develop a solution for expendable, low-power, economically feasible, and widely deployable bio-radar sensor network,

which can allow both radar sensing and communications using the same UWB sensor chip. In principle, the impulse UWB transceiver architecture proposed in Chapter 3 is feasible to function in both sensing mode to detect a target and communication mode to send the measurements to a sink node in the sensor network. In addition, an UWB radar transceiver for a radar sensing network and implantable device remains an very profound area of research. The implementation of an indestructible self-healing transceiver circuit and bio-sensor network is also a research topic of interest in next generation CMOS transceiver design.

The UWB transceiver signal analysis is based on the waveform in time domain. In the sensor network application, the radar may receive signals from several targets or a single target with different scatter areas and scatter signatures. It is required to develop an algorithm to detect human and non-human objects to perform real-time positioning and vital signs monitoring in multi-path, multi-target intensive environments. Further extension of the baseband processing may reconstruct the image of the targets.

A more sophisticated model based on the Markov process is being developed to represent the UWB bio-sensor network behaviour. More realistic situations such as lossy channel interference, sensor regeneration, and sensor response delay caused by sensor idling will be taken into account. A bio-sensor network with a sensor self learning algorithm and better power saving techniques will be designed and implemented.

Science is the world without end, it is an eternal mystery.

Albert Einstein

References

[1] Federal Communications Commission, "FCC notice of proposed rule making, revision of part 15 of the commission's rules regarding ultrawideband transmission system," FCC, Washington DC, ET-docket 98-153, Feb., 2002

[2] FCC Notice of Proposed Rule Making, "Revision of Part 15 of the Commissions Rules Regarding Ultra-Wideband Systems." ET-Docket No. 98-153, Feb., 2002.

[3] FCC First Report and Order, "Revision of Part 15 of the Commissions Rules Regarding Ultra-Wideband Systems." ET-Docket No. 98-153, Apr., 2002.

[4] I. Oppermann, M. Hmlinen and J. Iinatti, *UWB : Theory and Applications*. John Wiley and Sons, September 2004.

[5] Faranak Nekoogar, *Ultra-Wideband Communications: Fundamentals and applications*. Prentice Hall Pearson Education, Inc., 2005.

[6] E. M. Staderini, "UWB radar in medicine," *Aerospace and Electronic System Magazine, IEEE*, Vol. 17, Issue 1, pp. 13-18, January 2002.

[7] McEwan: "Body monitoring and imaging apparatus and method". United States Patent 5,766,208 Jun. 16, 1998.

[8] T. McEwan, S. Azevedo, "Micropower Impulse Radar," *Science and Technology Review*, January 1996.

[9] G. B. Carlos, "Bio-medical Sensing using Ultra Wideband Communications and Radar Technology: a feasibility study," 1st International Conference on Pervasive Computing Technologies for Healthcare, 2006.

[10] Jrgen Sachs, *Handbook of Ultra-Wideband Short-Range Sensing*, Wiley-VCH, Dec., 2012.

[11] S. Gabriel, R. W. Lau, and C. Gabriel, "The Dielectric Properties of Biological Tissues: III. Parametric Models for the Dielectric Spectrum of Tissues," *Phys. Med. Biol.,* Vol. 41, pp. 2271-2293, 1996.

[12] I. Y. Immoreev, S. Samkov, and T. H. Tao, "Short Distance Ultra Wideband Radars," *Aerospace and Electronic Systems Magazine, IEEE*, Vol. 20, No. 6, pp. 9- 14, June 2005.

[13] Immoreev I. Y. "Practical Application of Ultra-Wideband Radars," *IEEE Ultrawideband and Ultrashort Impulse Signals*, pp. 44-49, Septemeber 2006.

[14] P. Bernardi, R. Cicchetti, S. Pisa, E. Pittella, E. Piuzzi, and O. Testa, "Design and Realization of a UWB Radar for Breath Activity Monitoring," *Electromagnetic Compatibility (EMC EUROPE), 2012 International Symposium on*, Rome, Sept., 2012.

[15] C. Y. Lee and C. Toumazou, "Ultra-low Power UWB for Real Time Biomedical Wireless Sensing," *IEEE International Symposium on Circuits and Systems*, pp. 57- 60, May 2005.

[16] Wireless2000, Patient Assessment Monitor (PAM 3000), Wireless2000 RF and UWB Tech., Burnaby, BC, Canada, 2007, http://www.wireless2000.com/hrrm.htm.

[17] Igor Immoreev, "Ten Questions on UWB," *IEEE AES Systems Magazine*, pp. 8-10, November, 2003.

[18] P. K. Saha, N. Saski and T. Kikkawa, "Impulse-based UWB transmitter in 0.18μm CMOS for Wireless interconnect in future ULSI," *Ext. Abst. of the Fourth Hiroshima International Workshop on Nanoelectronics for Tera-bit Information Processing*, Hiroshima University, Japan, pp. 76-77, September 2005.

[19] H. Lee et al., "A 15mW 69dB 2G sample/s CMOS analog front-end for low-band UWB applications," *IEEE Proc. Int. Circuits Syst. Symp.,* pp. 368-371, 2005.

[20] P. Mercier et al., "Ultra-low-power UWB for sensor network applications," *IEEE Proc. Int. Circuits Syst. Symp.,* pp. 2562-2565, 2008.

[21] Junwoo Lee, Young-Jin Park, Myunghoi Kim, Changwook Yoon, Joungho Kim, and Kwan-Ho Kim, "System-On-Package Ultra-Wideband Transmitter Using CMOS Im-

pulse Generator," *IEEE Transcations on Microwave Theory and Techniques*, Vol. 54, No. 4, pp. 1667 - 1674, April 2006.

[22] Yanjie Wang, Ali M. Niknejad, Vincent Gaudet, and Kris Iniewski, "A CMOS IR-UWB Transceiver Design for Contact-Less Chip Testing Applications," *IEEE Transcations on Circuits and Systems-II:Express Briefs*, Vol. 55, No. 4, pp. 334-338, April 2008.

[23] Jin He, Y. P. Zhang, "A CMOS Ultra-Wideband Impulse Radio Transceiver for Inter-chip Wireless Communications," *IEEE International Conference on Ultra-Wideband, ICUWB*, September 2007.

[24] Dolmans G., Rousseaux O., Li Huang, Ting Fu, Gyselinkx B., D'Amico S.,Baschirotto, A., Ryckaert J., Van Poucke B., "UWB Radio Transceivers For Ultra Low Power and Low Data Rate Communications," *IEEE International Conference on Ultra-Wideband, ICUWB*, pp. 152-157, September, 2007.

[25] Mitchell Lazarus, "The FCC Waives The Ultra-Wideband Rules - Again," *The Law of Communications*, Published by Fletcher, Heald & Hildreth, 2011.

[26] Federal Communications Commission, "Waiver granted to waive Parts 15.503(d) and 15.521(d) of the FCC Rules," FCC, Washington DC, DA 12- 41, Jan., 2012.

[27] J. Foerster, "Channel Modeling Sub-Committee Report (Final)," IEEE P802.15 Working Group for Wireless Personal Area Networks (WPANs), February 2003.

[28] A. F. Molisch, "IEEE 802.15.4a Channel Model Final Report," IEEE P802.15 Working Group for Wireless Personal Area Networks (WPANs), November 2004.

[29] "IEEE 802.15 WPAN Low Rate Alternative PHY Task Group 4a (TG4a)," IEEE Standards Association. March 30, 2007.

[30] Fred S. Lee, "Energy Efficient Ultra-Wideband Radio Transceiver Architectures and Receiver Circuits," PhD dissertation, MIT, 2007.

[31] David Barras, "A Low-power Impulse Radio Ultra-wideband CMOS Radio-frequency Transceiver," PhD dissertation, ETH ZURICH, 2010.

[32] D.J. Daniels, *Surface-Penetrating Radar*, The Institution of Electrical Engineers, 1996.

[33] David J. Daniels, *Ground Penetrating Radar, 2nd Edition*, The Institution of Electrical Engineers, 2004.

[34] Eugene F. Knott, John F. Shaeffer, Michael T. Tuley, *Radar Cross Section, Edition 2*, The Institution of Electrical Engineers, 2003.

[35] Jun Jason Zhang and Antonia Papandreou-Suppappola,"MIMO Radar with Frequency Diversity," *International WD and D Conference*, pp. 208-212, 2009.

[36] L. Stoica, A. Rabbachin, H. O. Repo, T. S. Tiuraniemi, and I. Oppermann, "An ultra-wideband system architecture for tage based wireless sensor networks," *IEEE Transactions on Vehicular Technology,* Vol. 54, No. 5, pp. 1632-1645, September 2005.

[37] Lingli Xia, Ke Shao, Hu Chen, Yumei Huang, Zhiliang Hong, and Patrick Y. Chiang, "0.15nJ/b 3-5GHz IR-UWB System With Spectrum Tunable Transmitter and Merged-Correlator Noncoherent Receiver," *IEEE Transactions on Microwave Theory and Techniques,* Vol. 59, No. 4, pp. 1147-1156, April, 2011.

[38] S. R. Duenas, X. Duo, S. Yamac, M. Ismail, and L. R. Zheng, "CMOS UWB IR non-coherent receiver for RF-ID applications," *IEEE North-East Workshop Circuits Syst.*, pp. 213-216, 2006.

[39] M. M. Verhelst and W. W. Dehaene, "Analysis of the QAC IR-UWB receiver for low energy, low data-rate communication," *IEEE Trans. Circuits Syst. I, Reg. Papers*, Vol. 55, No. 8, pp. 2423-2432, September 2008.

[40] Julien Ryckaert, Mustafa Badaroglu, Vincent De Heyn, Geert Van der Plas, Pierluigi Nuzzo, Andrea Baschirotto, Stefano DAmico, Claude Desset, Hans Suys, Michael Libois, Bart Van Poucke, Piet Wambacq, Bert Gyselinckx, "A 16 mA UWB 3-to-5 GHz 20 Mpulses/s Quadrature Analog Correlation Receiver in 0.18 μm CMOS," *IEEE International Solid-State Circuits Conference*, pp. 368-377, 2006.

[41] Xubo Wang, Anh Dinh, and Daniel Teng, "Reliability Modeling for Wireless Ultra Wideband Biomedical Radar Sensing Network," *Bioinformatics and Biomedical Technology (ICBBT), 2010 International Conference on*, pp. 69-73, April 2010.

[42] Anand Panangadan, Syed Muhammad Ali, and Ashit Talukder, "Markov Decision Processes for Control of a Sensor Network-based Health Monitoring," *In Proc. of the*

Seventeenth Conf. on Innovative Applications of Artificial Intelligence(IAAI), pp. 1529-1534, 2005.

[43] D. Bein, V. Jolly, B. Kumar and S. Latifi, "Reliability Modeling in Wireless Sensor Networks," *International Journal of Information Technology*, Vol. 11, No. 2, 2003.

[44] C. F. Chiasserini and M. Garetto, "Modeling the Performance of Wireless Sensor Networks," *IEEE Conference on Computer Communications (INFOCOM)*, March 7-11, 2004.

[45] Xinyu Chen and Michael R. Lyu, "Reliability Analysis for Various Communication Schemes in Wireless CORBA," *IEEE Transaction on Reliability*, Vol. 54, No. 2, June 2005.

[46] Vladimir V. Shakhov and Hyunseung Choo, "Reliability of Wireless Sensor Network with Sleeping Nodes," *International Conference on Conceptual Structures (ICCS)*, pp. 530-534, 2007.

[47] Akhilesh Shrestha, Liudong Xing, and Hong Liu, "Infrastructure Communication Reliability of Wireless Sensor Networks," *Proceedings of the 2nd IEEE International Symposium on Dependable, Autonomic and Secure Computing, DASC06*, 2006.

[48] Richard chi-Hsi Li, *Key Issues in RF/RFIC Circuit Design*, Higher Education Press, 2006.

[49] Alan Hastings, *The Art of Analog Layout, 2nd Edition,* Prentice Hall Pearson Education, Inc., 2006.

[50] Anfu Zhu, Fu Sheng, and Anxue Zhang, "An Implementation of Step Recovery Diode-Based UWB Pulse Generator," *IEEE International Conference on Ultra-Wideband*, Sept., 2010.

[51] H. G. Jungmeister and D. Schmidt, "High-speed pulse circuits obtain-ed by computer-aided nonlinear analysis of step-recovery diodes," *IEEE Journal of Solid-state Circuits*, Vol. SC-5, No. 4, August 1970.

[52] J. Han, M. Miao and C. Nguyen, "Recent development of SRD- and FET-based subnanosecond pulse generators for ultra-wideband Communications," *IEEE Topical Conference on Wireless Communication Technology*, 2003.

[53] K. Li, D. Kurita, and T. Matsui, "A novel UWB bandpass filter and its application on UWB pulse generation," *IEEE International Conference Ultra-Wideband*, pp.446-451, 2005.

[54] Y. Zhu, J. R. Marciante, J. D. Zuegel, and H. Wu, "Integrated distributed transversal filters for pulse shaping and interference suppression in UWB impulse radios," *IEEE International Conference Ultra-Wideband*, pp. 563-568, Oct. 2006.

[55] K. Marsden, H. J. Lee, D. Ha, and H. S. Lee, "Low power CMOS re-programmable pulse generator for UWB systems," *IEEE Conf. UWB Systems Technologies*, pp. 443-447, 2003.

[56] D. Baranauskas and D. Zelenin, "A 0.36 W 6b up to 20 GS/s DAC for UWB wave formation," *IEEE Int. Solid-State Circuits Conf. Dig. Tch. Papers,* pp. 580-581, 2006.

[57] P. Schvan et al., "A 22 GS/s 6b DAC with Integrated Digital Ramp Generator," *ISSCC Dig. Tech. Papers,* pp. 122-123, Feb., 2005.

[58] D. D. Wentzloff and A. P. Chandrakasan, "Gaussian Pulse Generators for Subbanded Ultra-Wideband Transmitters," *IEEE Trans. Microw. Theory Tech.*, Vol. 54, No. 4, pp. 1647-1655, Apr. 2006.

[59] J. Ryckaert, C. Desset, A. Fort, M. Badaroglu, V. D. Heyn, P. Wambacq, G. V. der Plas, S. Donnay, B. V. Poucke, and B. Gyselinckx, "Ultra-wideband transmitter for low-power wireless body area networks: Design and evaluation," *IEEE Trans. Circuits Syst. I, Reg. Papers*, Vol. 52, No. 12, pp. 2515-2525, Dec., 2005.

[60] Maria G. D Benedetto and Guerino Giancola, *Understanding Ultra Wide Band Radio Fundamentals*, Pearson Hall, 2005.

[61] Stanley Bo-Ting Wang, *Design of Ultra-Wideband RF Front-End*, PhD dissertation, University of California, Berkeley, 2005.

[62] Qiu, R.C., "A Theory of Time-Reversed Impulse Multiple-Input Multiple-Output (MIMO) for Ultra-Wideband (UWB) Communications", *IEEE 2006 International Conference on Ultra-Wideband*, pp. 587-592, Sept. 2006.

[63] R. C. Qiu, C. Zhou and Q. Liu, "Physics-Based Pulse Distortion for Ultra-Wideband Signals", *IEEE Transactions on Vehicular Technology*, Vol. 54, No. 5, pp. 1546-1555, Sept. 2005.

[64] Chenming Zhou, "Impulsive Radio Propagation and Time Reversed MIMO System for UWB Wireless Communications", PhD Dissertation, Tennessee Technological University, 2008.

[65] X. Wang, A. Dinh, D. Teng, L. Chen, S. B. Ko, "Impulse Based Range-Gated UWB Wireless Transceiver IC in 90nm CMOS for Medical Sensing Applications and Communications,", *IEEE International Conference on Ultra-Wideband (ICUWB)*, pp. 194-199, Vancouver, Canada, Sept., 2009.

[66] T. Terada, S. Yoshizumi, M. Muqsith, Y. Sanada and T. Kuroda, "A CMOS Ultra-wideband impulse radio transceiver for 1-Mb/s data communications and ±2.5-cm range finding," *IEEE Journal of Solid-State Circuits*, Vol. 41, No. 4, pp. 891-898, April 2006.

[67] N. Paulino, J. Goes, A. Steiger-Garcao, "A CMOS Variable Width Short-Pulse Generator Circuit for UWB RADAR Applications," *Circuits and Systems, IEEE International Symposium, ISCAS 2008 IEEE*, May 2008.

[68] Silvia Solda *et al.*, "A 5 Mb/s UWB-IR Transceiver Front-End for Wireless Sensor Networks in 0.13um CMOS," *IEEE J. Solid-Stae Circuits*, Vol. 46, No. 7, pp. 1636-1646, Jul. 2011.

[69] Bernhard Wicht, Thomas Nirschl, and Doris Schmitt-Landsiedel, "Yield and Speed Optimization of a Latch-Type Voltage Sense Amplifier," *IEEE JOURNAL OF SOLID-STATE CIRCUITS,* Vol. 39, No. 7, pp. 1148-1158, July, 2004.

[70] Martin S. Smith, *Introduction to Antennas*, Macmillan Education, London, 1988.

[71] C. N. Paulson, J. T. Chang, C. E. Romero, J. Watson, F. J. Pearce, N. Levin, "Ultra-wideband Radar Methods and Techniques of Medical Sensing and Imaging," *SPIE International Symposium on Optics East*, Boston, MA, US, 2005.

[72] P. K. Saha, N. Saski and T. Kikkawa, "Impulse-based UWB transmitter in 0.18um CMOS for Wireless interconnect in future ULSI," *Ext. Abst. of the Fourth Hiroshi-*

ma International Workshop on Nanoelectronics for Tera-bit Information Processing, Hiroshima University, Japan, pp. 76-77, September 2005.

[73] T. H. Lee, *The Design of CMOS Radio-Frequency Integrated Circuits*, 1st ed., New York: Cambridge Univ. Press, 1998.

[74] Yifan Chen, Erry Gunawan, Kay Soon Low, Cheong Boon Soh, and Lin Lin Thi, "Human Respiration Rate Estimation Using Body-Worn Ultra-Wideband Radar," *Antennas and Propagation International Symposium, 2007 IEEE*, June 2007.

[75] A. E. Tan, M. Y. Chia, and S. Leong, "Sub-nanosecond pulse forming network on SiGe BiCMOS for UWB communicatioins," *IEEE Trans. Micro. Theory Tech.*, Vol.54, No. 3, pp. 1019-1024, Mar. 2006.

[76] L. Smaini, C. Tinella, D. Helal, C. Stoecklin, L. Chabert, C. Devaucelle, R. Cattenoz, N. rinaldi, and D. Belot, "Single-chip CMOS pulse generator for UWB systems," *IEEE J. Solid-State Circuits*, Vol.41, no. 7, pp. 1551-1561, Jul. 2006.

[77] J. Han and C. Nguyen, "A new ultra-wideband, ultra-short monocycle pulse generator with reduced ringing," *IEEE Micro. Wireles. Compon. Lett.*, Vol.12, No.6, pp.206-208, Jun. 2002.

[78] Y. Zheng, Y. Zhang, and Y. Tong, "A novel wireless interconnect technology using impulse radio for interchip communications," *IEEE Trans. Micro. Theory Tech.*, Vol.54, No.4, part II, pp. 1912-1920, April 2006.

[79] Tuan Anh Phan, Jeongseon Lee, Vladimir Krizhanovskii, Quan Le, Seok-Kyun han, and Sang-Gug Lee, "Energy-Efficient Low-Complexity CMOS Pulse Generator for Multiband UWB Impulse Radio," *IEEE Trans. Circuits and System*, Vol.55, No.11, pp.3552-3563, 2008.

[80] N. Paulino, J. Goes, A. Steiger-Garcao, "A CMOS Variable Width Short-Pulse Generator Circuit for UWB RADAR Applications," *Circuits and Systems, IEEE International Symposium, ISCAS 2008 IEEE*, May 2008.

[81] Patrick P. Mercier, Denis C. Daly, and Anantha P. Chandrakasan, "An Energy-Efficient All-Digital UWB Transmitter Employing Dual Capacitively-Coupled PUlsed-Shaping

Drivers," *IEEE Journal of Solid-State Circuits*, Vol. 44, No. 6, pp. 1679-1688, June 2009.

[82] Chul Kim and Saeid Noosahbadi, "Design of a Tunable All-Digital UWB Pulse Generator CMOS Chip for Whreless Endoscope," *IEEE Transcations on Biomedical Circuits and Systems*, Vol. 4, No. 2, pp. 1932-4545, June 2010.

[83] Wang, X., Dinh, A.v. and Teng, D., "Ultra Wide-Band High-Order Pulse Digital Transmitter IC in 90nm CMOS for Biomedical Radar Sensing, *IEEE International Conference on Ultra-Wideband (ICUWB)*, pp. 336-340, Bologna, Italy, Sept., 2011.

[84] Julien Ryckaert, Geert Van der Plas, Vincent De Heyn, Claude Desset, Bart Van Poucke, and Jan Craninckx, "A 0.65-to-1.4 nJ/Burst 3-to-10 GHz UWB All-Digital TX in 90nm CMOS for IEEE 802.15.4a," *IEEE Journal of Solid-State Circuits*, Vol. 42, No. 12, pp. 2860-2869, December 2007.

[85] Rui Xu, Yalin Jin, and Cam Nguyen, "Power-Efficient Switching-Based CMOS UWB Transmitters for UWB Communications and Radar Systems," *IEEE Transaction on Microwave Theory and Techniques*, Vol. 54, No. 8, pp. 3271-3277, August 2006.

[86] Jorge R. Fernandes, Hugo B. Goncalves, Luis B. Oliveira, and Manuel M. Silva, "A Pulse Generator for UWB-IR Based on a Relaxation Oscillator," *IEEE Transactions on Circuits and Systems-II Express Briefs*, Vol. 55, No. 3, pp. 239-243, March 2008.

[87] David Barras, Frank Ellinger, Heinz Jackel, and Walter Hirt, "Low-Power Ultra-Wideband Wavelets Generator With Fast Start-Up Circuit," *IEEE Transactions on Microwave Theory and Techniques*, Vol. 54, No. 5, pp. 2138-2145, May 2006.

[88] Lingli Xia, Changhui Hu and Patrick Chiang. "Chapter 6: Ultra Wideband RF Transceiver Design in CMOS Technology", *Ultra Wideband Communications: Novel Trends - System, Architecture and Implementation*, Dr. Mohammad Matin (Ed.), ISBN: 978-953-307-461-0, InTech, 2011.

[89] Tuan Anh Phan, Jeongseon Lee, Vladimir Krizhanovskii, Quan Le, Seok-Kyun Han, and Sang-Gug Lee, "Energy-Efficient Low-Complexity CMOS Pulse Generator for Multiband UWB Impulse Radio," *IEEE Transactions on Circuits and Systems I*, Vol. 55, No. 11, pp. 3552-3563, 2008.

[90] H. Kim and Y. Joo, "Fifth-derivative Gaussian Pulse Generator for UWB System" *RFIC IEEE Symposium on*, pp. 671-674, 2005.

[91] A. Bevilacqua *et al.*, "Transformer-Based Dual-Mode Voltage Controlled Oscillators," *IEEE Trans. Circuit and System-II*, Vol. 54, No. 4, pp. 293-297, April 2007.

[92] L. H. Lue, H. Hsieh-Hung, and L. Yu-Te, "A Wide Tuning-Range CMOS VCO With a Differential Tunable Active Inductor," *IEEE Trans. Microwave Theory and Techniques*, Vol. 54, No. 9, pp. 3462-3468, Sept. 2006.

[93] D. Hauspie, P. Eun-Chul, and J. Craninckx, "Wideband VCO With Simultaneous Switching of Frequency Band, Active Core, and Varactor Size," *IEEE J. Solid-Stae Circuits*, Vol. 42, No. 7, pp. 1472-1480, Jul. 2007.

[94] Zahra Safarian, and Hossein Hashemi, "Wideband Multi-Mode CMOS VCO Design Using Coupled Inductors," *IEEE Trans. Circuit and Systems-I*, Vol. 56, No. 8, pp. 1830-1843, August 2009.

[95] X. Wang, A. Dinh, D. Teng, L. Chen, S. B. Ko, Y. Shi, V. Dal Bello-Hass, and J. Basran, "Impulse Based Range-Gated UWB Wireless Transceiver IC in 90nm CMOS for Medical Sensing Applications and Communications," *IEEE International Conference on Ultra-Wideband, ICUWB 2009*, September 2009.

[96] Domenico Zito et al., "SoC CMOS UWB Pulse Radar Sensor for Contactless Respiratory Rate Monitoring," *IEEE Transactions on Biomedical Circuits and Systems*, Vol. 5, No. 6, pp. 503-510, Dec. 2011.

[97] Ta-Shun Chu, Jonathan Roderick, SangHyun Chang, et al., "A Short-Range UWB Impulse-Radio CMOS Sensor for Human Feature Detection," *IEEE ISSCC Dig. Tech. Papers*, pp. 294-296, Feb. 2011.

[98] R. Dokania et al., "An Ultralow-Power Dual-Band UWB Impulse Radio," *IEEE Transactions on Circuits and Systems-II: Express Briefs*, Vol. 57, No.7, pp. 541-545, July 2010.

[99] Po-Yu Chang and Shawn S. H. Hsu, "A Compact 0.1-14-GHz Ultra-Wideband Low-Noise Amplifier in 0.13-um CMOS," *IEEE Transactions on Microwave Theory and Techniques*, Vol. 58, No. 10, pp. 2575-2581, October 2010.

[100] M. T. Reiha and J. R. Long, "A 1.2 V Reactive-Feedback 3.1-10.6 GHz Low-Noise Amplifier in 0.13um CMOS," *IEEE J. Solid-State Circuits*, Vol. 42, No. 5, pp. 1023-1033, May 2007.

[101] R. C. Liu, K. L. Deng, and H. Wang, "A 0.6-22-GHz Broadband CMOS Distributed Amplifier," *IEEE Radio Frequency Integrated Circuits symp. Dig. Papers,* pp. 103-106, 2003.

[102] Y. J. Wang and A. Hajimiri, "A compact Low-Noise Weighted Distributed Amplifier in CMOS," *IEEE Int. Solid-State Circuits Conf. Tech. Dig.*, pp. 220-221, 2009.

[103] T. H. Lee, *The Design of CMOS Radio-Frequency Integrated Circuits, 2nd ed.* New York: Cambridge Univ. Press, 2005.

[104] David Murphy, Jacob J. Rael, and Asad A. Abidi, "Phase Noise in LC Oscillators: A Phasor-Based Analysis of a General Result and of Loaded Q," *IEEE TRANSACTIONS ON CIRCUITS AND SYSTEMSI: REGULAR PAPERS*, Vol. 57, No. 6, pp. 1187-1203, June, 2010.

[105] A. Bevilacqua and A. M. Niknejad, "An Ultrawideband CMOS Low-Noise Amplifier for 3.1-10.6 GHz wireless receivers," *IEEE J. Solid-State Circuits*, Vol. 39, No. 12, pp. 2259-2268, Dec. 2004.

[106] Q. Li and Y. P. Zhang, "A 1.5V 2-9.6 GHz Inductorless Low-Noise Amplifier in 0.13um CMOS," *IEEE Transactions on Microwave Theory and Techniques*, Vol. 55, No. 10, pp. 2015-2023, Oct. 2007.

[107] Christopher Bowick, Cheryl Ajluni, and John Blyler, *RF Circuit Design, 2nd Edition*, Newnes, 2007.

[108] Khurram Muhammad and S. M. Rezaul Hasan, "A Full-Band UWB Common-Gate Band-Pass Noise Matched g_m-boosted series peaked CMOS differential LNA," *Analog Integrated Circuit and Signal Processing, Springer*, Vol. 76, pp. 47-60, 2013.

[109] Hasan Rezaul, S. M, "Analysis and Design of a Multi-Stage CMOS Band-Pass Low Noise Pre-Amplifier for Ultra-Wide-Band RF Receiver," *IEEE Transactions on VLSI Systems*, Vol. 18, No. 4, pp. 638-651, 2010.

[110] B. Park, S. Choi, and S. Hong, "A Low Noise Amplifier with Tunable Interference Rejection for 3.1-10.6-GHz UWB Systems," *IEEE Microwave Wireless Component Letters*, Vol. 20, No. 1, pp. 40-42, 2010.

[111] Perumana Bevin G., et al., "Resistive-Feedback CMOS Low-Noise Amplifiers for Multiband Applications," *IEEE Transactions on Microwave Theory and Techniques*. Vol. 56, No. 5, pp. 1218-1225, 2008.

[112] Jianxin Liang, Choo C. Chiau, Xiaodong Chen, and Clive G. Parini, "Study of a Printed Circular Disc Monopole Antenna for UWB Systems," *IEEE Transactions on Antennas and Propagation*, Vol. 53, No. 11, pp. 3500-3504, Nov. 2005.

[113] S. Licul, J. A. N. Noronha,W. A. Davis, D. G. Sweeney, C. R. Anderson, and T. M. Bielawa, "A parametric study of time-domain characteristics of possible UWB antenna architectures," *Vehicular Technology Conference*, Oct. 2003.

[114] Carlos Gustavo Bilich, "Feasibility of Bio-Medical Sensing Using Ultra Wideband Communications and Radar Technology," PhD Dissertation, University of Trento, Italy, 2007.

[115] Okan Zafer Batur et al., "An Ultra Low-Power Dual-Band IR-UWB Transmitter in 130-nm CMOS," *IEEE Transactions on Circuits and Systems-II: Express Briefs*, Vol. 59, No. 11, pp. 701-705, Nov. 2012.

[116] A. Scuderi, E. Ragonese, G. Palmisano, "24-GHz Ultra-Wideband Transmitter for Vehicular short-range radar applications," *IET Circuits, Devices & Systems*, Vol. 3, Issue 6, pp. 313-321, Dec. 2009.

[117] Jianxin Liang et al., "Study of a Printed Circular Disc Monoploe Antenna for UWB systems" *IEEE Transactions on Antennas and Propagation*, Vol. 53, No. 11, pp. 3500-3504, Nov. 2005.

[118] Edde, B., *RADAR: Principles, technology, applications*, Prentice Hall, 1995.

[119] Asoke K. Bhattacharyya, D. L. Sengupta, *Radar Cross Section Analysis and Control*, Artech House, 1991.

[120] M. Lazebnik, D. Popovic, L. McCartney et al., "A large-scale study of the ultrawideband microwave dielectric properties of normal, benign and malignant breast tissues

obtained from cancer surgeries," *Physics in Medicine and Biology*, Vol. 52, No. 20, pp. 6093-6115, Oct 21, 2007.

[121] M. Helbig, M. A. Hein, R. Herrmann et al., "Experimental active antenna measurement setup for UWB breast cancer detection," *IEEE International Conference on Ultra-Wideband, ICUWB 2012*, Syracuse, USA, Sept. 2012.

[122] M. Helbig, I. Hilger, M. Kmec, et al., "Experimental phantom trials for UWB breast cancer detection," *Proc. German Microwave Conf.*, Ilmenau, Germany, pp. 1-4, March 2012.

[123] M. Helbig, C. Geyer, M. Hein et al., "A Breast Surface Estimation Algorithm for UWB Microwave Imaging," *IFMBE Proceedings 4th European Conference of the International Federation for Medical and Biological Engineering*, pp. 760-763, 2009.